UNIVERSITÀ DEGLI STUDI DI PADOVA

FACOLTÀ DI SCIENZE MM. FF. NN.
Dipartimento di Geoscienze
Direttore Prof. Cristina Stefani

TESI DI LAUREA SPECIALISTICA
IN
GEOLOGIA E GEOLOGIA TECNICA

# TECTONIC EVOLUTION OF THE HOLY CROSS MOUNTAINS (POLAND)

**Relatore:** Prof. Massimiliano Zattin
**Correlatori:** Dott. Benedetta Andreucci
Dott. Ada Castelluccio

**Laureando:** Silvia Cattò

ANNO ACCADEMICO 2013/2014

## ABSTRACT

The Holy Cross Mountains, located in the southern part of the central Poland, possesses especially interesting features for geological studies, particularly, the role of the long-lived Holy Cross Fault and the timing of tectonic evolution are still to be evaluated. Throughout the combined use of the thermochronology and structural modelling software, the tectonic evolution of the area is achieved .

In particular, low-temperature thermochronometers have been widely used, as (U-Th)/He analysis and fission tracks analysis, both performed on apatites. The samples collected in situ have been worked to obtain fitting crystals for the analysis. Thermochronological ages have been used to constrain and clarify the structural evolution inferred by maps and geological profiles. The type and rate of movement along the Holy Cross Fault during its geological history was quantified. The construction of the model shows the great significance of Devonian subsidence in the area, as well as the importance of Variscan orogeny. Dispersion of the data suggests that the Mesozoic burial history was slow and multiphase. The results testify the role of Laramide orogeny and the lack of significant phases after that.

## RIASSUNTO

L'area delle Holy Cross Mountains, situata nella Polonia centro-meridionale, possiede caratteristiche che la rendono particolarmente interessante per studi geologici, in particolare, il ruolo della Holy Cross Fault e le tempistiche dell'evoluzione tettonica devono ancora essere valutate. Mediante l'uso congiunto della termocronologia e di programmi di modellazione strutturale si è proceduto a caratterizzare l'evoluzione tettonica della zona. In particolare, grande uso hanno avuto termocronometri di bassa temperatura come l'analisi (U-Th)/He e delle tracce di fissione, entrambe eseguite su apatiti. I campioni prelevati in campagna sono stati lavorati fino ad ottenere cristalli utili per le analisi. Le età termocronologiche sono state utilizzate per vincolare e chiarire l'evoluzione strutturale ricavata dall'analizi di mappe e profili geologici. Particolare attenzione è stata data alla quantificazione del tipo e del rateo di movimento lungo la Holy Cross Fault durante la storia geologica. La costruzione del modello mostra la grande rilevanza della subsidenza devoniana dell'area, nonchè la spiccata importanza dell'orogenesi Varisica. La dispersione dei dati suggerisce inoltre una storia mesozoica lenta e multifase. I risultati ottenuti testimoniano il ruolo dell'orogenesi Laramide e la mancanza di fasi successive significative.

# TABLE OF CONTENTS

# CHAPTER ONE

# INTRODUCTION

## 1.1. SUMMARY

The present work covers the area of the Holy Cross Mountains, located in the southern part of the central Poland. The goal of the study is to reconstruct the tectonic evolution of this region by analysis of the burial and thermal history through low temperature thermochronology. A restored section, crossing the main tectonic structures and stratigraphic horizons, has been therefore achieved and provides the key information to define the main evolutionary steps.


Fig. 1.1 Satellite view of Central Europe

The study area represents an important region for understanding the tectonic evolution of central Europe.

Indeed, the chief feature of the tectonics of Europe is its partition into two different regions: the ancient East European Craton and the areas which surround it, involved in Phanerozoic orogenies. The boundary between these two regions runs through the centre of Poland. Since in northern and central Poland the substratum is usually overlaid by a thick, continuous Quaternary cover, the Holy Cross Mountains and the surrounding areas are essential, considering the abundance of outcrops. In fact, they are structured in a quite extensive tectonic culmination (belonging to the Mid-Polish Anticlinorium) and, thanks to their convexity, several lithostratigraphic units can be seen through the region, exposing a nearly complete succession of Phanerozoic strata.

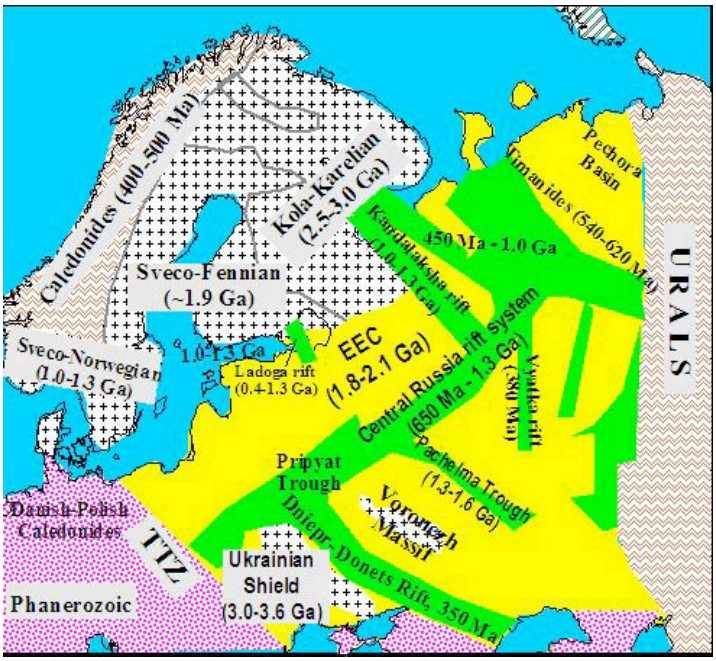


Fig. 1.2 Main geological features of northern and eastern Europe: East European Craton (EEC), West European Platform (WEP) phanerozoic, Tornquist–Teisseyre Zone (TTZ).

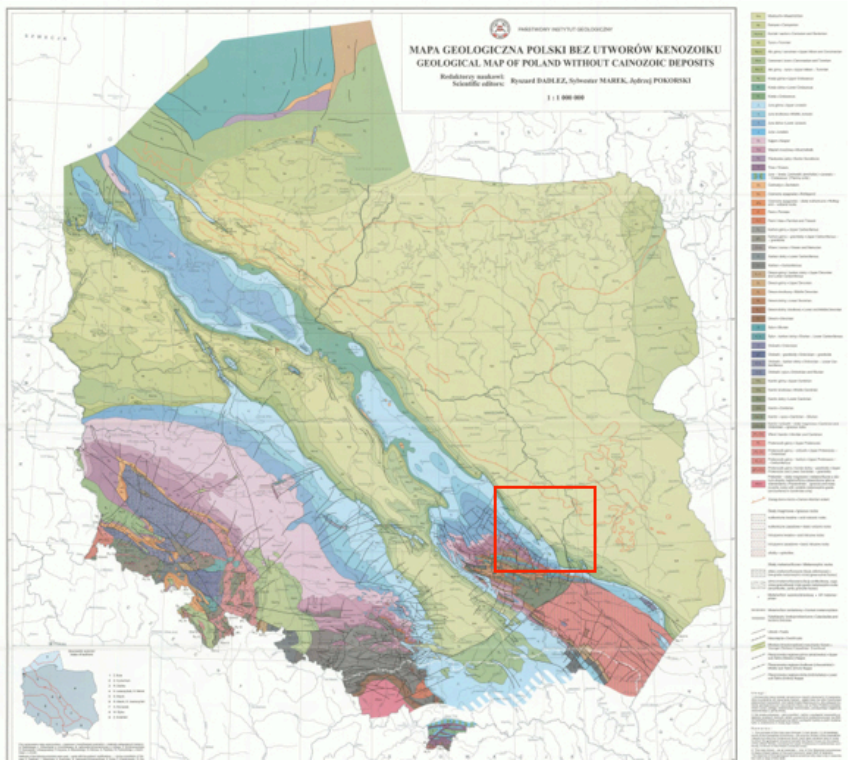


Fig. 1.3 Geological map of Poland. In the red rectangle lies the study area.

The best methodology for reconstruction of thermal and burial-exhumation history requires the use of low temperature thermochronology techniques. Thermochronology provides information about the thermal history of the rock by comparing the radiometric dates of two or more minerals with different closure temperatures. Among the many isotopes and minerals that can be used, two thermochronometers have been used owing to their relatively low closure temperatures. The apatite (U-Th)/He and the apatite Fission Track analysis belong to this "low temperature thermochronology", hence they are sensitive to vertical movements in the uppermost portion of the crust and suitable in order to reconstruct quantitatively the recent evolution of the area.

## 1.2. GOALS OF THE STUDY

This study aims to the reconstruction of the tectonic evolution of an area that is well-studied in a qualitative way, but lacks of more modern quantitative analysis. The goal of the work are the quantification of burial evolution and exhumation times and processes, that leads to the reconstruction of kinematic evolution of Holy Cross Mountain and the definition of the tectonic model of the area.

## 1.3. THESIS OUTLINE

The aim of this first chapter is to provide a brief introduction of the area and the capital methods. Furthermore, the goals of the work are underlined.

Chapter 2 provides the geological setting of the region: an overview on a large scale then on a local scale is supplied, along with the description on the main lithostratigraphic units and a summary concerning the tectonic and the geological history..

Chapter 3 includes the description of the methods: the low temperature thermochronometers employed -the apatite (U-Th)/He and the apatite Fission Track analysis- are explained, besides the software used for the collection and the analysis of the maps, the modelling and the construction of the restored section.

Chapter 4 describes the materials on which the analysis has been performed, and the basic procedures for it.

Chapter 5 presents the data obtained from the analysis, displayed through tables and diagrams and subsequently discussed. Within the chapter are also presented the main steps which lead to the creation of the restored section.

Chapter 6 deals with discussion and interpretation of the thermochronological data.

In Chapter 7 all the knowledges and the informations are related and discussed, in order to summarise the whole work.

Eventually, the conclusion of the work are presented in Chapter 8.

# CHAPTER TWO

# GEOLOGICAL SETTING

## 2.1. GEOLOGICAL CONTEXT

As stated in the previous chapter, the study area has a distinctive position within the Europe.

The Holy Cross Mountains (Góry Świętokrzyskie in Polish, henceforward referred as HCM) are located in the southern part of Central Poland, a zone of interest since crossed by the Trans-Europe Suture Zone (TESZ), a broad structural corridor which separates the East European Craton (EEC) from Western European Platform (WEP) comprehending the Variscan and Alpine orogens. Specifically, the northern boundary of the TESZ is termed Tornquist–Teisseyre Zone (TTZ) (Guterch et al.,1986) (Berthelsen, A., 1993), which trends NW–SE, running from the Baltic Sea (Pomerania, Poland) to the Black Sea (Dobrogea, Romania). The origin of TTZ goes back to the Cambrian and, at least during the late Palaeozoic, was often reactivated (Pozaryski et al., 1982).

The Baltic Shield, the Russian Platform and the Ukrainian Shield constitute the original mass of the EEC, which is mostly made up of gneiss and granite that were formed mostly during the Archean (2600 Ma) and consists of gneiss and granite which were repeatedly altered by rejuvenation processes.

The WEP lies southwest of the EEC, and is constituted of more recent terrains belonging to the Variscides and the Alpides. The Varisican complex consists in folded structures developed during the Varisican orogeny that occurred from Upper Carboniferous to Lower Permian. The development of this belt started at different times in diverse areas owing to dissimilarities in the plasticity of the basement. The Alpides occupy the most southerly E-

W zone in Europe and derive from the Alpine orogeny between the Upper Triassic and the Middle Miocene.

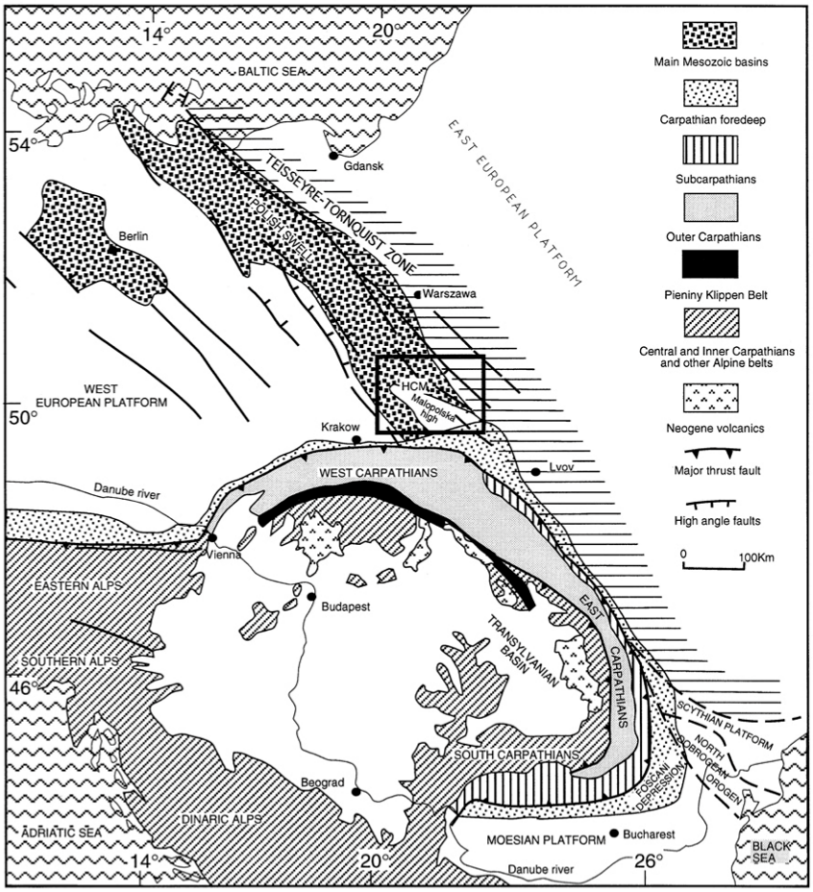


Fig. 2.1. Main structural units of central Europe showing the Teisseyre–Tornquist Zone that separates the Western and Eastern European Platforms, also called 'Russian platform' (modified after Roure et al., 1993). The square indicates the studied area, HCM Holy Cross Mountains.(J. Lamarche et al., 1999)

Despite their importance, the HCM occupy a relatively small area, ca. 1700 km², 90 km long and 30 km wide. The structure extends WNW–ESE, following the main strike direction of the Holy Cross Fault.

The HCM, which belongs to the Malopolska Massif, are located within the Tornquist–Teisseyre Zone, which, in this area, does not coincide strictly with the margin of the EEC along its whole length but rather it runs parallel to the north.

The Palaeozoic basement of the HCM is adjacent to the southwest part of the Precambrian EEC. It is composed of two tectonic units, which are

lithologically, stratigraphically, and tectonically distinct (Czarnocki, 1938, 1957; Mizerski, 1988): the Łysogóry unit (LU) to the north and the Kielce unit (KU) to the south, separated by the previously mentioned Holy Cross Fault (HCF). The HCF is a regional fault which seems connected to deep structures at the Moho discontinuity. North of this structure, the crustal thickness is about 50-52 km whereas south of it is about 43-45 km (Guterch et al., 1984). The Łysogóry and Kielce units are thought to have been separated during the early Palaeozoic (Lewandowski, 1992; Stupnicka, 1992). Paleomagnetic studies suggest the Kielce unit was probably a sliver of the Baltic Shield detached from the ancestral region and transferred along the margin of the HCF during Variscan times. More uncertain is the origin of the Łysogóry unit. The Bouguer anomalies suggest that this unit can be considered as an epicratonic element of the Eastern European Platform (Dadlez R., 2001), while paleontological evidences suggest that it is a peri-Gondwanan-derived terrane which did not reach the Baltic realm before Ordovician times (Valverde-Vaquero et al., 2000)

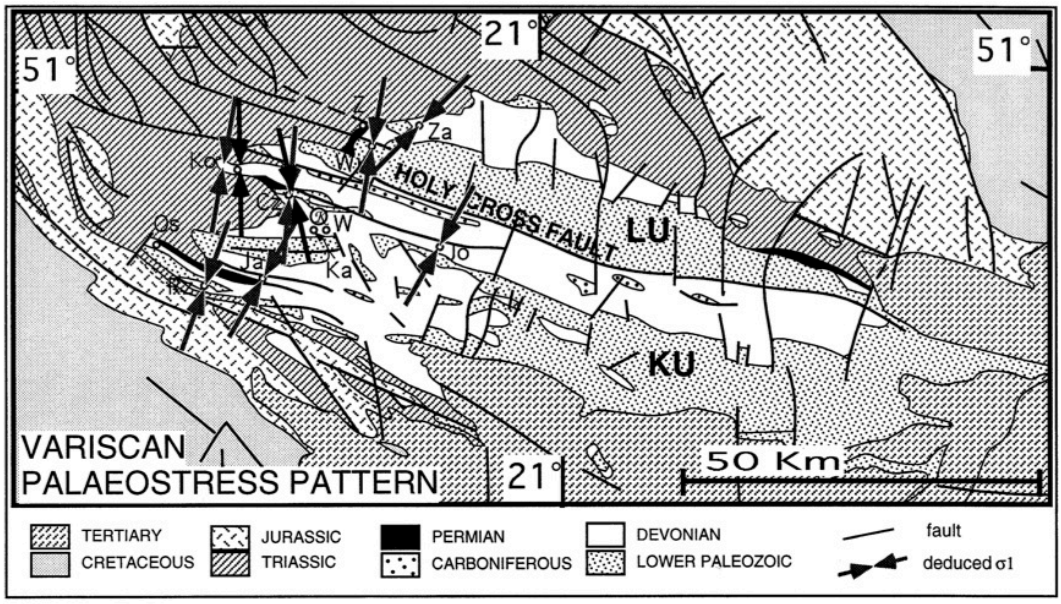


Fig. 2.2. Geological map of the Holy Cross Mountains (modified after Osika et al., 1972) and Variscan palaeostress pattern. The main Variscan deformation resulted from a N–S to NNE–SSW shortening. KU D Kielce unit; LU D Łysogóry unit; K D Kielce town. (J. Lamarche et al., 1999)

## 2.2. STRATIGRAPHY

In this chapter, a basic description of the main lithostratigraphic units is provided.

- ***Precambrian unit***. It is found mostly between the HCM and the Carpathians and consists of phyllites slates and meta-argillites with arkose intercalations. It has been dated to a range between 706 Ma and 625 Ma (Upper Proterozoic). These rocks always dip very steeply and are characterised by an intense metamorphism that discriminates them from the Cambrian Unit. The folding of this unit probably took place in the early phase of the Baikalian Orogeny. Several volcanic layers indicate the occurrence of a significant magmatism.
- ***Cambrian unit***. It is exposed mainly in an east-west belt running south of Chęcin. These rocks are greyish-green and brownish-crimson clay shales, with bands of siltstone and sandstone and laminae of calcareous-dolomitic rocks. Tuffites, metamorphic and volcanic clasts are also present. Some epimetamorphism can be present.
- ***Ordovician unit***. This succession have an irregular distribution, probably due to the scarce thickness. The strata are constituted of sandy-calcareous facies, typical of shallow platform sedimentation. The presence of graptolites shales suggests graben-like subsidence. However, the unit formed under synrift to post-rift conditions.
- ***Silurian unit***. Outcrops, although discontinuous, can be found in the eastern part of the Kielce and Łysogóry blocks. Its thickness is much higher than the Ordovician unit. Strata are composed mainly of mudstones, claystones and marly claystones with graptolites and no sandy sediments are present.
- ***Devonian unit***. The Lower Devonian is made of red sandstones, deposited in a terrigenous-marine environment. The Middle and Upper

Devonian is made up by limestones, with shallow laminae of marls in the upper area.

- ***Carboniferous unit.*** it is present only in the western part of the Małopolska block (western margin of the Lower San Horst) due to the massive erosion during the Variscan inversion. It is made of siliceous shales and occasionally siderites. Syn-thrust deposition.
- ***Permian unit***. The lower part is made of conglomerates, while the upper part is composed mainly by limestones, in lesser degree by siltstones and mudstones. Transition from continental to shallow marine deposits (Konon, 2004). There are some evidence of intense volcanic activity, especially in the lower part.
- ***Triassic unit***. The Lower Triassic sequences is characterised by terrigenous red-beds, while the Middle Triassic is developed as an extensive carbonate-evaporite platform with open marine influences from the south. In the Late Triassic deposition of continental red-bed resumed, with intermittent evaporite development. (Dadlez at al. 1995).
- ***Jurassic unit***. It is exposed mostly near the Polish-Ukrainian border. The Lower Triassic consists of clay and sandstones, while Middle Jurassic includes both mudstones and limestones, with clays laminae. The Upper Jurassic is made up by carbonates with sandstones intercalations.
- ***Cretaceous unit***. Outcrops can be found along the SE margin of the Lubaczów Horst, close to the Polish-Ukrainian border. The Lower Cretaceous comprises thick limestones and dolomites, likewise the Upper Cretaceous.
- ***Miocene unit***. In the HCM, this succession consists in thin lenses that covers the Mesozoic like a pellicle of few meters. Principally made up of pink limestones with sand laminae.

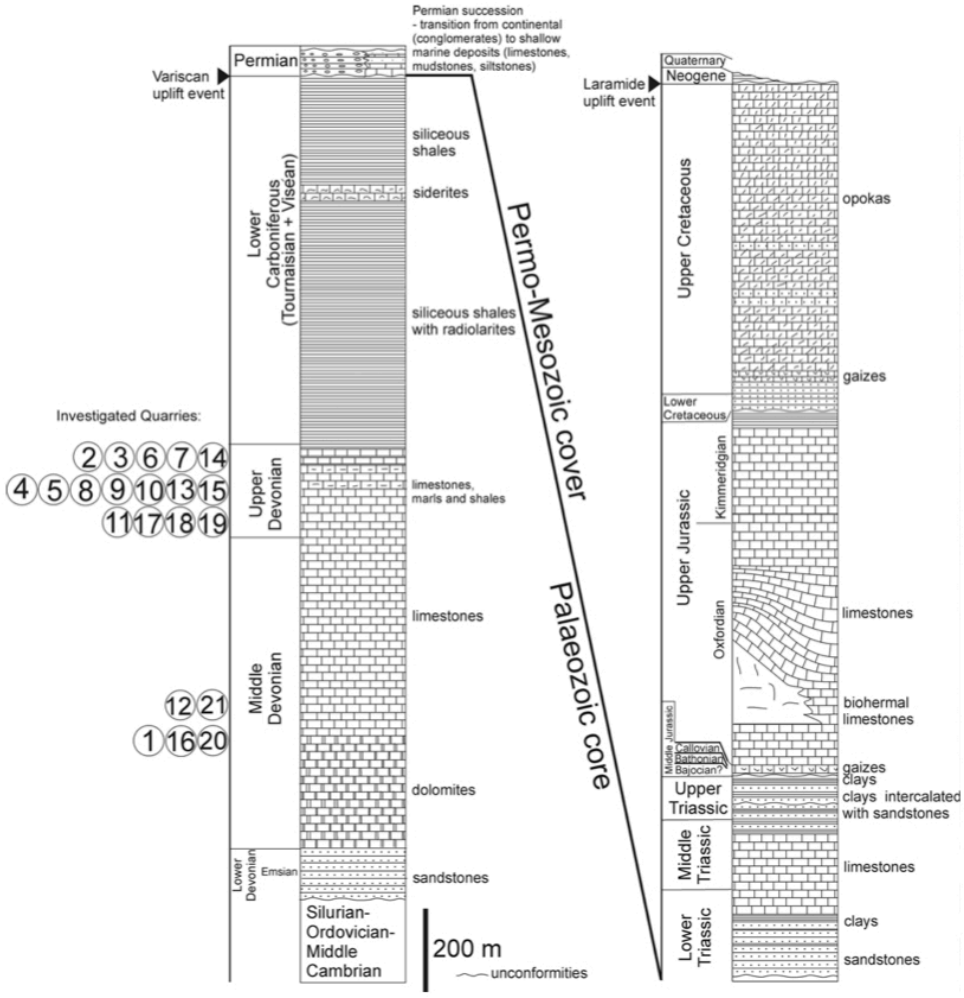


Fig. 2.3. Paleozoic and Mesozoic succession of the Holy Cross Mountains.

## 2.3. THERMAL SETTING

The present day heat flow values in the area of the HCM are interpolated from a map of surface heat flow in Poland and can be generically assumed between 46 mWm-2 and 50 mWm-2 (Karwasiecka and Bruszewska, 1997). Evaluation of the heat flow values in the past is much more difficult and it is generally based on vitrinite reflectance values. The best-fit curves on the dataset given by Marynowski (1998) (Fig. 2.3. A, curves a,b, B curves a) thus achieved suggests, that the heat flow through Palaeozoic and Mesozoic was constantly lower, about 30-35 mWm-2, than the present.

The same model allows an alternative thermal setting that, although the low fitting with vitrinite data, have much more congruence with the geodynamic context of the area. As seen in Fig. 2.3. A, curves d, B curves c) a moderate to slightly elevated Variscan (Carboniferous-Early Permian) heat low of 70-80 mWm-2 can be presumed, particularly in an elongated zone south of the Holy Cross Fault, rapidly decreasing during the Permian to values lower than present (ca. 30-35 mWm-2), and then slowing increasing up to the current values since the Cenozoic (Narkiewicz et al., 2010).

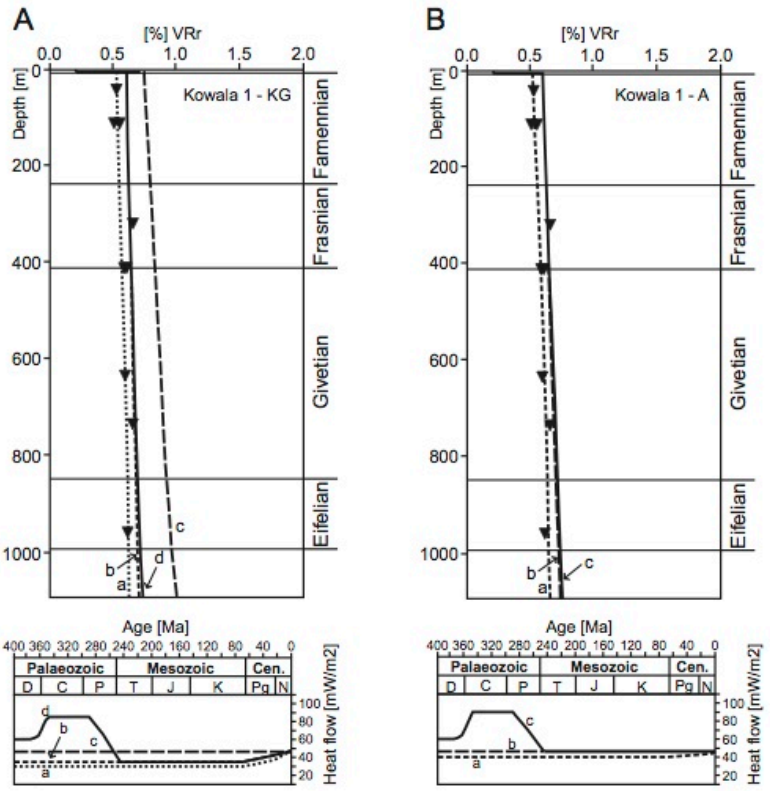


Fig. 2.4. [Measured (triangles) versus calculated (curves) vitrinite reflectance in kowala 1 well for different heat flow histories. a) variant kg. B) variant a](Narkiewicz et al., 2010) Variant KG implies thicker Permian-Mesozoic units and higher inversion magnitude; Variant A interpreted a continuous sedimentation until Hauterivian.

## 2.4. TECTONIC EVOLUTION

The most ancient part of the HMC is the Precambrian succession. The Upper Precambrian outcrops, often found between the HCM and the Carpathian Mountains, belongs to the Baikalian complex that originated during the Baikalian orogeny in the Upper Proterozoic (850-570 Ma). During the early phase of this orogeny, a geosyncline was formed and persisted, migrating to the north, up to the Middle Cambrian (520 Ma). Throughout the Lower and Middle Cambrian (570-520 Ma) the massifs were exposed to intense diagenesis and became peneplaines. The geodynamic setting of Late Cambrian is quite debated: in fact, the Upper Cambrian beds are arranged in a number of asymmetric folds dipping toward the north, the strike of which is incompatible with the Caledonian orogeny. The occurring of this folds has been largely discussed, but it can be supposed due to the Sandomirian orogeny, the early phase of the Caledonian orogeny, that took place from the Ordovician to the early Devonian (490-390 Ma). Despite of the ongoing orogeny, there are evidences that the Ordovician and Silurian strata deposited under extensional conditions. Moreover, it is generally assumed that Ordovician and Silurian subsidence in the Kielce and Łysogóry blocks resulted from flexural bending of the foreland plate related to the formation of the Caledonide foredeep (Poprawa et al., 1997; Poprawa, 2006a; Narkiewicz et al., 2010). Within the basin thus created, the sedimentation of Silurian mudstones occurred in post-rift conditions, leading to the progressive filling and hence to a forced marine regression.

During the Devonian, the rifting resumed, and the renewed subsidence allowed the emplacement of a thick carbonate platform, the depth of which varies though the region.

The original thickness of the Kielce platform is hard to define due to the intense erosion which occurred because of Variscan inversion (evaluation of

this value is among the goals of this work, and will be achieved by thermochronology).

During the Variscan orogeny (Late Devonian to Triassic), Laurasia and Gondwana collided to form the Pangea supercontinent. The HCM were affected by a new uplift episode, with an evident relief inversion. All the strata from Precambrian to Carboniferous are intensely folded. The palaeostresses deduced from the measurements of fold axes and the bedding attitude indicate the direction of Variscan shortening as trending N–S to NNE–SSW in both Kielce and Łysogóry units (J. Lamarche et al., 1999). As a consequence of this phase, both the Devonian and the Carboniferous units are massively eroded and their tops are marked by unconformities. In this period, as previously stated, the thermal gradient is much higher than the present, and intensive hot fluid activity is evident. Distribution of thermal maturity suggests an important role of HCF zone and its western prolongation as a carrier way for fluid migration during the Late Palaeozoic time (Belka 1990; Poprawa, Zywiecki 2005).

The uplift lasted until the Mesozoic, when an important subsidence phase took place. Relief inversion is recorded by the Permian succession, in which a transition from continental conglomerates to shallow marine limestones can be seen.

The Permian-Mesozoic is dominated by the development of an epicontinental basin. The Polish Basin formed the easternmost part of the Permian-Mesozoic middle European basin (Dadlez, 1989a; Ziegler, 1990), bordered to the east by the elevated EEC and to the southwest by the Bohemian Massif. The main depocentral axis of the Polish Basin lies parallel to the edge of the EEC, and this boundary is related to the distinct structural features of the TTZ.

The deposition shifted from terrigenous to carbonate-platform-like through the Early to the Middle Triassic, while continental-like sedimentation was dominant during the Late Triassic and Early Jurassic, which, however,

includes a considerable proportion of marginal and open marine facies. Siliciclastic sedimentation partially continued to the Middle Jurassic, which was developed, however, entirely in an open marine environment. In central and southern Poland, during the Late Jurassic, a thick carbonate platform with anhydrite and halite deposits took place, marking the incipient marine regression.

Open marine and marginal marine siliciclastic depositional systems prevailed during the Early Cretaceous, until when marine transgression lead to the development of an open marine carbonate platform which persisted beyond the Late Cretaceous until the Early Paleocene (Dadlez at al. 1995). A last orogenic phase, the so-called Laramide orogeny (Late Cretaceous to Late Paleocene), produced a new inversion which locally led to the removal of an abundant part of Mesozoic sediments and finally to the exposure of the Palaeozoic core of the HCM (Kutek and Głazek, 1972; Kutek, 2001) which roughly acquire their present shape. The Mesozoic cover is overlaid by the Miocene marine succession, which is related to the development of Carpathian foredeep and forebulge. A Miocene subsidence is then associated to extensional reactivation of faults that dissected also the Mesozoic–Palaeozoic successions along the TTZ (Kosakowski et al., 2013).

# CHAPTER THREE

# METHODS

## 3.1. INTRODUCTION TO THE CHAPTER

The following section describes methods applied on the samples during this work.

Two different methods can be identified, both of them aiming to the same result: reconstructing the burial and thermal history of the HCM and constrain the main evolutionary steps of the area.

The first method that will be discussed is the thermochronology, particularly the low temperature branch of this discipline and its application on apatite crystals.

A second part will provide a description of the modelling software used in the structural reconstruction and the geological maps acquisition from external sources.

### 3.1.1. APATITE

Either the (U-Th)/He and the Fission Track analysis can be performed both on zircon and apatite crystals. The four thermochronometers are characterised by different $T_c$ and sensitivities but the whole of them belong to the lower temperature thermochronology.

In this work, the analysis have been performed just on apatites and cover the coolest temperature ranges of all the thermochronometers.

The term "apatite" identifies a group of similar isomorphous hexagonal phosphate minerals, following the chemical formula $Ca_5(PO_4)_3(F,Cl,OH)$.

The focus on apatite arises from its ubiquity and moderately high U and Th content, but more importantly because He accumulation in apatite occurs

only at temperatures below 70-75°C . At higher temperatures diffusion removes He as fast as it is produced by decay (Todd A. et al., 2003).

Apatite is a common accessory mineral in igneous, metamorphic and clastic sedimentary rocks. It is a widely spread phase in igneous series, common in rocks of all metamorphic grades and virtually ubiquitous in clastic sedimentary rocks. Hence, the thermochronology applied on this mineral is a basic tool for several geodynamic purposes.

## 3.2. THERMOCHRONOLOGY: THEORY

Thermochronology can be defined as the quantitative study of the thermal histories of rocks using temperature-sensitive radiometric dating methods, which are based on the comparison between the observed abundance of a naturally occurring radioactive isotope and its decay products. The dating is achieved through well-known decay rates equations, and the calibration on a vertical succession of strata previously recognised with basic geologic principles.

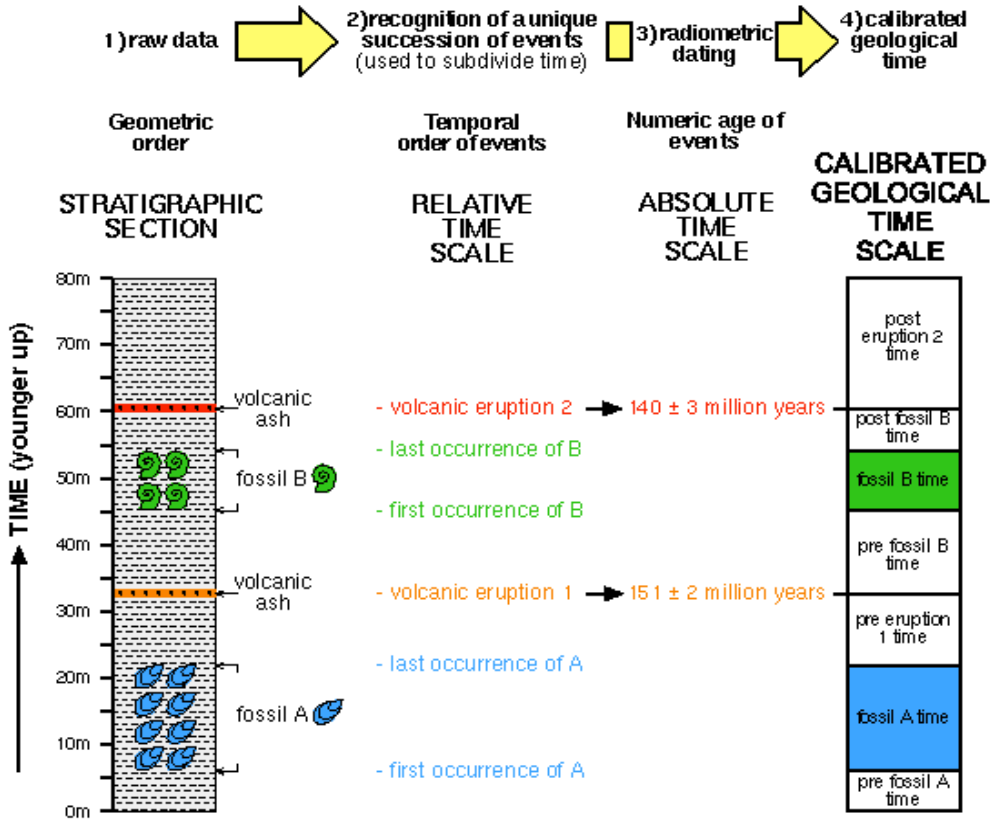


Fig 3.1 How relative dating of events and radiometric (numeric) dates are combined to produce a calibrated geological time scale. In this example, the data demonstrates that "fossil B time" was somewhere between 151 and 140 million years ago, and that "fossil A time" is older than 151 million years ago. Note that because of the position of the dated beds, there is room for improvement in the time constraints on these fossil-bearing intervals (e.g., you could look for a datable volcanic ash at 40-45m to better constrain the time of first appearance of fossil B)

The decay rates equations can be calculated for different isotopes. Therefore, several radioisotopic systems can be evaluated and distinct minerals can be used. The term "thermochronometer" defines a radioisotopic system consisting of radioactive parent, radiogenic daughter or crystallographic feature, and the mineral in which they are found (Reiners et al. 2005). Each one is characterised by a particular precision and, most importantly, an its own closure temperature and sensitivity.

The closure temperature (Tc) can be defined as the temperature of a system at the time given by its apparent age. The closure of a thermochronometer occurs through a range of decreasing temperatures for which the retention of products of the decay by the system progressively increase from 0% at

the base (maximum temperature) to 100% at the top (minimum temperature): this temperature interval is defined Partial Retention Zone (PRZ) (Andreucci B., 2013).

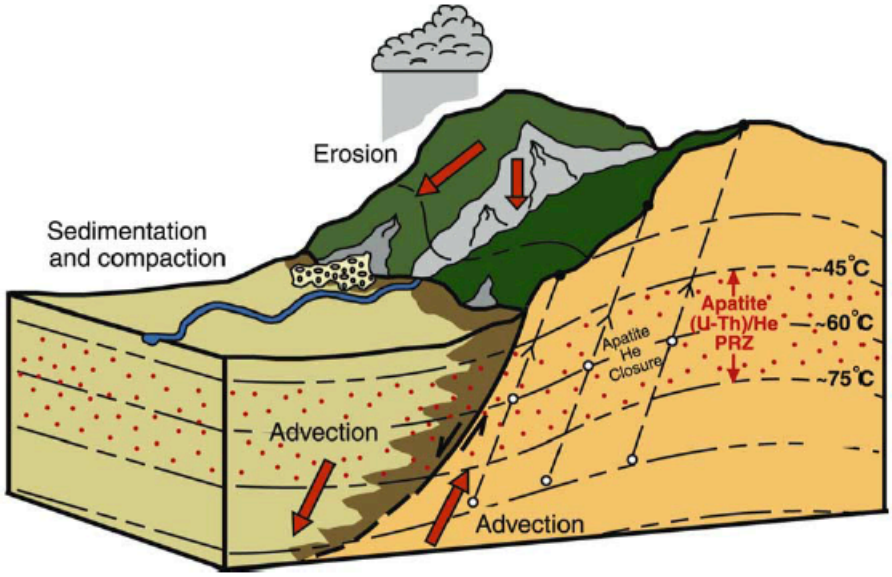


Fig. 3.2 Thermal processes in a normal-fault bounded range that influence the interpretation of apatite (U-Th)/He data. Isotherms (dashed lines) are curved from advection of mass and heat (red arrows) in the footwall and hanging wall, and by topographic relief.
Rocks in the subsurface (open circles) are exhumed and sampled at the surface (filled circles). The stippled red zone between 45 and 75°C represents the helium partial retention zone (HePRZ) where helium diffusion is neither fast enough to maintain a zero concentration, nor slow enough for complete retention of helium.

Among the several thermochronometers, a branch of them are most sensitive to low temperatures (typically within a range of 40°C and 125 °C for durations of heating and cooling in excess of 10^6 years); the most common are the apatite fission track (AFT) and apatite (U–Th)/He (AHe), which are used to investigate the tectonic within the upper part (1-3 km) of the Earth's crust.

PRZ for AHe varies between ca. 20°C and 60°C, whereas closure temperatures are in the range 40°C-80°C, for cooling rates of 10°C/Ma and diameter of the spherical domain of 60 μm, AHe Tc=67°C (Reiners and Brandon, 2006).

The $^{4}He$ production–diffusion model predicts that the $T_c$ of AHe will vary with cooling rate and effective parent isotopes concentration, and may differ from the commonly assumed $T_c$ of 75 °C $Ma^{-1}$ by up to ±15 °C (Farley et al. 1996).

The AFT PRZ values are generally comprised between 30°C and 130°, but can be significantly different depending on cooling rate and apatite chemistry. AFT $T_c$s generally vary between ca 80°C and 120°C, but still being largely affected by apatite composition. An apatite of "average" composition (Ketcham et al., 1999) has, for cooling rates of 10°C/Ma, $T_c$=116°C.

After a thermal history dataset is achieved, numerical or analytical thermal models can be used to quantify the cooling processes. Thermal models can be used to simulate the exhumation-burial history of the sample, through different computer programs which allow both forward and inverse modelling.

Table 3.1
Summary of commonly used thermochronometers and features.

| ***Decay System*** | ***Mineral*** | | ***Approximate precision*** **(%, 1 σ)** | ***Closure Temperature*** **(°C)** | ***Activation Energy*** **(kJ/mol)** | ***References*** |
|---|---|---|---|---|---|---|
| (U-Th)/Pb | zircon | | 1–2 | >900 | 550 | Cherniak and Watson (2001); Cherniak (2001) |
| | titanite | | 1–2 | 550–650 | 330 | Cherniak (1993) |
| | monazite | | 1–2 | ~700 | 590 | Cherniak et al. (2004) |
| | apatite | | 1–2 | 425–500 | 230 | Chamberlain and Bowring (2001); Cherniak et al. (1991) |
| 40Ar/39Ar | hornblende | | 1 | 400–600 | 270 | Harrison (1981); Dahl (1996) |
| | biotite | | 1 | 350–400 | 210 | Grove and Harrison (1996); Harrison et al. (1985) |
| | muscovite | | 1 | 300–350 | 180 | Robbins (1972); Hames and Bowring (1994) |
| | K-feldspar | | 1 | 150–350 | 170–210 | Foland (1994); Lovera et al. (1991; 1997) |
| Fission-track | titanite | | 6 | (a) 240–300 (b) 380–420 | 440–480 | (a) Coyle and Wagner (1998); (b) Watt and Durrani (1985); Naeser and Faul (1969) |
| | zircon | (a) zero-damage (b) natural | 6 | (a) 330–350 (b) 230 | (a) 300–350 (b) 210 | (a) Tagami et al. (1998); Rahn et al. (2004) (b) Brandon and Vance (1992); Brandon et al. (1998) |
| | apatite | | 8 | 90–120 | 190 | Laslett et al. (1987); Ketcham et al. (1999) |
| (U-Th)/He | titanite | | 3–4 | 160–220 | 190 | Reiners and Farley (1999) |
| | zircon | | 3–4 | 160–200 | 170 | Reiners et al. (2004) |
| | apatite | | 3–4 | 55–80 | 140 | Farley (2000) |

Note: Approximate precisions are estimated values for age determinations; for TIMS U/Pb measurements precisions can be considerably better than cited here. Closure temperatures calculated using Dodson (1973) [or, for fission-track, Dodson (1979) using the 50% annealing isopleth (fanning models); also see Brandon et al. (1998)] using typical ranges of grain sizes and cooling rates (1–100 °C/m.y.) (small grains/low cooling rate and large grains fast/cooling rate). Also see Hodges (2003) for a similar and more complete compilation.

### 3.2.1. (U-Th)/He THERMOCHRONOLOGY

Uranium-Thorium dating is based on the detection by mass spectrometry of both the parent ($^{234}U$) and daughter ($^{230}Th$) products of decay, through the emission of an alpha particle, and it is part of the much longer decay series beginning in $^{238}U$ and ending in $^{206}Pb$ (Reiners et al. 2005 and Lisker et al., 2013).

AHe thermochronology relies on the accumulation of $^{4}He$ during the α-disintegration of $^{238}U$, $^{235}U$, $^{232}Th$, their daughter products and, $^{147}Sm$. The $T_c$ of mineral grains is dependent on activation energy, a geometry factor for the crystal shape, the thermal diffusivity ($D_0$), the length of the average diffusion pathway from the interior to the surface of the grain and the cooling rate at $T_c$.

The He ingrowth equation assumes absence of 4He, both initial and produced by sources extraneous to the crystal, and secular equilibrium among all daughter products in the decay chain. In addition, 4He diffusion in apatite is impeded by radiation-induced damage to the apatite structure. A careful selection of the crystal is therefore required, to avoid grains affected by pervasive inclusions or broad coating. This procedure will be described more carefully in the following paragraph dealing with the samples preparations.

The equation for He ingrowth in time (t) is:

$$^{4}He = 8^{238}U(e^{\lambda_{238}t}-1) + 7^{235}U(e^{\lambda_{235}t}-1) + {}^{232}Th(e^{\lambda_{232}t}-1) + {}^{147}Sm(e^{\lambda_{147}t}-1)$$

where He, U, Th and Sm refer to present-day amounts, and λ is the decay constant.

In Table 3.2 the values and features of the principal decay systems are shown.

Table 3.2
Geologically useful long-lived radioactive decay schemes

| Parent | Decay Mode | λ | Half-life | Daughter | Ratio |
|---|---|---|---|---|---|
| $^{40}K$ | $\beta^+$, e.c, $\beta^-$ | $5.543 \times 10^{-10} y^{-1}$ | $1.28 \times 10^{9} yr$ | $^{40}Ar$, $^{40}Ca$ | $^{40}Ar/^{36}Ar$ |
| $^{87}Rb$ | $\beta^-$ | $1.42 \times 10^{-11} y^{-1}$ | $4.8 \times 10^{10} yr$ | $^{87}Sr$ | $^{87}Sr/^{86}Sr$ |
| $^{138}La$ | $\beta^-$ | $2.67 \times 10^{-12} y^{-1}$ | $2.59 \times 10^{11} yr$ | $^{138}Ce$, $^{138}Ba$ | $^{138}Ce/^{142}Ce$, $^{138}Ce/^{136}Ce$ |
| $^{147}Sm$ | α | $6.54 \times 10^{-12} y^{-1}$ | $1.06 \times 10^{11} yr$ | $^{143}Nd$ | $^{143}Nd/^{144}Nd$ |
| $^{176}Lu$ | $\beta^-$ | $1.94 \times 10^{-11} y^{-1}$ | $3.6 \times 10^{10} yr$ | $^{176}Hf$ | $^{176}Hf/^{177}Hf$ |
| $^{187}Re$ | $\beta^-$ | $1.64 \times 10^{-11} y^{-1}$ | $4.23 \times 10^{10} yr$ | $^{187}Os$ | $^{187}Os/^{188}Os$, $(^{187}Os/^{186}Os)$ |
| $^{190}Pt$ | α | $1.54 \times 10^{-12} y^{-1}$ | $4.50 \times 10^{11} yr$ | $^{186}Os$ | $^{186}Os/^{188}Os$ |
| $^{232}Th$ | α | $4.948 \times 10^{-11} y^{-1}$ | $1.4 \times 10^{10} yr$ | $^{208}Pb$, $^{4}He$ | $^{208}Pb/^{204}Pb$, $^{3}He/^{4}He$ |
| $^{235}U$ | α | $9.849 \times 10^{-10} y^{-1}$ | $7.07 \times 10^{8} yr$ | $^{207}Pb$, $^{4}He$ | $^{207}Pb/^{204}Pb$, $^{3}He/^{4}He$ |
| $^{238}U$ | α | $1.551 \times 10^{-10} y^{-1}$ | $4.47 \times 10^{9} yr$ | $^{206}Pb$, $^{4}He$ | $^{206}Pb/^{204}Pb$, $^{3}He/^{4}He$ |

Note: the branching ratio, i.e. ratios of decays to $^{40}Ar$ to total decays of $^{40}K$ is 0.117. $^{147}Sm$ and $^{190}Pt$ also produce $^{4}He$, but a trivial amount compared to U and Th.

This equation can be simplified, assuming that the ratio of 238U to 235U has in the solar system a constant value of 137.88 in all rocks. However, new studies do not agree on this value, stating that many naturally occurring uranium-rich minerals, such as zircon, actually have a lower 238U/235U ratio, with an average of 137.818 ± 0.045 (the uncertainty assigned to this value relates to the variation observed between different samples). Agreement between these results, other rocks, and meteorites indicate that the new average 238U/235U value and uncertainty may also be representative of the Earth's 'bulk' uranium isotopic composition (British Geological Survay, 2012).

$$^{4}He = 8^{238}U(e^{\lambda_{238}t} - 1) + 7\left(\frac{^{238}U}{137.88}\right)(e^{\lambda_{235}t} - 1) + 6^{232}Th(e^{\lambda_{232}t} - 1) + ^{147}Sm(e^{\lambda 147 t} - 1)$$

The cooling age equation cannot however be directly solved , since the daughter 4He has different potential parent isotopes which can not be differentiated on the base of their role in the production of the 4He. On this purpose, the value of t is approximated using a Taylor series approximation, which can be simplified as (M. Fellin, personal communication):

$$t_1 \approx ({}^4He - f(t_0) + t_0 \cdot f'(t_0)) / f'(t_0)$$

The value of t1 is expressed as the "raw date" (see the datasets in Chapter 4), and represents the uncorrected cooling age of the sample, an underestimation of the true cooling age because of α-particle ejection, which is discussed later.

### 3.2.1.1. α-EJECTION CORRECTION

As previously stated, the value of t1 explicited in the equation 2, expresses the "raw date", an underestimation of the true age of the sample. In fact, it is possible that some He loss occurred by ejection of α particles outside the crystal domain, namely the "α-particle ejection".

When a parent isotope goes through α-decay, the α particles emitted travels a certain distance from the site of decay owing to the kinetic energy of the reaction. In apatites (and zircons) this distance is ca. 20 μm. Should the decay occur within this span from the crystal edge, there is a statistical certainty that some daughter product will be ejected from the crystal lattice, injected in the surrounding phases and lost to the environment. The loss of α particles leads to an underestimation of the age of the crystal, which needs to be revised. Since the magnitude of α-ejection is controlled by surface to volume ratio, spatial distribution of the parent atoms and medium specific diffusion values, the correction is mainly based on geometric parameters. Therefore, to account for α-ejection it is a common practice to measure the physical dimensions of the crystal to be dated and to calculate an homogeneous α-ejection correction factor (HAC), to which the raw date has to be multiplied, to obtain the age corrected for ejection (Farley, 2002).

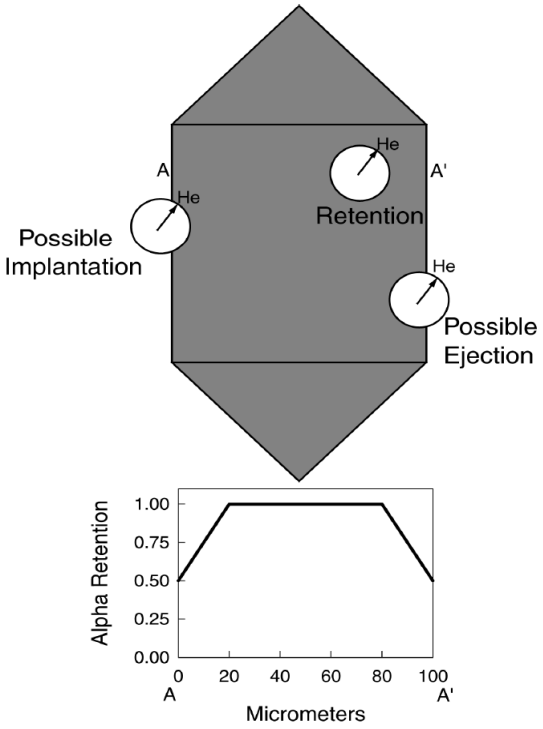


Fig. 3.3 The effects of long α−stopping distances on He retention (from Farley, 2002) . The upper figure illustrates the three possibilities within a schematic crystal: α retention, possible α ejection, and possible α implantation. The centre of the circle denotes the site of the parent U or Th nuclide, and the edge of the white circle labeled He indicates the locus of points where the α particle may come to rest; the arrow indicates one possible trajectory. The lower plot shows schematically how α retention changes from rim to core to rim along the path A-A'; exact equations defining the shape of this curve as a function of grain size were given by Farley et al. (1996)

### 3.2.1.2. PROBLEMS

Misunderstandings in the evaluation of the age of the sample are possible. The appraisal of the HAC is rather influenced by the rightfulness of the measurements. Correction values of 0.75-0.90 are common, however this value can increase or decrease significantly with changes in grain size or poor grain geometry. This problem is exaggerated by abrasion and rounding of the grains. Furthermore, inclusions and coating can also be misleading, since they constitute external sources of He. In this case a correlation between age and U-Th contents (often expressed as effective uranium, eU= [U] + 0.235×[Th]) could be observed.

### 3.2.2. FISSION-TRACK THERMOCHRONOLOGY

Fission track thermochronology is based on the analysis of damage trails, namely the "fission tracks" (FT), producted by the spontaneous fission of U.

The spontaneous fission decay of 238U produces linear defects in the lattice of U-bearing minerals (Fleischer et al. 1975), which are enlarged using a chemical etching process enabling their observation under an optical microscope.

The technique is applied to minerals which contain sufficient U (typically >10 ppm) to generate a statistically useful quantity of spontaneous fission tracks over geological time. The method assumes that fission tracks are generated only by decay of $^{238}U$, which is generally true due to the low decay constant value of other isotopes decaying by spontaneous fission. Throughout this process, an unstable $^{238}U$ nucleus splits into two nuclear fragments positively charged. This ions travel to the lattice because of the coulomb repulsion forces between them.

The original ionization left by passage of charged particle is unstable and ejects ions into the solid; later the stressed region relaxes elastically, straining the undamaged matrix.

Typically, these fission tracks in apatite grains (AFT) have an initial width of approximately 10 nm and a length of up to 20 μm (Paul G Fitzgerald, 1992).

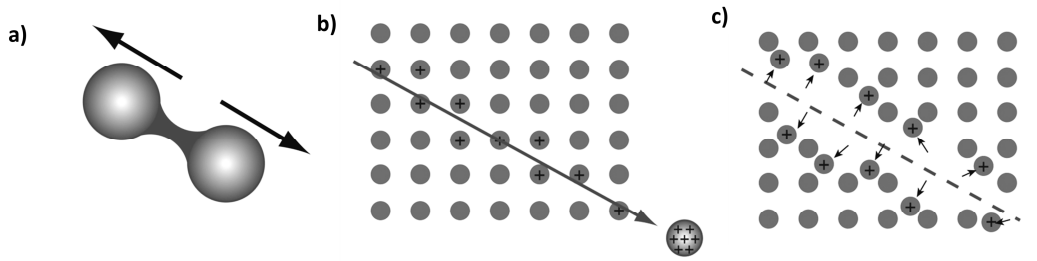


Fig. 3.3 The "Ion Explosion Spike" model for FT formation (from Fleischer et al., 1975). The Heavy nucleus splits in two nuclear fragments (a); the two positively charged fragments are pushed away from each other and along their track they tear off electrons from the atoms of the lattice (b); the positively charged atoms along the track dislocate from their lattice position due to repulsive electrostatic forces (c).

The determination of AFT age depends on the same general equation as any radioactive decay scheme, modified considering that 238U decays not only by spontaneous fission but also by α-decay (Tagami and O'Sullivan, 2005). A main difference is that AFT thermochronology measures the effect, rather than the product, of a radioactive decay scheme, referring to the number of 238U atoms and the number of spontaneous fission tracks per unit volume.:

$$N_s=\frac{\lambda_f}{\lambda_\alpha}{}^{238}N(e^{\lambda_\alpha t}-1)$$

where t is the time, $\lambda_f$ = 8.5 10-17 $yr^{-1}$ is the spontaneous fission decay constant, $\lambda_\alpha$=1.5 10-10 $yr^{-1}$ is the α-decay constant $\lambda_\alpha$=1.5 10-10 $yr^{-1}$, Ns is the number of spontaneous fission tracks per unit volume; $^{238}$N is the number of $^{238}$U atoms per unit volume.

This fission track density is obtained by counting the Ns on a polished internal surface of a mineral grain viewed under high magnification using an optical microscope.

#### 3.2.2.1. ANNEALING OF FT

Fission tracks are characterised by a semi-stable nature, therefore their dimension can change through time.

All newly formed tracks in apatite have a length of approximately 16 μm but they significantly shorten if during its history the sample experiences partial reset conditions. The shortening and fading of the fission tracks are controlled by their internal structure and chemistry, but generally the annealing can be considered as a temperature dependent diffusional process, to which the Arrhenius law can be applied. However, a defined physical model of fission track annealing at the atomic level. Fission tracks annealing models have thus been developed using a completely empirical approach (Braun et al., 2006).

The annealing rate also depends on the crystallographic orientation of the tracks and it is higher for tracks orthogonal to the C-axis of the crystal, lower for tracks parallel to it. In order to quantify the effect of annealing, the lengths of horizontal confined tracks are measured. The elements on which the analysis is based are mostly the tracks cut off by fractures (tracks in cleavage). The track lengths distribution obtained by this procedure provide information on the thermal history of the sample (Braun et al., 2006).

## 3.3 MODELLING WITH MOVE

The construction of balanced section has been performed using Move by Midland Valley, a software dedicated to the structural modelling, that allows to provide a validated geological scenario for the study area. The core features of this application are the processing of data coming from several sources and the integration between different types of information for 2D cross-section construction and 3D model building.

The algorithms on which the program is based assure the geometrical correctness of the geological cross-sections, adhering to structural geology principles and providing the essential tools to build, balance, restore and analyse cross-sections at a local and regional scale. For normal faulting the "simple shear" algorithm was applied, whereas for compressional faulting the "fault parallel flow" algorithm resulted more fitting. The former requires knowing the geometry of the hanging wall and describes well the movement of listric faults, the latter considers the motion of every element as parallel to the fault plane and is used to restore thrusts with flat-ramp geometry.

Although the modules allow both 2D and 3D analysis, only the two-dimensional model has been sought since sufficient for the goals of this work.

2D modelling assumes that the kinetic of the movements is parallel to the plain of section, otherwise the accuracy of the algorithms is not complete and the cross-section cannot be rightfully balanced and restored. This problem can be obviated placing the section in order to be orthogonal to the main direction of the structures in the area, like faults or fold axis.

The core of the structural modelling is the construction of a balanced section which can be sequentially restored from its deformed present-day geometry to the undeformed original shape.

Starting from outcrop and borehole data we construct a geological cross-section that has to be corrected in agreement with the result of the sequential restoration. Every change made during the restoration has to be applied to the present-day section. The final result is a balanced cross-section with geometries consistent with those observed in the field. The geometry of faults have to be reasonable and the bed-lengths and bed area must be conserved.

The algorithms applied to restore the displacement along the normal faults and the reverse faults are the vertical simple shear and the fault parallel flow, respectively. The isostatic response to the tectonic load and the removal of

sedimentary bodies has been simulated applying flexural isostasy and the appropriate decompaction curves, respectively. The parameters token into account for the isostatic correction will be described in the next chapter.

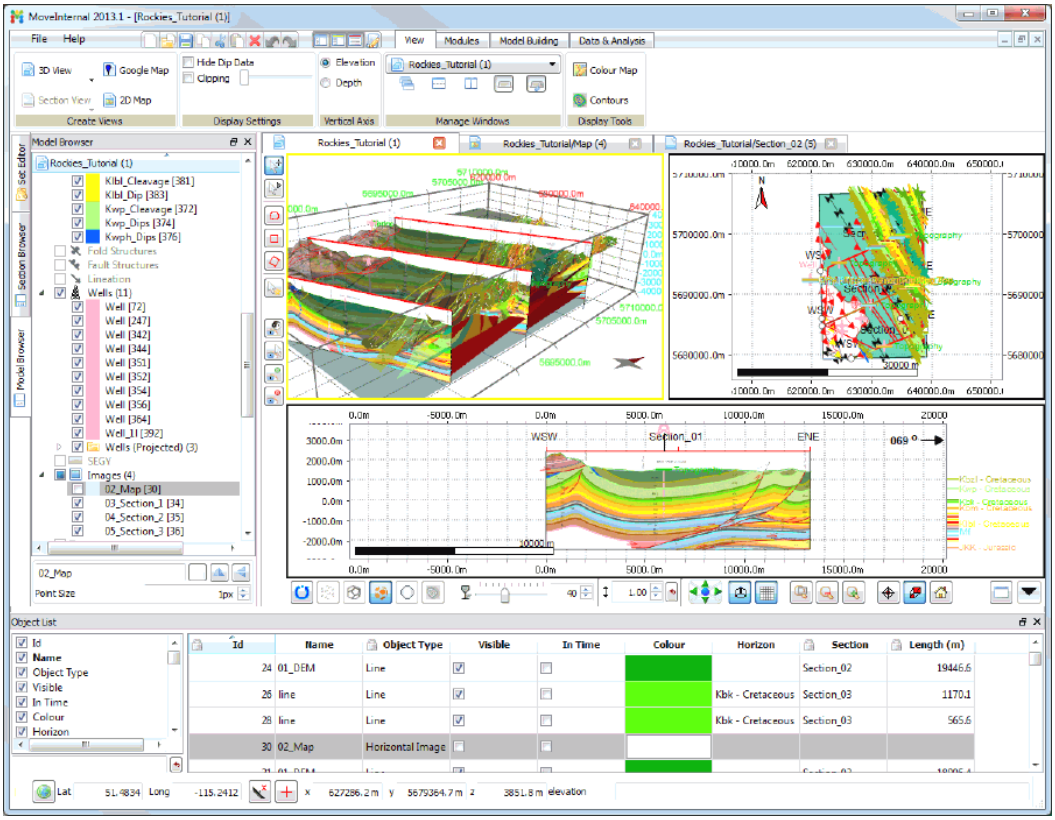


Fig. 3.3 Image from Move2013 tutorial, displaying the main features and modules of the software.

# CHAPTER FOUR

# SAMPLES AND PROCEDURES

The collection of the materials for thermochronology occurred during a geological survey in June 2013. The field trip covered the Ukrainian and Polish Carpathians, transiting in the meanwhile through the HCM. The field team was composed by both italian and polish geologists whose aim was to improve the knowledge of the structural geology, the thermochronology and the paleotemperatures of the area.

## 4.1. MATERIALS

A set of 12 samples was taken from different outcrops to analyse the apatite minerals with both (U-Th)/He and fission track analysis. In Figure 4.1 the location of the samples is shown.

Table 4.1

The table summarise the collected samples, their exact location and the lithology of which they belong.

| Samples | Latitude | Longitude | Elevation | Age |
|---|---|---|---|---|
| PL_105 | 50° 44' 46.06" | 21° 1' 46.77" | 0 | Silurian |
| PL_106 | 50° 56.721' | 21° 1.531' | 263 | Devonian |
| PL_107 | 50° 58' 39.6" | 21° 00' 46.3" | 258 | Silurian |
| PL_108 | 50.84327° | 21.68728° | 0 | Silurian |
| PL_109 | 50.905903° | 21.151512° | 0 | Triassic |
| PL_110 | 50°57.634' | 21° 11.689' | 205 | Triassic |
| PL_111 | 50° 58' 6.2" | 20° 34'37.3" | 0 | Triassic |
| PL_112 | 50.969156° | 20.691287° | 0 | Permo_Triassic |
| PL_113 | 50°58'2.6" | 21°13'23.0" | | |
| PL_114 | 50° 44' 08.9" | 21° 33' 48.1" | | |
| PL_115 | 50°50.233' | 20°44.099' | 0 | Silurian |
| PL_116 | 50° 25' 48.5" | 20° 48' 17.9" | 265 | Miocene |

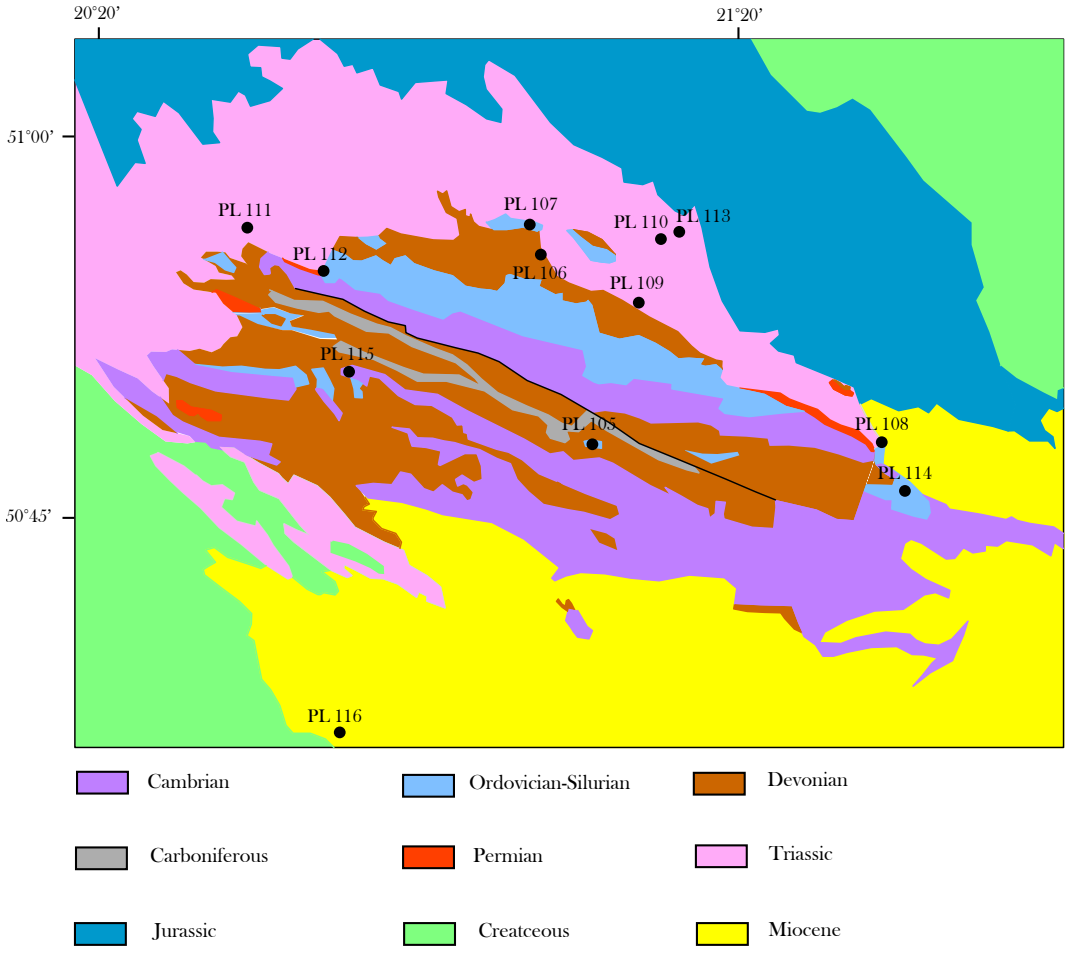


Fig 4.1 The map represents the stratigraphic units of the HCM, distincted by colour.The bolder black line marks the Holy Cross Fault, the other line identifies the chosen cross-section. The black circles show the location of the samples.

All the collected samples represent sandstones and limestones from the Łysogóry unit and the Kielce unit. In Table 4.1 the main geographical features of the samples are provided, along with their age estimated by the horizon from which the material was collected.

### 4.1.1. SAMPLES PREPARATION

All the samples were studied at the University of Padua, Department of Geosciences.

Rock cobbles aptly labelled were fragmented using first a press crusher, then a jaw crusher. Accurate cleaning procedures were applied in order to avoid the contamination of the samples. The crumbled material was sieved through 250 μm sieve-cloth achieving a uniform sand-like particle size; the coarser fraction was reworked until it reached the correct dimensions.

Part of the material was then inserted in a washing table with riffles, the other fraction was separated by decanting in bakers, in order to remove the fine grained material. The two different procedures were aimed to verify the efficiency of the two techniques in selecting the correct grain size. We found that although the table with ripples minimise the working time, its accuracy seems to be slightly minor.

The magnetic fraction was separated by processing the sand-classed material with a Frantz Isodynamic magnetic separator. The diamagnetic fraction was submitted to heavy liquid separation with Sodium Polytungstate, the density of which is shown in Figure 4.2, allowing the concentration of the minerals with a density higher than $\rho$=2.89 g/cm$^3$, that is both apatite ($\rho$=3.1-3.35 g/cm$^3$) and zircon ($\rho$= 4-4.70 g/cm$^3$). From this point forward the material was worked with distinct procedures depending of the analysis to employ on it.

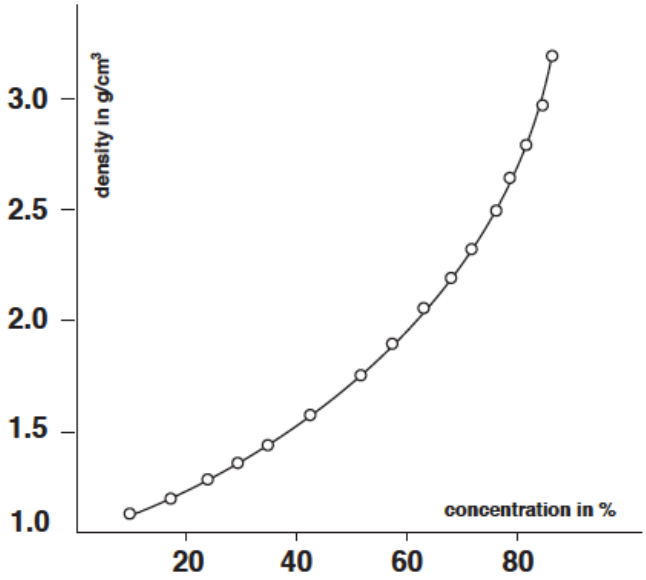


Fig 4.2 Density of aqueous sodium polytungstate solution as a function of mass portion at 25°C.

### 4.1.2. MAP SPECIFICATIONS AND ACQUISITION

The first step for the construction of a structural model is the acquisition of all available geological maps of the area.

For the regional view, which allows to detect the main structures, it was used the "Góry Świętokrzyskie" map on 1:200000 realised by Panstwowy Instytut Geologiczny. This map is the scansion of the master copy on paper, hence it possess only two-dimensional data. For this reason, along with its poor resolution, it is useful to give a general idea of the geological structure of the area from a qualitative point of view, but it can not be used for the modelling in the strict sense.

The data actually used for the modelling belongs to a set of 15 maps on 1:50000 scale acquired by the same institute, realised in .tiff format, hence providing elevation data and supplying tridimensional topography.

## 4.2. PROCEDURES

### 4.2.1. AHE

The selection of the material obtained after the separation process was performed by manual picking under optical stereoscope. The apatite grains were selected according to the characteristics previously stated in the paragraph about the (U-Th)/He thermochronology.

The apatites were photographed and measured for the geometrical reconstruction required for α-ejection correction. The prism length and width measurements were taken respectively parallel on the c-axis, and perpendicular to it on two orthogonal directions.

Then crystals were packed in Nb tubes of 1mm heights that worked as a micro-furnace for crystal heating and He extraction during analysis and then sent to the Geosciences department of the University of Arizona (Tucson).

The crystal is degassed by heating and 4He is measured by gas-source mass spectrometry. Apatite is chemically dissolved and U, Th and Sm contents are measured by inductively coupled plasma mass spectrometry.

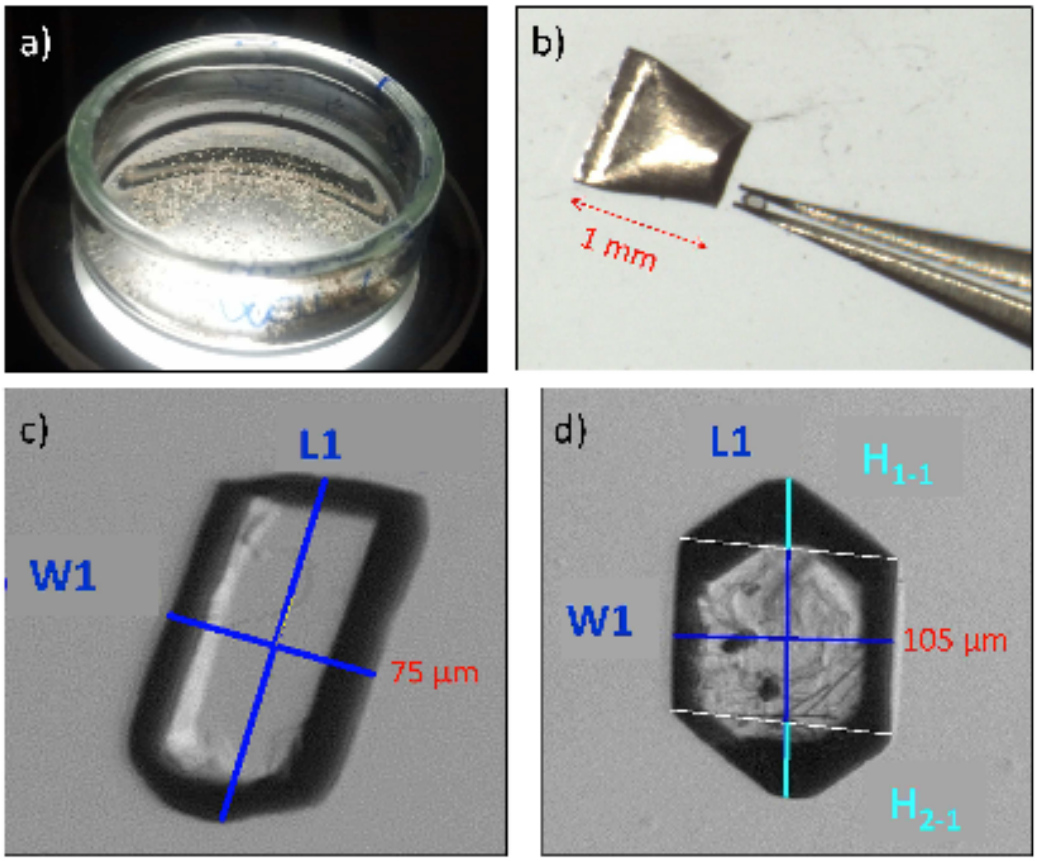


Fig 4.3 Grain selection and picking: the grains are poured in a petri-dish for grain selection under optical microscope (a); the selected grains are photographed and measured, for apatite length (L) and width (W) are measured on two sides parallel to the c-axis (c) , for zircons the tips heights (H1, H2) are also measured (d). Grains are finally packed in Nb tubes (b).

### 4.2.2. AFT

The remaining apatites which do not fit the criteria were employed in AFT analysis: apatite grains were mounted in epoxy resin, polished to expose inner crystal surfaces and to eliminate defects, then chemically etched with $HNO^3$ to highlight the spontaneous tracks .

Following the External Detector Method (EDM), a mica sheet with low-U content was placed over each grain mount and then piled in standard irradiation tubes. At the two ends of each stack of samples, two packages constituted by standard CN5 glass, of known U content, and mica were

placed in order to monitor neutron fluence during irradiation. Sample irradiation was performed in the reactor at the Radiation Centre of Oregon State University with a nominal neutron fluence of $9x10^{15}$ n $cm^{-2}$,. Nuclear fragments belonging to $^{235}U$ atoms placed close to the polished surfaces of the grains are injected in the mica sheet forming fission tracks in its lattice. Induced fission track density can be then measured on the mica surface after proper chemical etching. The $^{238}U$ content is then calculated according the constant natural $^{235}U/^{238}U$ ratio ($7.252x10^{-3}$).

After irradiation, each mount-mica package was opened and the mica sheets were chemically etched with HF 40% for 40 minutes in order to highlight the fission tracks induced by neutron irradiation. Apatite fission track analysis was performed trough an optical microscope on mount-mica couples fixed on microscope slides. For every samples, 20 apatites were selected, and analysed. Their spontaneous track density was measured along with the induced track density on their imprints on the mica.

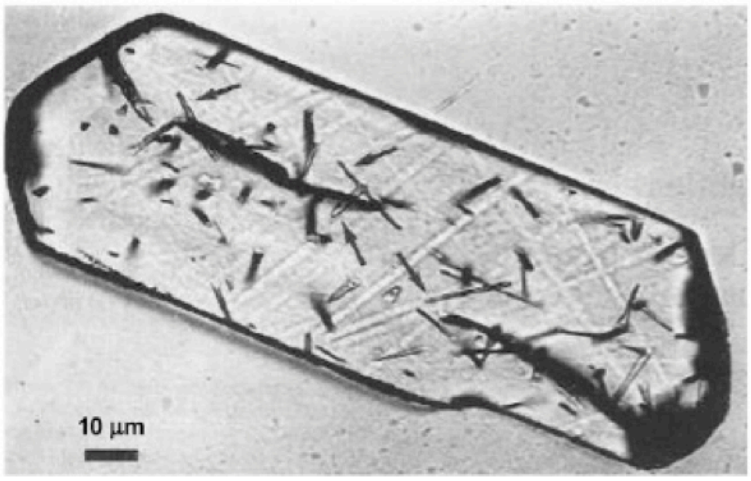


Fig 4.3 An optical microscopy image of etched spontaneous tracks on a polished internal surface of apatite crystal. (Gleadow et al., 1986)

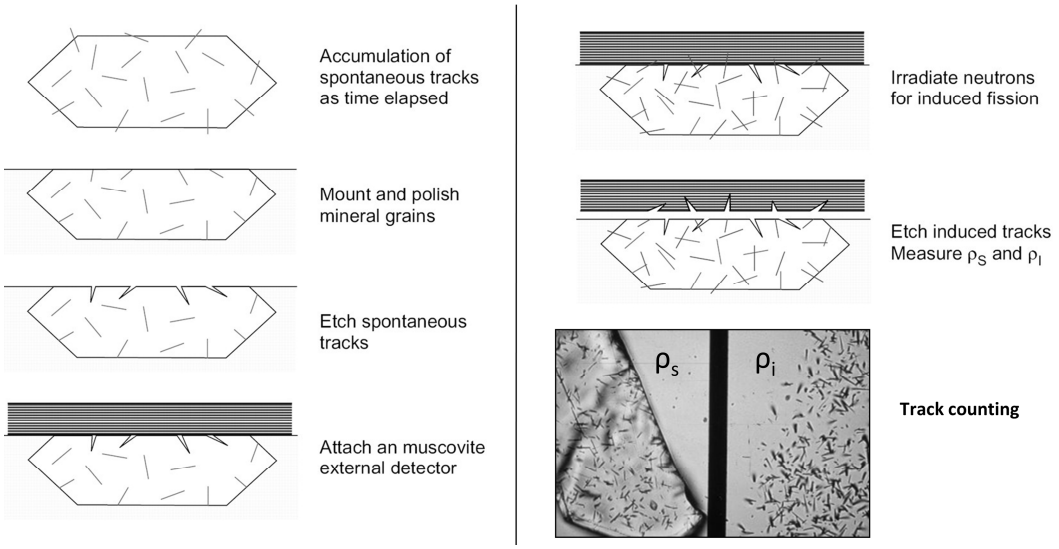


Fig 4.4 Schematic procedure for FT analysis with the EDM method (from Tagami and O'Sullivan, 2005). Source for the picture of spontaneous and induced tracks is the www.geotrack.com.au website.

Then their ages were determined using the equation:

$$t_i = \frac{1}{\lambda_d} ln\left(1 + \lambda_d \zeta g \rho_d \frac{\rho_{s,i}}{\rho_{i,i}}\right)$$

Where subscript i refers to grain i; ti is fission track age of grain i; $\lambda_d$ is the total decay constant of $^{238}U$; $\zeta$ is the calibration factor based on EDM of fission track age standards, depending on the microscope and operator; g is the geometry factor for spontaneous fission track registration, $\rho_d$ the induced fission track density for a uranium standard corresponding to the sample position during neutron irradiation, $\rho_s$, i is the spontaneous fission track density for grain i; $\rho_i$, i is the induced fission track density for the grain i (Donelick et al., 2005).

Measured data were input into a proper software, (TRACKKEY) , which allows to calculate the mean age, test the homogeneity of age populations and to generate radial plots of the ages for every analysed sample.

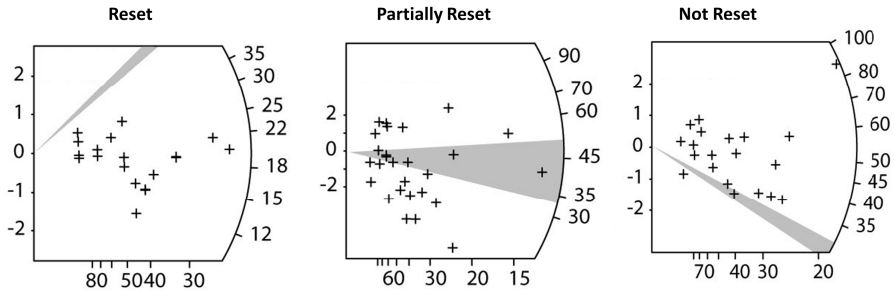


Fig 4.5 Examples of Radial Plots referred to sedimentary rocks heated to different degree.

### 4.2.3. CROSS-SECTION BUILDING AND FORWARD MODELLING

The first step to construct a geological cross-section with Move was to import the maps in the software. The tiff-format maps were conveniently cut and georeferenced using the Universal Transverse Mercator coordinate system (UTM) on the WGS84 reference ellipsoid. Then the section trace was drawn, placing it normal to the tectonic transport direction and to the regional structures, in order to maximise the accuracy of the restoration.

In this study, a NE-SW oriented section was chosen, going from Potok village (Staszów County), near Chmielnik town, to Lubienia (Starachowice County).

Subsequently, the top of every horizon and the fault traces were digitised on the maps and its intersection with the section trace was reported on the topographic profile. All the dips in close proximity to the section were digitised and then projected on that trace line. The odd data were manually adjusted to be located in the right structural and stratigraphic position.

Some geological profiles provided with the 1:50000 scale geological maps were acquired and digitised to obtain information on the orientation of the faults, otherwise obliterated by Miocene and Quaternary deposits. Well-data were used to constrain the thickness of strata at depth.

These procedures were essential in order to construct an initial raw section (Fig. 4.6), which would provide the basis for developing a general forward

model. The latter allows the construction of the eroded strata above the present-day topographic profile.

Fig 4.6 Raw model of the cross section. The eroded strata have been reconstructed assuming a constant thickness. Solid lines represent strata constrained by field evidence, point-dotted lines strata reconstructed hypothesising a certain thickness, dotted lines indicate particular geometry as folds.

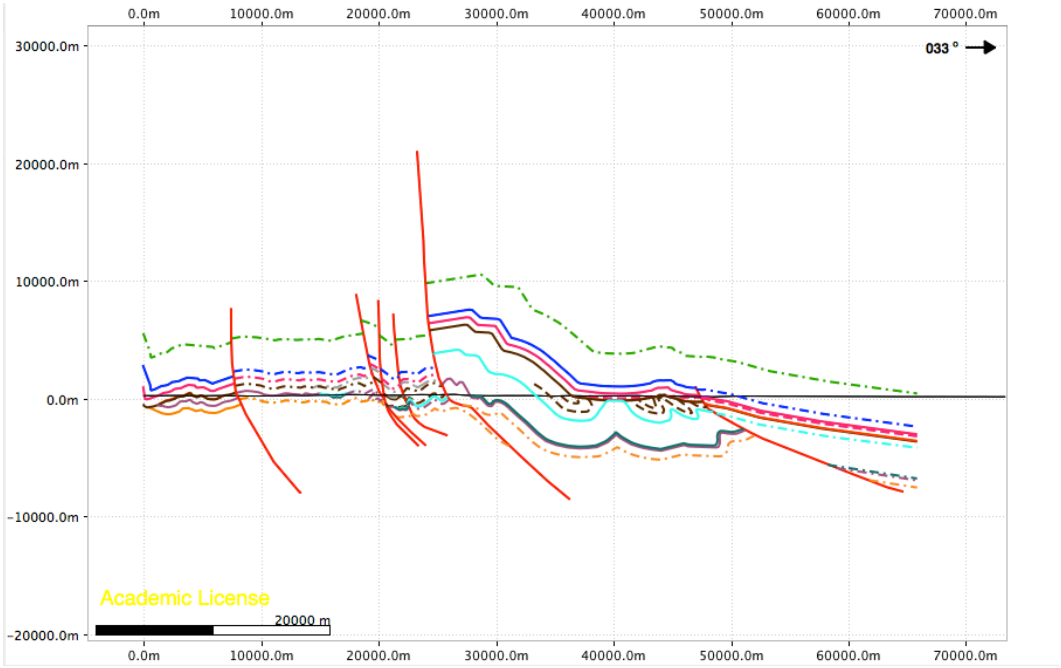


Forward modelling means the application of deformations and movements on undeformed horizontal beds. Therefore, it reconstructs the tectonic history from the past to the present time. This model requires as input data the geometry of the faults and the thickness of the strata. It does not have to be detailed, but it has to provide a general idea of the structural evolution of the area, which can be deduced from the references.

The oldest horizon was supposed to be horizontal and undeformed, and the older faults were delineated. Then the deformation was applied, according to both geometrical (e.g. present-day relationships between strata) and geological evidences (e.g. folds, unconformities, erosional surfaces).

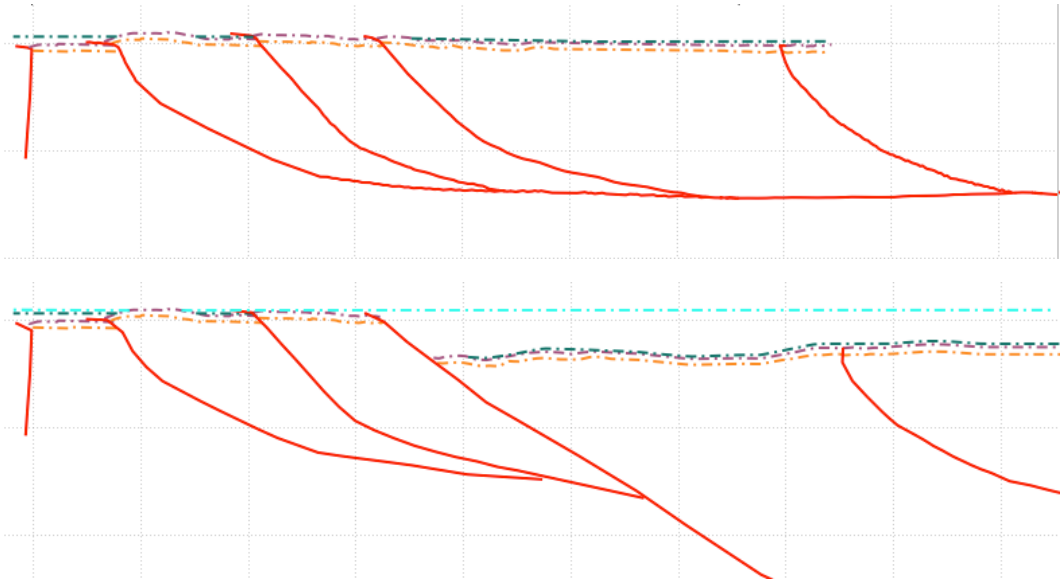

Fig 4.7 Simple shear deformation applied to reconstruct the extensional movement along a fault. The strata which fill the accommodation space is horizontal an undeformed.

The main deformations that were applied can be divided in fault-related (Fig 4.7) and non-fault-related. The former group includes the movements along the faults for which the algorithms described in Chapter 3 are applied.

Non-fault-related movements include deformations due to the compaction of the strata, and the isostasy. The algorithms used in this processes require information about physical values of beds, like their porosity, density, flexural elasticity etc.

Performing the forward model, the data are constantly corrected and the raw section was ongoing modified through iterations, so that the final output would be a cross-section which can be modified from the present time to the past without changes.

In this way, the balanced section is achieved, as shown in Fig 4.8.

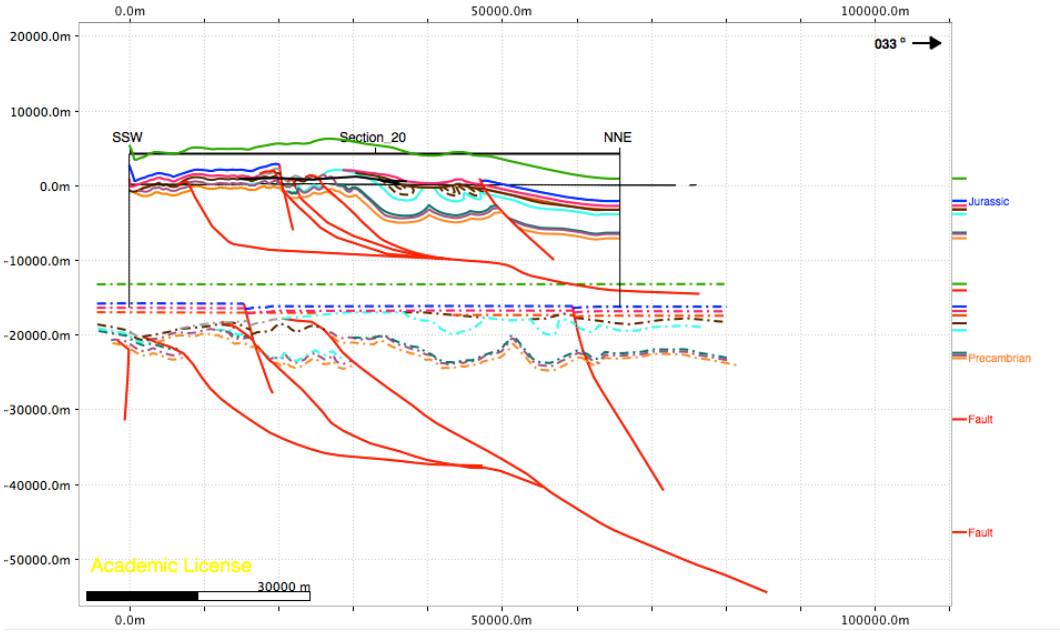


Fig 4.8 The first images represent the balanced section, achieved by forward modelling. The second image display the first step of unfolding in order to retrodeform the cross-section.

# CHAPTER FIVE

# RESULTS

In this chapter the results of the (U-Th)/He and the fission-track analysis are presented and briefly commented. The detailed interpretation and discussion will be provided in the following chapter.

The restored section and the restoring process are also displayed in detail.

## 5.1 AHE

Table 5.1

Apatite (U-Th)/He analytical data

Sample name; Th/U - ratio between the Th and U masses; raw date - grain age before applying the alpha ejection correction factor (FT); ± σ - analytical error on raw date; Correct date – grain age corrected by the HAC factor; ± σ – analytical error on corrected age. 4 replicates were excluded from the dataset and not taken in account. Criteria for discarding a crystal were: a) outlier age value accompanied by marked imperfections observed in the grain (bad shape, inclusions); b) outlier age value accompanied by extremely high or low analytical values; c) outlier age value with no apparent meaning (e.g. non reset age in crystal belonging to a sample with completely reset AFT age).

Table 5.2

Apatite (U-Th)/He analytical data (continuum)

Ppm eU- concentration of effective Uranium (eU=[U] + 0.235×[Th]); ppm U to nmol 4He - concentration of U, Th, Sm and He.

Table 5.3

Apatite (U-Th)/He analytical data (continuum)

Mass and concentrations related to the Ca content.

| SAMPLE NAME | Th/U | raw date (Ma) | 1s ± date (Ma) | 1s ± date % | Ft 238U | Ft 235U | Ft 232Th | Ft 147Sm | Rs (um) | corr date (Ma) | 1s ± date (Ma) | 1s ± date % |
|---|---|---|---|---|---|---|---|---|---|---|---|---|
| PL105_Ap1 | 2.37 | 65.77 | 1.20 | 1.83 | 0.79 | 0.76 | 0.76 | 0.93 | 67.75 | 84.51 | 1.55 | 1.83 |
| PL105_Ap2 | 2.06 | 107.87 | 1.94 | 1.80 | 0.84 | 0.81 | 0.81 | 0.95 | 90.62 | 129.60 | 2.34 | 1.81 |
| PL105_Ap3 | 1.45 | 52.06 | 1.77 | 3.40 | 0.75 | 0.71 | 0.71 | 0.92 | 56.40 | 70.37 | 2.41 | 3.43 |
| PL105_Ap4 | 2.73 | 204.80 | 5.71 | 2.79 | 0.83 | 0.81 | 0.81 | 0.95 | 87.23 | 248.08 | 6.98 | 2.81 |
| PL105_Ap5 | 3.77 | 41.10 | 0.77 | 1.88 | 0.75 | 0.71 | 0.71 | 0.92 | 56.67 | 56.05 | 1.06 | 1.88 |
| PL107_Ap1 | 25.32 | 24.80 | 0.60 | 2.43 | 0.73 | 0.70 | 0.70 | 0.91 | 53.75 | 35.20 | 0.86 | 2.43 |
| PL107_Ap2 | 4.98 | 92.47 | 2.14 | 2.32 | 0.66 | 0.61 | 0.61 | 0.89 | 40.34 | 145.77 | 3.40 | 2.34 |
| PL107_Ap3 | 2.79 | 35.64 | 14.24 | 39.94 | 0.68 | 0.63 | 0.63 | 0.90 | 43.36 | 53.90 | 22.11 | 41.02 |
| PL107_Ap4 | 14.71 | 60.71 | 1.14 | 1.88 | 0.73 | 0.69 | 0.69 | 0.91 | 52.55 | 86.29 | 1.62 | 1.88 |
| ~~PL107_Ap5~~ | ~~8.52~~ | ~~0.19~~ | ~~0.45~~ | ~~240.41~~ | ~~0.70~~ | ~~0.66~~ | ~~0.66~~ | ~~0.90~~ | ~~47.76~~ | ~~0.28~~ | ~~0.67~~ | ~~240.39~~ |
| PL108_Ap1 | 0.62 | 122.26 | 2.56 | 2.09 | 0.63 | 0.59 | 0.59 | 0.88 | 37.49 | 193.29 | 4.08 | 2.11 |
| PL108_Ap2 | 4.22 | 128.26 | 6.08 | 4.74 | 0.72 | 0.68 | 0.68 | 0.91 | 50.41 | 182.48 | 8.87 | 4.86 |
| PL108_Ap3 | 5.71 | 69.71 | 1.12 | 1.61 | 0.75 | 0.72 | 0.72 | 0.92 | 57.33 | 95.24 | 1.54 | 1.61 |
| PL108_Ap4 | 4.30 | 121.21 | 1.80 | 1.48 | 0.79 | 0.76 | 0.76 | 0.93 | 67.48 | 156.85 | 2.33 | 1.48 |
| PL108_Ap5 | 2.86 | 105.84 | 2.43 | 2.30 | 0.69 | 0.64 | 0.64 | 0.90 | 44.59 | 157.65 | 3.65 | 2.32 |
| PL109_Ap1 | 4.41 | 33.01 | 0.92 | 2.77 | 0.59 | 0.54 | 0.54 | 0.86 | 33.17 | 58.06 | 1.61 | 2.78 |
| PL109_Ap2 | 18.78 | 97.84 | 2.13 | 2.18 | 0.72 | 0.68 | 0.68 | 0.91 | 50.02 | 141.97 | 3.09 | 2.18 |
| ~~PL109_Ap3~~ | ~~12.19~~ | ~~20.22~~ | ~~1.16~~ | ~~5.74~~ | ~~0.70~~ | ~~0.66~~ | ~~0.66~~ | ~~0.90~~ | ~~46.49~~ | ~~30.26~~ | ~~1.74~~ | ~~5.75~~ |
| PL109_Ap4 | 6.72 | 41.11 | 0.84 | 2.04 | 0.75 | 0.71 | 0.71 | 0.92 | 57.06 | 56.38 | 1.15 | 2.04 |
| PL109_Ap5 | 3.09 | 59.59 | 0.97 | 1.63 | 0.82 | 0.80 | 0.80 | 0.94 | 83.64 | 73.12 | 1.19 | 1.63 |
| PL110_Ap1 | 12.69 | 39.93 | 0.67 | 1.68 | 0.74 | 0.70 | 0.70 | 0.92 | 54.49 | 56.06 | 0.94 | 1.67 |
| PL110_Ap2 | 13.62 | 34.01 | 0.65 | 1.92 | 0.65 | 0.60 | 0.60 | 0.89 | 39.45 | 55.16 | 1.06 | 1.92 |
| PL110_Ap3 | 5.92 | 40.26 | 0.69 | 1.71 | 0.75 | 0.72 | 0.72 | 0.92 | 57.44 | 55.04 | 0.94 | 1.71 |
| PL110_Ap4 | 12.02 | 37.24 | 0.67 | 1.79 | 0.75 | 0.71 | 0.71 | 0.92 | 56.96 | 51.45 | 0.92 | 1.78 |
| PL110_Ap5 | 14.01 | 34.67 | 0.72 | 2.07 | 0.71 | 0.67 | 0.67 | 0.91 | 49.30 | 50.70 | 1.05 | 2.07 |
| PL112_Ap1 | 1.89 | 59.32 | 1.06 | 1.79 | 0.83 | 0.81 | 0.81 | 0.95 | 87.93 | 71.79 | 1.29 | 1.80 |
| PL112_Ap2 | 4.23 | 50.26 | 0.89 | 1.78 | 0.81 | 0.79 | 0.79 | 0.94 | 77.76 | 62.86 | 1.12 | 1.78 |
| PL112_Ap3 | 16.52 | 45.85 | 0.88 | 1.92 | 0.82 | 0.79 | 0.79 | 0.94 | 79.33 | 57.62 | 1.11 | 1.92 |
| PL112_Ap4 | 0.23 | 78.85 | 1.52 | 1.93 | 0.86 | 0.84 | 0.84 | 0.95 | 103.47 | 92.08 | 1.78 | 1.93 |
| PL112_Ap5 | 4.58 | 52.81 | 0.94 | 1.78 | 0.79 | 0.76 | 0.76 | 0.93 | 68.88 | 68.13 | 1.21 | 1.78 |

| SAMPLE NAME | ppm eU (morph) | ppm eU w/ Sm (morph) | ppm U (morph) | d ppm U (morph) | ppm Th (morph) | d ppm Th (morph) | ppm Sm (morph) | d ppm Sm (morph) | nmol 4He/g (morph) | d nmol 4He/g (morph) | mol Ca | d mol Ca |
|---|---|---|---|---|---|---|---|---|---|---|---|---|
| PL105_Ap1 | 12.43 | 13.15 | 8.05 | 0.12 | 18.64 | 0.27 | 155.97 | 2.33 | 4.51 | 0.07 | 3.29E-08 | 5.66E-10 |
| PL105_Ap2 | 5.94 | 6.21 | 4.03 | 0.06 | 8.09 | 0.12 | 60.41 | 0.91 | 3.53 | 0.05 | 4.99E-08 | 8.95E-10 |
| PL105_Ap3 | 10.86 | 11.37 | 8.14 | 0.34 | 11.55 | 0.17 | 112.00 | 1.64 | 3.10 | 0.05 | 2.11E-08 | 3.88E-10 |
| PL105_Ap4 | 8.01 | 8.34 | 4.93 | 0.19 | 13.12 | 0.19 | 71.63 | 1.07 | 9.09 | 0.13 | 5.57E-08 | 9.66E-10 |
| PL105_Ap5 | 13.10 | 13.62 | 7.03 | 0.11 | 25.83 | 0.37 | 115.97 | 1.71 | 2.95 | 0.05 | 1.75E-08 | 2.97E-10 |
| PL107_Ap1 | 13.47 | 13.57 | 1.98 | 0.03 | 48.90 | 0.71 | 30.62 | 0.53 | 1.82 | 0.04 | 9.94E-09 | 2.31E-10 |
| PL107_Ap2 | 8.24 | 8.39 | 3.85 | 0.10 | 18.68 | 0.30 | 36.94 | 0.55 | 4.17 | 0.07 | 6.93E-09 | 1.26E-10 |
| PL107_Ap3 | 14.78 | 14.92 | 9.02 | 6.16 | 24.53 | 0.36 | 36.06 | 0.61 | 2.86 | 0.05 | 7.80E-09 | 1.33E-10 |
| PL107_Ap4 | 5.43 | 5.65 | 1.24 | 0.02 | 17.83 | 0.26 | 50.63 | 0.76 | 1.82 | 0.03 | 1.33E-08 | 2.35E-10 |
| ~~PL107_Ap5~~ | ~~1.56~~ | ~~1.56~~ | ~~0.53~~ | ~~0.02~~ | ~~4.39~~ | ~~1.14~~ | ~~0.07~~ | ~~0.06~~ | ~~0.00~~ | ~~0.00~~ | ~~0.00E+00~~ | ~~1.43E-11~~ |
| PL108_Ap1 | 8.98 | 9.45 | 7.86 | 0.13 | 4.76 | 0.10 | 102.45 | 1.52 | 6.06 | 0.10 | 3.02E-09 | 5.29E-11 |
| PL108_Ap2 | 7.32 | 7.48 | 3.72 | 0.34 | 15.30 | 0.23 | 37.53 | 0.61 | 5.15 | 0.07 | 1.57E-08 | 2.67E-10 |
| PL108_Ap3 | 9.94 | 10.09 | 4.31 | 0.07 | 23.96 | 0.34 | 36.75 | 0.54 | 3.78 | 0.05 | 2.08E-08 | 3.63E-10 |
| PL108_Ap4 | 7.06 | 7.25 | 3.56 | 0.05 | 14.89 | 0.22 | 45.39 | 0.68 | 4.70 | 0.05 | 2.98E-08 | 5.11E-10 |
| PL108_Ap5 | 8.67 | 8.81 | 5.24 | 0.11 | 14.59 | 0.24 | 33.36 | 0.52 | 5.02 | 0.09 | 7.33E-09 | 1.36E-10 |
| PL109_Ap1 | 18.71 | 19.47 | 9.31 | 0.14 | 40.02 | 0.57 | 169.71 | 2.60 | 3.39 | 0.09 | 6.65E-09 | 1.26E-10 |
| PL109_Ap2 | 10.42 | 10.87 | 1.96 | 0.03 | 35.96 | 0.52 | 103.88 | 1.51 | 5.62 | 0.10 | 1.38E-08 | 2.41E-10 |
| ~~PL109_Ap3~~ | ~~2.98~~ | ~~3.01~~ | ~~0.79~~ | ~~0.03~~ | ~~9.34~~ | ~~0.14~~ | ~~8.64~~ | ~~0.14~~ | ~~0.33~~ | ~~0.02~~ | ~~8.52E-09~~ | ~~1.68E-10~~ |
| PL109_Ap4 | 7.18 | 7.30 | 2.83 | 0.04 | 18.53 | 0.27 | 29.17 | 0.43 | 1.61 | 0.03 | 1.68E-08 | 2.95E-10 |
| PL109_Ap5 | 22.23 | 22.46 | 13.01 | 0.19 | 39.23 | 0.57 | 57.36 | 0.87 | 7.22 | 0.09 | 5.35E-08 | 9.40E-10 |
| PL110_Ap1 | 14.47 | 14.59 | 3.70 | 0.06 | 45.82 | 0.66 | 34.30 | 0.54 | 3.15 | 0.04 | 1.48E-08 | 2.97E-10 |
| PL110_Ap2 | 35.65 | 36.55 | 8.65 | 0.13 | 114.87 | 1.65 | 215.98 | 3.19 | 6.64 | 0.10 | 1.02E-08 | 1.85E-10 |
| PL110_Ap3 | 24.17 | 24.48 | 10.26 | 0.15 | 59.20 | 0.85 | 79.54 | 1.18 | 5.30 | 0.07 | 1.97E-08 | 4.34E-10 |
| PL110_Ap4 | 21.00 | 21.14 | 5.59 | 0.08 | 65.54 | 0.94 | 44.53 | 0.68 | 4.26 | 0.06 | 1.90E-08 | 3.51E-10 |
| PL110_Ap5 | 25.95 | 26.05 | 6.17 | 0.10 | 84.19 | 1.32 | 38.16 | 0.65 | 4.90 | 0.08 | 1.52E-08 | 2.63E-10 |
| PL112_Ap1 | 10.29 | 10.49 | 7.18 | 0.10 | 13.24 | 0.19 | 44.09 | 0.66 | 3.33 | 0.05 | 7.79E-08 | 1.38E-09 |
| PL112_Ap2 | 14.04 | 14.16 | 7.13 | 0.10 | 29.40 | 0.42 | 30.24 | 0.44 | 3.84 | 0.06 | 3.46E-08 | 5.86E-10 |
| PL112_Ap3 | 8.80 | 8.89 | 1.84 | 0.03 | 29.62 | 0.42 | 25.74 | 0.38 | 2.20 | 0.03 | 4.39E-08 | 7.82E-10 |
| PL112_Ap4 | 52.21 | 52.45 | 49.64 | 0.71 | 10.95 | 0.16 | 51.56 | 0.75 | 22.37 | 0.31 | 1.13E-07 | 2.02E-09 |
| PL112_Ap5 | 12.02 | 12.20 | 5.86 | 0.08 | 26.19 | 0.37 | 43.32 | 0.64 | 3.46 | 0.05 | 3.36E-08 | 5.83E-10 |

| SAMPLE NAME | mass ap (g) | d mass ap (g) | ppm U (Ca) | d ppm U (Ca) | ppm Th (Ca) | d ppm Th (Ca) | ppm Sm (Ca) | d ppm Sm (Ca) | nmol 4He/g (Ca) | d nmol 4He/g (Ca) | ppm eU (Ca) | ppm eU w/ Sm (Ca) | eU (morph)/ eU (Ca) |
|---|---|---|---|---|---|---|---|---|---|---|---|---|---|
| PL105_Ap1 | 3.32E-06 | 5.71E-08 | 11.81 | 0.26 | 27.34 | 0.61 | 228.80 | 5.21 | 6.61 | 0.15 | 18.24 | 19.28 | 0.68 |
| PL105_Ap2 | 5.03E-06 | 9.03E-08 | 12.92 | 0.30 | 25.92 | 0.60 | 193.47 | 4.53 | 11.30 | 0.26 | 19.01 | 19.89 | 0.31 |
| PL105_Ap3 | 2.13E-06 | 3.92E-08 | 14.88 | 0.67 | 21.10 | 0.50 | 204.65 | 4.82 | 5.67 | 0.14 | 19.84 | 20.78 | 0.55 |
| PL105_Ap4 | 5.62E-06 | 9.74E-08 | 12.61 | 0.54 | 33.53 | 0.75 | 183.14 | 4.18 | 23.25 | 0.52 | 20.49 | 21.32 | 0.39 |
| PL105_Ap5 | 1.76E-06 | 2.99E-08 | 11.34 | 0.26 | 41.67 | 0.93 | 187.09 | 4.21 | 4.76 | 0.11 | 21.13 | 21.97 | 0.62 |
| PL107_Ap1 | 1.00E-06 | 2.33E-08 | 4.84 | 0.13 | 119.38 | 3.27 | 74.74 | 2.16 | 4.45 | 0.14 | 32.89 | 33.12 | 0.41 |
| PL107_Ap2 | 6.99E-07 | 1.27E-08 | 7.83 | 0.25 | 38.02 | 0.92 | 75.18 | 1.77 | 8.49 | 0.22 | 16.76 | 17.08 | 0.49 |
| PL107_Ap3 | 7.86E-07 | 1.34E-08 | 20.24 | 13.84 | 55.07 | 1.24 | 80.97 | 1.94 | 6.43 | 0.15 | 33.18 | 33.51 | 0.45 |
| PL107_Ap4 | 1.34E-06 | 2.37E-08 | 2.91 | 0.07 | 41.75 | 0.95 | 118.56 | 2.76 | 4.25 | 0.10 | 12.72 | 13.24 | 0.43 |
| ~~PL107_Ap5~~ | ~~n.d.~~ | ~~n.d~~ | ~~n.d~~ | ~~n.d~~ | ~~n.d~~ | ~~n.d~~ | ~~n.d~~ | ~~n.d~~ | ~~n.d~~ | ~~n.d~~ | ~~n.d~~ | ~~n.d~~ | ~~n.d~~ |
| PL108_Ap1 | 3.05E-07 | 5.33E-09 | 20.93 | 0.50 | 12.69 | 0.34 | 272.88 | 6.26 | 16.15 | 0.38 | 23.91 | 25.18 | 0.38 |
| PL108_Ap2 | 1.58E-06 | 2.70E-08 | 6.52 | 0.61 | 26.83 | 0.61 | 65.81 | 1.56 | 9.03 | 0.19 | 12.83 | 13.11 | 0.57 |
| PL108_Ap3 | 2.09E-06 | 3.66E-08 | 8.38 | 0.20 | 46.62 | 1.05 | 71.50 | 1.63 | 7.36 | 0.16 | 19.33 | 19.62 | 0.51 |
| PL108_Ap4 | 3.01E-06 | 5.15E-08 | 5.83 | 0.13 | 24.42 | 0.55 | 74.41 | 1.69 | 7.70 | 0.16 | 11.57 | 11.89 | 0.61 |
| PL108_Ap5 | 7.40E-07 | 1.37E-08 | 9.97 | 0.28 | 27.76 | 0.69 | 63.46 | 1.54 | 9.55 | 0.25 | 16.49 | 16.76 | 0.53 |
| PL109_Ap1 | 6.71E-07 | 1.27E-08 | 10.93 | 0.26 | 47.01 | 1.12 | 199.33 | 4.85 | 3.98 | 0.13 | 21.98 | 22.87 | 0.85 |
| PL109_Ap2 | 1.39E-06 | 2.43E-08 | 3.84 | 0.09 | 70.38 | 1.59 | 203.30 | 4.62 | 11.00 | 0.28 | 20.38 | 21.27 | 0.51 |
| ~~PL109_Ap3~~ | ~~8.59E-07~~ | ~~1.70E-08~~ | ~~2.01~~ | ~~0.08~~ | ~~23.89~~ | ~~0.59~~ | ~~22.11~~ | ~~0.56~~ | ~~0.84~~ | ~~0.05~~ | ~~7.63~~ | ~~7.71~~ | ~~0.39~~ |
| PL109_Ap4 | 1.70E-06 | 2.97E-08 | 6.73 | 0.16 | 44.07 | 1.01 | 69.39 | 1.59 | 3.83 | 0.10 | 17.09 | 17.37 | 0.42 |
| PL109_Ap5 | 5.39E-06 | 9.49E-08 | 30.61 | 0.70 | 92.28 | 2.10 | 134.92 | 3.13 | 16.97 | 0.37 | 52.29 | 52.83 | 0.43 |
| PL110_Ap1 | 1.49E-06 | 2.99E-08 | 8.69 | 0.22 | 107.52 | 2.65 | 80.48 | 2.05 | 7.39 | 0.18 | 33.96 | 34.23 | 0.43 |
| PL110_Ap2 | 1.03E-06 | 1.86E-08 | 11.18 | 0.26 | 148.41 | 3.42 | 279.04 | 6.50 | 8.58 | 0.21 | 46.05 | 47.22 | 0.77 |
| PL110_Ap3 | 1.99E-06 | 4.37E-08 | 15.73 | 0.42 | 90.79 | 2.39 | 122.00 | 3.24 | 8.14 | 0.21 | 37.07 | 37.55 | 0.65 |
| PL110_Ap4 | 1.91E-06 | 3.54E-08 | 11.69 | 0.28 | 136.93 | 3.20 | 93.03 | 2.23 | 8.90 | 0.21 | 43.87 | 44.17 | 0.48 |
| PL110_Ap5 | 1.53E-06 | 2.66E-08 | 7.59 | 0.18 | 103.58 | 2.42 | 46.95 | 1.14 | 6.03 | 0.15 | 31.93 | 32.04 | 0.81 |
| PL112_Ap1 | 7.85E-06 | 1.40E-07 | 13.44 | 0.31 | 24.79 | 0.56 | 82.53 | 1.92 | 6.23 | 0.14 | 19.26 | 19.63 | 0.53 |
| PL112_Ap2 | 3.49E-06 | 5.91E-08 | 15.13 | 0.34 | 62.36 | 1.38 | 64.14 | 1.44 | 8.15 | 0.18 | 29.78 | 30.02 | 0.47 |
| PL112_Ap3 | 4.43E-06 | 7.89E-08 | 4.48 | 0.10 | 72.23 | 1.65 | 62.76 | 1.46 | 5.37 | 0.13 | 21.46 | 21.68 | 0.41 |
| PL112_Ap4 | 1.14E-05 | 2.04E-07 | 104.61 | 2.39 | 23.08 | 0.53 | 108.65 | 2.51 | 47.13 | 1.07 | 110.04 | 110.52 | 0.47 |
| PL112_Ap5 | 3.39E-06 | 5.88E-08 | 12.29 | 0.28 | 54.90 | 1.23 | 90.82 | 2.07 | 7.26 | 0.17 | 25.19 | 25.57 | 0.48 |

Among the 12 initial samples, 5 were devoid of fitting apatites and 1 owned a unique apatite crystal, moreover not reliable for the analysis due to the marked roundness and the slightly small dimensions.

For each of the 6 remaining samples, 5 (prismatic, unfractured, not-coated, inclusion-free) apatite crystals were selected for the dating.

The crystals were often quite abraded and slightly-to-moderately rounded, but coating was generally minimal and a discrete part of the replicates was free of inclusions.

After the analysis, between the initial 30 replicates 4 were discharged because of their critical analytical values, mostly very low quantities of effective Uranium (eU) and Uranium, respectively.

The Th/U ratio presents moderately high values among the majority of replicates within the samples PL107, PL109, PL110, but abnormally high values are also present. This can be related to the presence of Th-bearing inclusions, however, the absence of a straightforward correlation between dates and the Th/U ratio (Table 5.1) indicates negligible influence of such Th rich inclusions.The raw date is the thermochronologic age calculated by the $^{4}He$ ingrowth equation with iterative processes, not corrected for the α-ejection. The computation of the raw date is based on the quantities of $^{238}U$, $^{235}U$, $^{232}Th$ and, $^{147}Sm$ in the grain. These values are expressed in ppm. Next to each value, the analytical error on the measure is indicated (d).

The quantities of $^{4}He$ and their analytical errors are indicated in nmol/g.

An age correction is thus applied according a geometrical factor (FT), based on the three measured dimensions of the grain, , and the $R_s$ parameter, that

explicits the spherical radius, that is the radius of a sphere with an equivalent surface area to volume ratio as the apatite crystal.
The raw data thus corrected express the real thermochronologic age of the crystal, for which, likewise the raw data, its analytical error (σ), absolute and percent, is given.
The concentration of effective Uranium (eU) is defined as:

$$eU=(U) + 0.235\times(Th)$$

Generally, low values of eU make the age not reliable.
The samples employed in this work are characterised by moderately to slightly low values, and most data are reliable.

The complete dataset is displayed in Table 5.1-5.2-5.3.

PL105 exhibits one bad data; the ages are different from each other, with a range of over 70 Ma. The reproducibility is very low.
PL107 shows one bad data and an array of ages characterised by a difference of over 100 Ma. Hence, the reproducibility is very low.
PL108 displays a good reproducibility, and the dates are around 155 Ma.
PL109 presents one bad data; the ages are different from each other, with a range of over 80 Ma. Two replicates have a good reproducibility, otherwise very low.
PL110 shows a distinctive reproducibility of ages, set around 55 Ma.
PL112 exhibit one bad data; the reproducibility is good and the dates are around 70 Ma.
Dispersion of the ages is showed in Fig. 5.1.

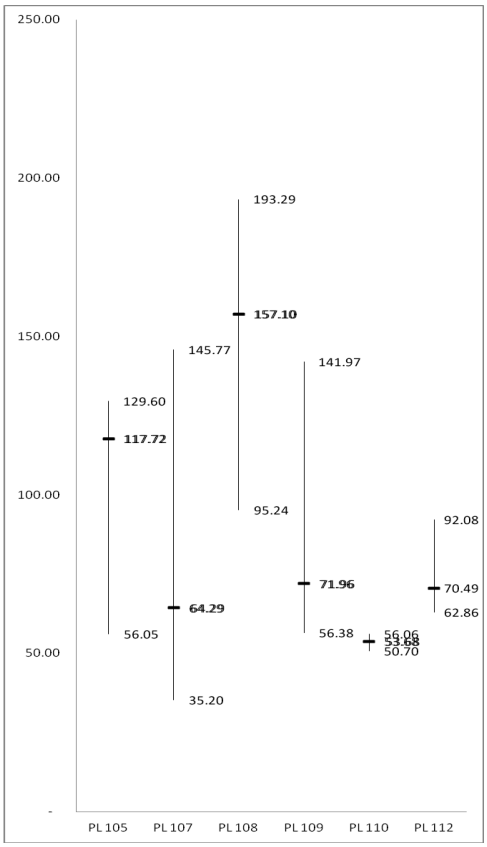


Fig 5.1 Data dispersion for every sample. On Y axis the thermochronological ages are plotted. The graph displays the maximum value, the minimum value, the ages range and (bolder) the mean of the values.

In the following graphics the correct ages and their relative errors are displayed.

Fig 5.2- 5.3 AHe data with 1σ error are plotted for every replicate in the upper figures.
In the lower graphics AHe data with 1σ error are plotted for every replicated according to the samples to which they belong, to improve the visibility.

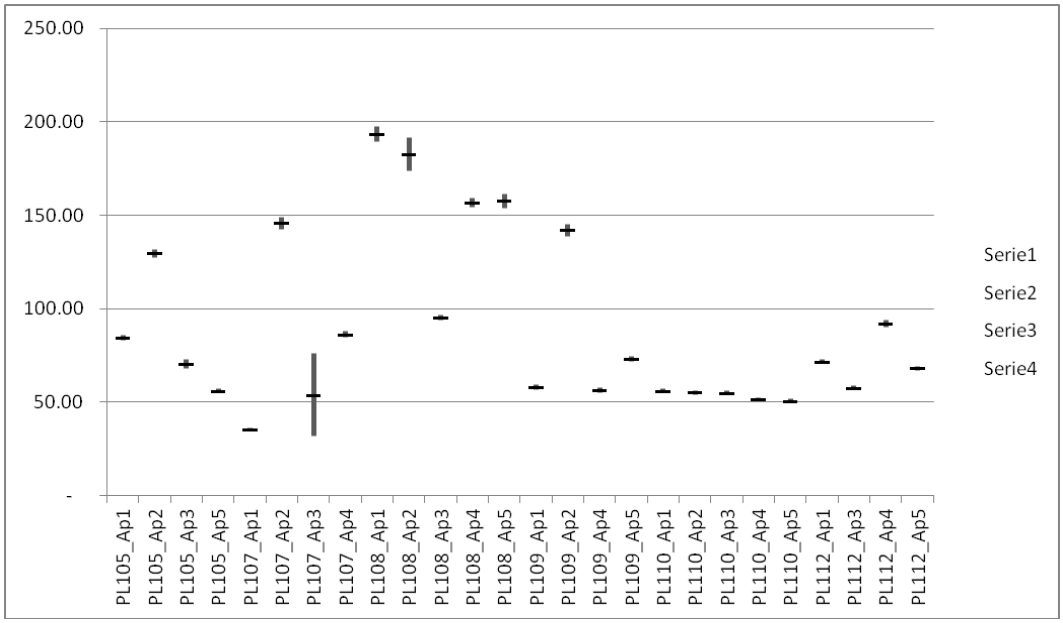


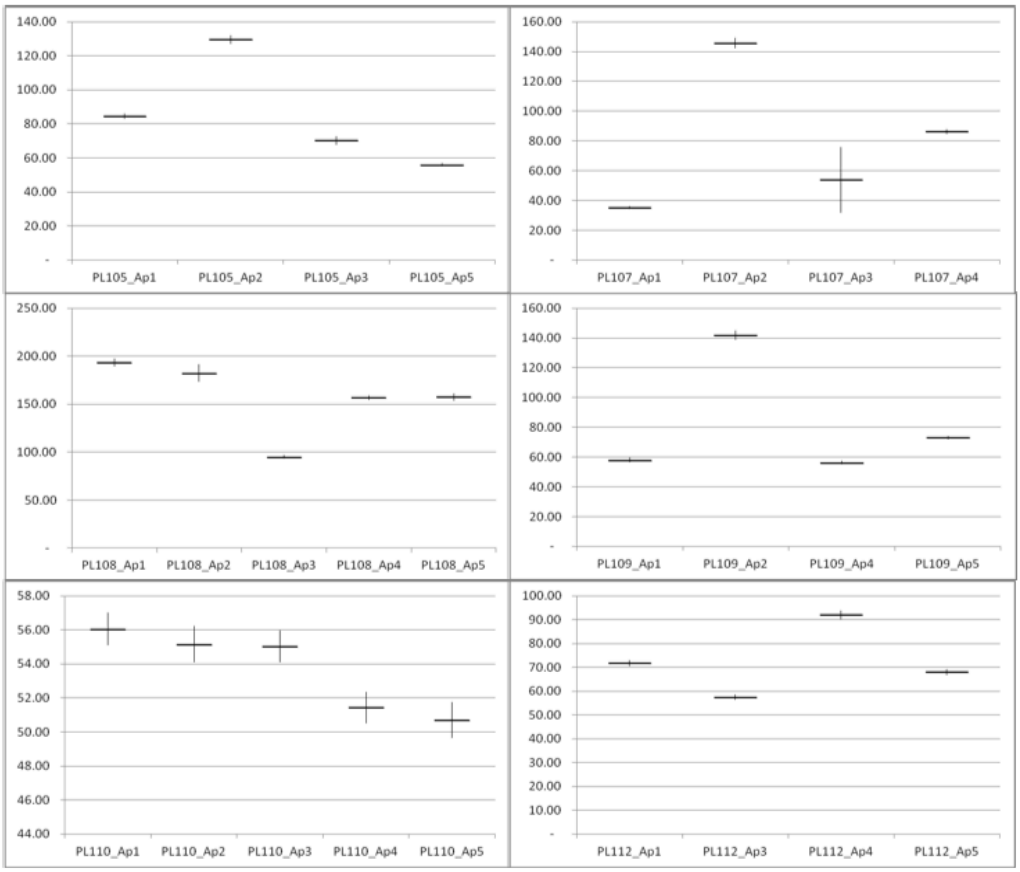


U-Th/He dating is based on the assumption that the $^{4}He$ ingrowth depends only of the age of closure of the system. Therefore, the age should not depend by the chemistry of the apatite crystal.

In order to verify this assumption, some graphics can be plotted, in order to check the relationships among age, and, U content, Th content, Th/U ratio and eU content.

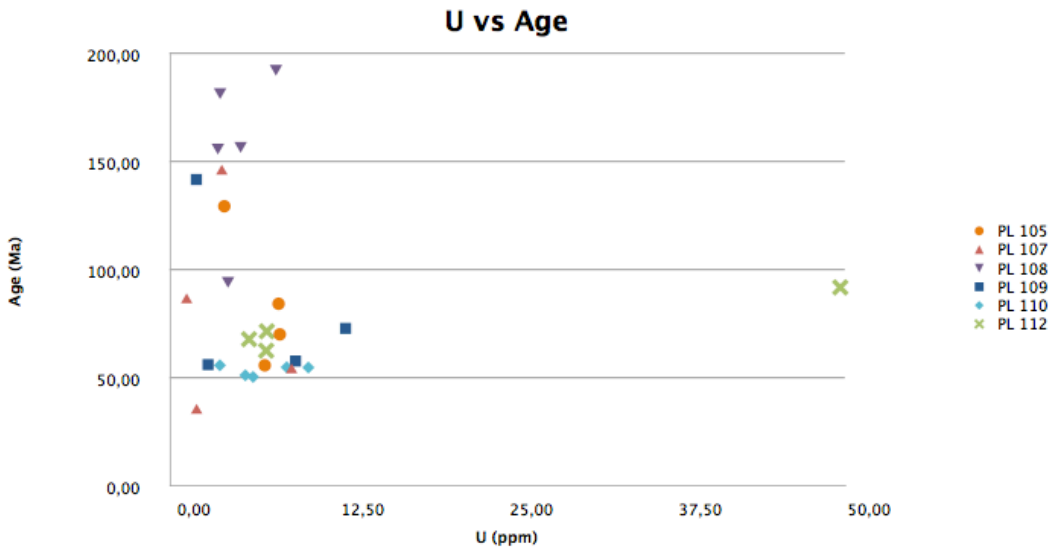


Fig 5.4 AHe single grain (distincted by belonging) ages plotted against Uranium concentration. The bad data was excluded.

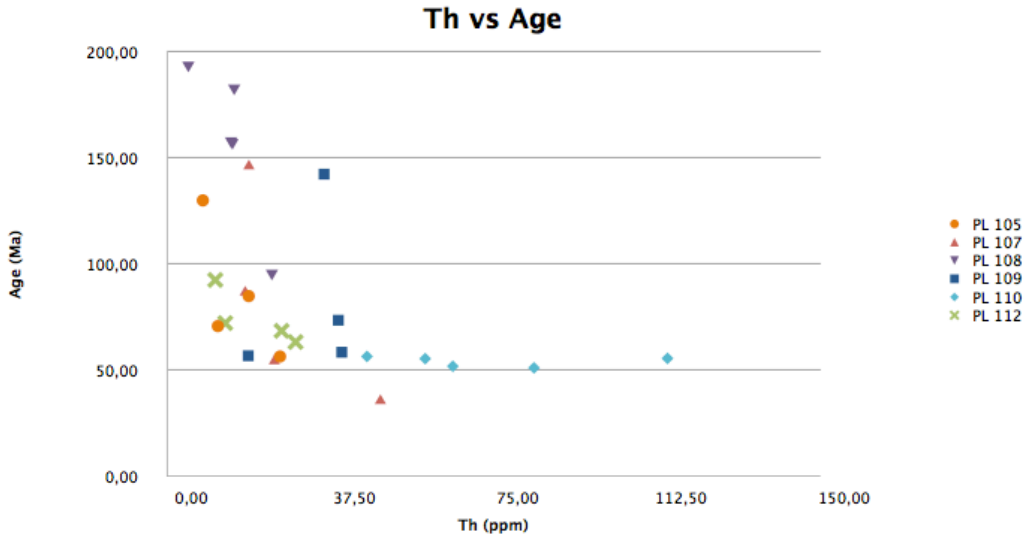


Fig 5.5 AHe single grain (distincted by belonging) ages plotted against Thorium concentration. The bad data was excluded.

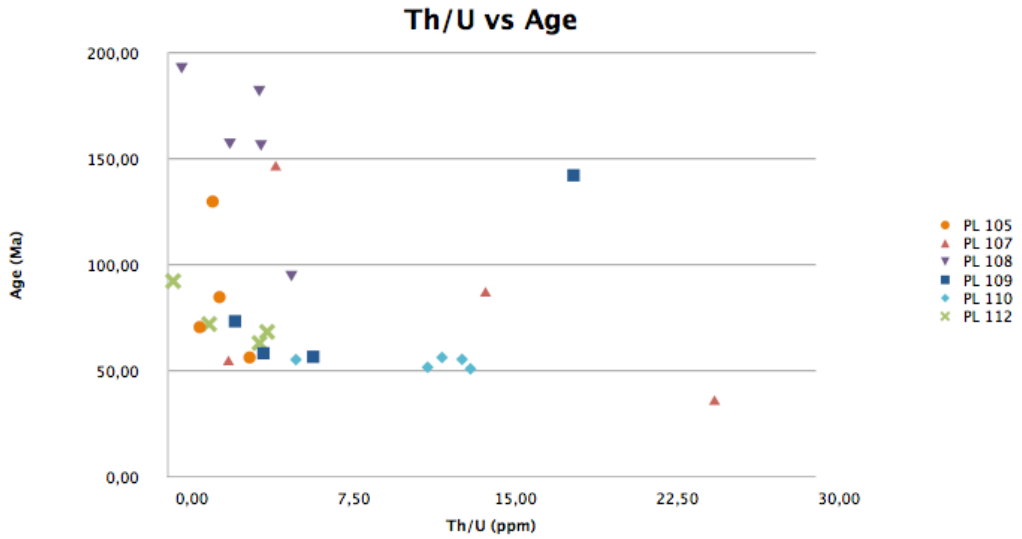


Fig 5.6 AHe single grain (distincted by belonging) ages plotted against Th/U ratio. The bad data was excluded.

All the diagrams in Fig. 5.4-5.6 show no straightforward correlation between dates and analytical values. Therefore, we can affirm that age data can be considered acceptable.

However, the age versus eU graphics require a more detailed approach and for this reason they will be discussed in Chapter 6.

## 5.2. AFT

Data provided by the fission-tracks analysis is used to support the results of the (U-Th)/He analysis. Their importance in this work is secondary and it is mainly related to employing them as a validation of the latter analysis.

Therefore, the fission-tracks analysis is performed on the same samples of the (U-Th)/He analysis and for each one the fission-tracks, spontaneous and induced, are counted for 20 apatite crystals. Usually is more advisable evaluating a larger number of crystals in order to improve the statistical

significance of the calculations. However, considering the minor importance of this method, a limited number of apatites is sufficient.

A provisional count has been performed on 10 apatites of PL105, PL108 and PL109, and the analysis was not continued owing to the bad quality of the crystals. PL110 displayed a high dispersion of the values that made them nearly useless in order to obtain a significant thermochronological age. PL107 and PL112 are fully analysed and the results are shown in the radial plot displayed in Fig 5.7-5.8. Alle the thermochronological ages of the samples are summarised in Table 5.4.

Table 5.4

The table show the stratigraphic age of the sample, the thermochronological age inferred by fissiont-tracks analysis and the standard deviation on the age.

| SAMPLE NAME | STRATIGRAPHIC AGE | AFT AGE (Ma) | DEVIATION (Ma) |
|---|---|---|---|
| PL 105 | Silurian | 131 | ± 16 |
| PL 107 | Silurian | 215 | ± 22 |
| PL 108 | Silurian | 109 | ± 18 |
| PL 109 | Triassic | n.d. | n.d. |
| PL 110 | Triassic | high dispersion | high dispersion |
| PL 112 | Permian | 105 | ± 13 |

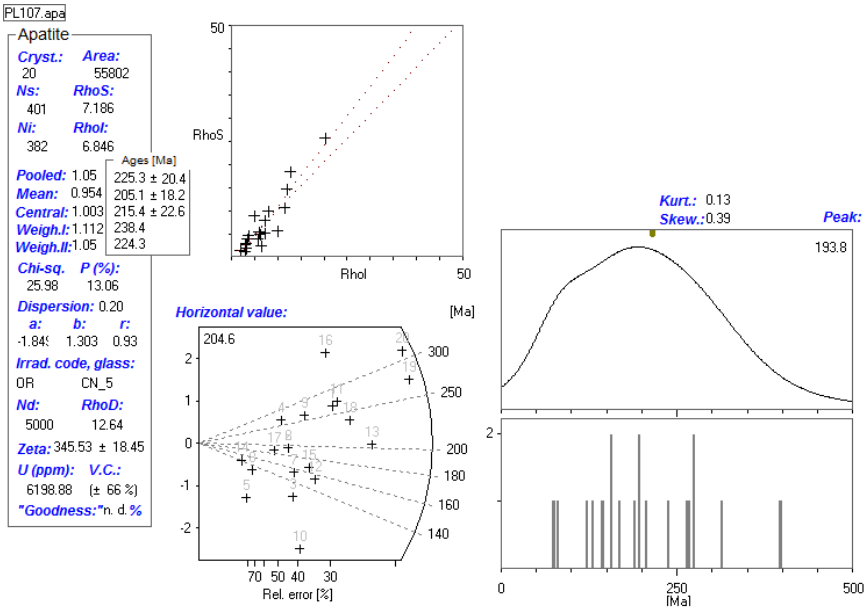


Fig 5.7 Radial plot for AFT analysis on PL107. Precision of single grain age is indicated on the horizontal axis; standard error is reported in the vertical axis. Radial plots were drawn using the TRACKEY 4.2 software (Dunkl, 2002).

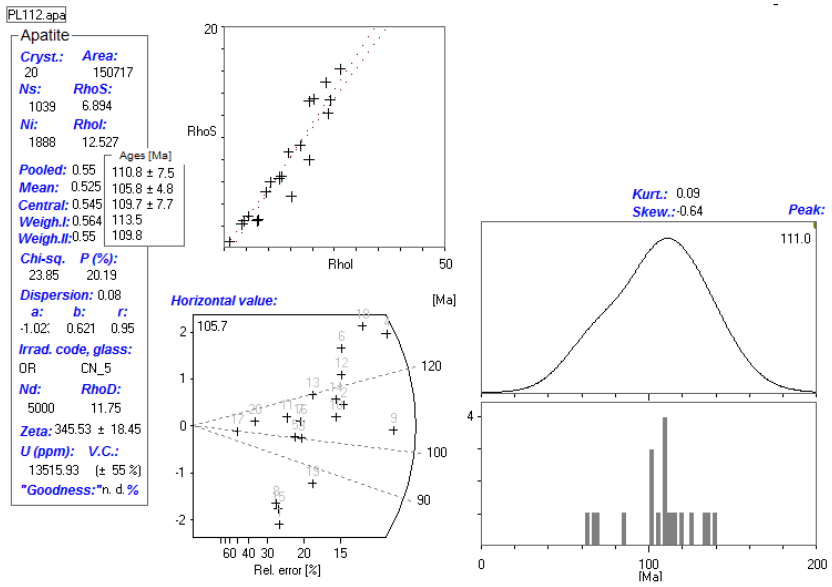


Fig 5.7 Radial plot for AFT analysis on PL112. Precision of single grain age is indicated on the horizontal axis; standard error is reported in the vertical axis. Radial plots were drawn using the TRACKEY 4.2 software (Dunkl, 2002).

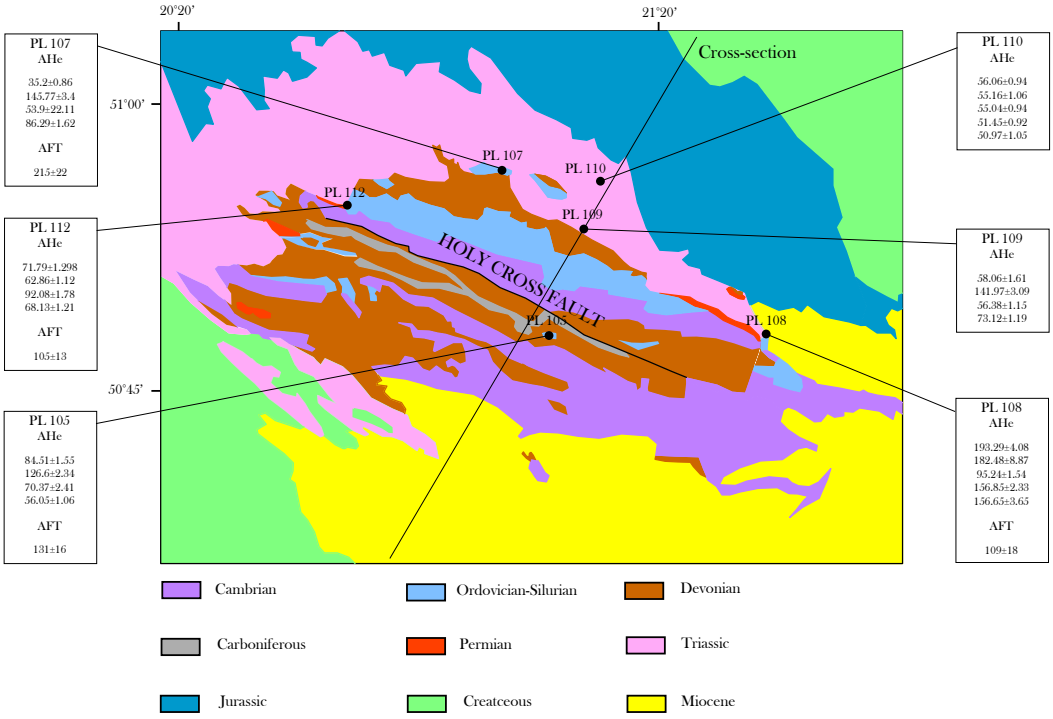


Fig 5.8 The map represents the stratigraphic units of the HCM, distincted by colour. The bolder black line marks the Holy Cross Fault, the other line identifies the chosen cross-section. The black circles show the location of the samples actually used for the thermochronological analysis.

In Fig 5.8, the AHe and AFT values are reported on the geological map, in order to provide a synthesis of the thermochonological data.

## 5.3. **BALANCED CROSS-SECTION AND SEQUENTIAL RESTORATION**

In the previous chapter, within the paragraph dealing with the Move procedures, the workflow to construct a balanced section was explained.
This is the key point for the final steps, the restoration of the section and the creation of the final structural model.
In order to apply decompaction to the strata to reconstruct their original thickness, it is necessary to know some physical parameter, especially the initial porosity of the rock, the elastic thickness, the Young's modulus, the crustal and mantle density etc. These values have been derived from other studies, or deduced from the lithology of the units.

Table 5.4

Main physical features which characterised the various lithologies.

| Litology | Matrix density | Initial porosity | Porosity reduction factor | Initial vertical permeability | Permeability reduction factior | Permeability anosotropy | Reciprocal compaction factor | Exponential compaction factor | Matrix thermal conductivity | Matrix thermal conductivity correction | Matrix heat capacity | Matrix thermal conductivity anosotropy |
|---|---|---|---|---|---|---|---|---|---|---|---|---|
| | [g/cm3] | | | [mD] | | | [1/km] | [1/km] | [W/m*C] | | [kJ/m3*C] | |
| Sandstone | 2.64 | 0.45 | 0.000175 | 30000 | 7 | 0.4 | 1.75 | 0.27 | 4.4 | 270 | 2800 | 1.55 |
| Siltstone | 2.64 | 0.55 | 0.00023 | 100 | 6 | 0.2 | 2.20 | 0.41 | 2.0 | 170 | 2650 | 1.55 |
| Shale | 2.60 | 0.6 | 0.0003 | 10 | 6 | 0.2 | 2.40 | 0.51 | 1.5 | -180 | 2100 | 1.55 |
| Limestone | 2.72 | 0.6 | 0.00019 | 5000 | 6 | 0.5 | 1.50 | 0.22 | 2.9 | 350 | 2600 | 1.55 |
| Dolomite | 2.85 | 0.6 | 0.0002 | 5000 | 6 | 0.5 | 1.50 | 0.22 | 4.8 | 300 | 2600 | 1.55 |
| Evaporite | 2.15 | 0.00 | 0.050 | 1.00E-09 | 1 | 1.0 | 0.00 | 0.00 | 5.4 | 470 | 1750 | 1.55 |

The cross-section validate through forward modelling has been manually corrected so that the geometry of the elements was actually possible.

The entire succession, from Precambrian to Cretaceous units can be observed. The Miocene is also present, but it has been omitted owing to its shallow thickness in this section, never exceeding 10 meters, and its poor importance for the reconstruction of the main tectonic events involving this area.

In the section six major faults cut the Paleozoic and Mesozoic successions. Five of them are listric faults, as they become sub-horizontal at a depth of 15 km as inferred by seismic studies (Guterch et al., 1994). Among them, the main fault is the Holy Cross Fault (the second from NNE), dividing the Łysogóry unit (NNE) from the Kielce unit (SSW).

The remaining fault, in the Kielce block, presents a very steep dip angle, ca. 85°, and it is much more recent than the other structures, probably post-Permian, since it cuts through the Carboniferous succession. This fault could be associated to the Mesozoic extensional event. The particular geometry of the HCF has been obtained by several iterative processes which are aimed to minimise the difference between the model generated by Move's algorithms and the field evidences.

A description of the principal features at present day is shown in the Figure below.

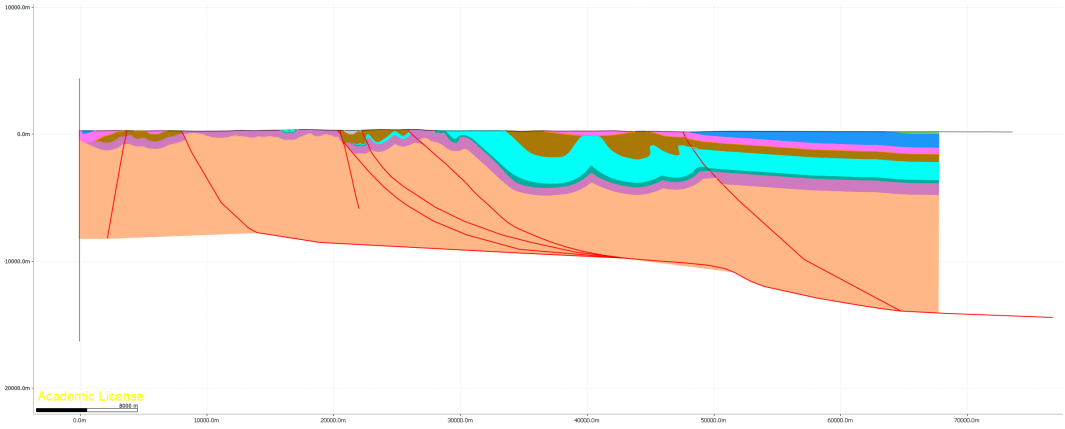


Fig 5.9 Present day cross-section.

As it can be seen, the Cretaceous strata have been dismantled by the massive erosion following the Laramide inversion (Late Cretaceous to Late Paleocene) and therefore they are absent in this section apart from a shallow strata in the Northern part.

From SSW proceeding toward the Northern block, can be noticed Upper Paleozoic (Permian) and Lower-Middle Mesozoic strata folded with SW vergence, lying above an unconformity which removes the Carboniferous and part of the Devonian beds. Mesozoic strata under the unconformity are also folded, although less intensely. In the central part, in the area South to the HCF, the Mesozoic succession is instead continuous and distinctly folded and Carboniferous strata are present. The block North to the HCF is divided by a listric fault with NE vergence: the Southern part presents Mesozoic strata intensively folded, cut by an unconformity which also in this case removes the Carboniferous and reduces the Devonian thickness; above the unconformity, Lower Mesozoic strata form a wide synclinal fold. In the Northern area the strata gently dip towards NE almost undisturbed and they are characterised by a constant thickness.

The construction of the balanced section makes the display of the eroded section.

The wide anticlinal structure particularly notable in the Cretaceous strata is the before-mentionated Anticlinorium, the origin of which dates back from the Laramide (Alpine) Inversion.

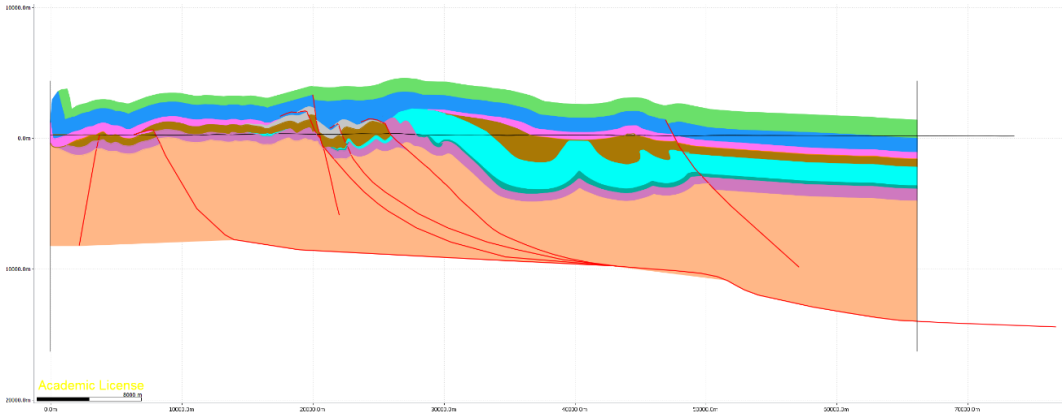


Fig 5.10 Reconstructed cross-section pre-Eocene erosion. The anticlinorium was generated by the Laramide orogeny.

The first step is the restoration of the the Cretaceous unit deformed by the Laramide orogeny. The Cretaceous bed is flattened to 0 m b.s.l. (regional datum) and the other successions are simultaneously taken back to its depositional context, which was a thick carbonate platform within a shallow marine context.

The Cretaceous succession is removed and the oldest strata are decompacted applying the Airy Isostasy algorithm; default values of the software are kept for Young modulus and elastic thickness parameters, whereas the density of the mantle is considered 3100 kg $m^{-3}$ and the density of the crust about 2950 kg $m^{-3}$, according with other studies on this matter (www.earthbyte.org/Resources/ICONS/EUR)

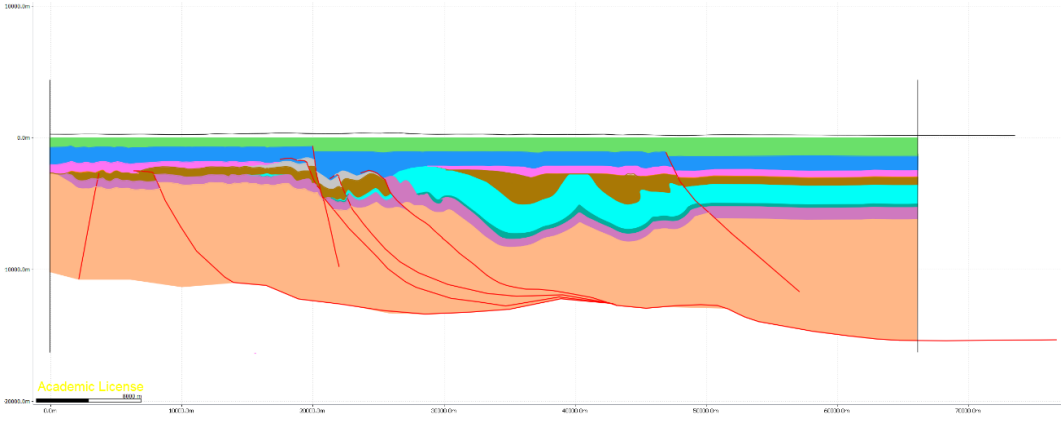


Fig 5.11 Reconstructed cross-section after the deposition of the Cretaceous unit.

The strata, then horizontal and undeformed, is later decompacted and its original thickness is restored. The estimate of the thickness of the Cretaceous succession is around 1000 meters in the less thick areas up to over 1600 meters at its maximum. A confirmation of this value derives from vitrinite reflectance data obtained by the lab of Roma Tre in the framework of this project..

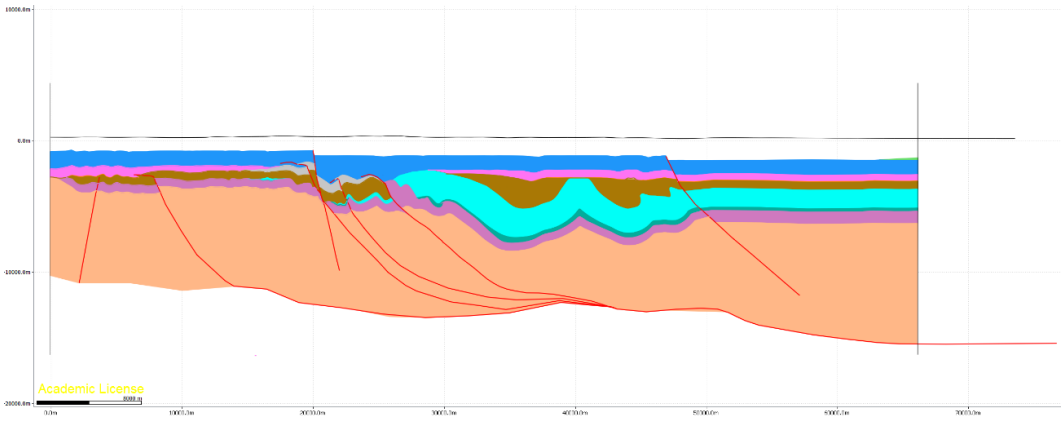


Fig 5.11 Reconstructed cross-section after the deposition and the faulting of the Jurassic unit.

The same processes of flattening and decompaction is applied to both the Jurassic and Triassic units, deposited in the same platform environment. However, the thickness of these bed is much more limited (around 600 meters).

During this step, the normal faulting which affected the most northward fault is restored using the Triassic as a template horizon.

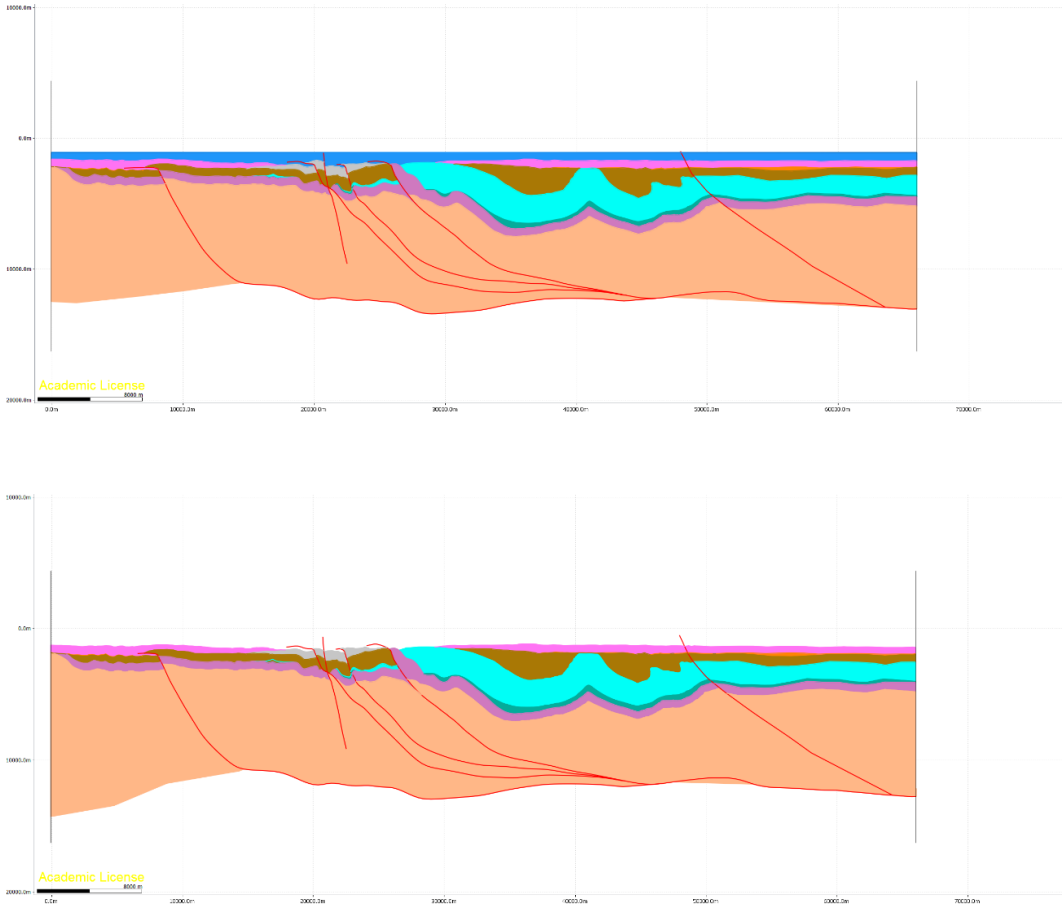


Fig 5.12-5.13 Reconstructed cross-sections showing the deposition of the Jurassic and Triassic units.

The Permian is characterised by a non continuous sedimentation (about 60 m thick succession) probably due to its shallow-water depositional environment. It unconformably overlays the Paleozoic successions in the northern and southern part of the section but it is absent in its central part. Indeed, the Permian is the first unit to sediment on the erosional surface which cross the older strata, from the Devonian to the Precambrian, and represents the massive erosion due to the uplift during the Variscan orogeny.

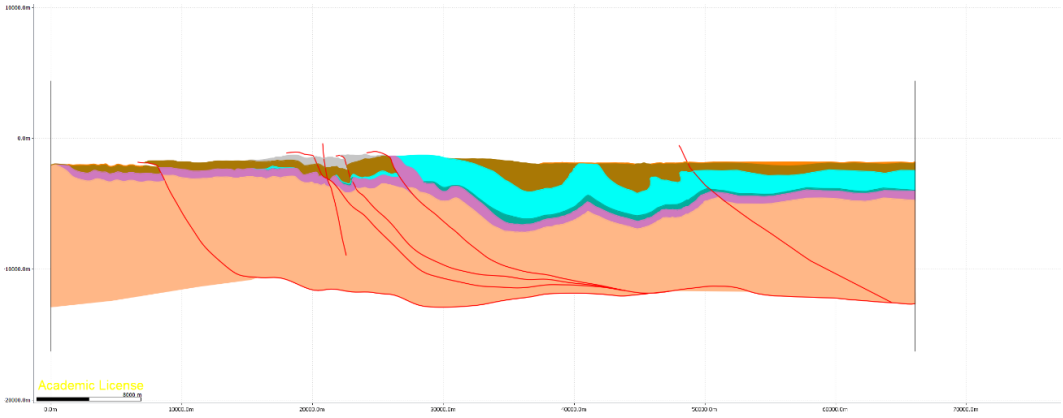


Fig 5.14 Reconstructed cross-section after the post-Variscan erosion.

The Permian unit is flattened , removed and the older succession below it has been decompacted The young, steep fault is restored to make the Carboniferous at the footwall and hanging wall coinciding.

The erosional surface is estimated, then the compressional structures deriving from the Variscan orogeny is reconstructed according to the forward model.

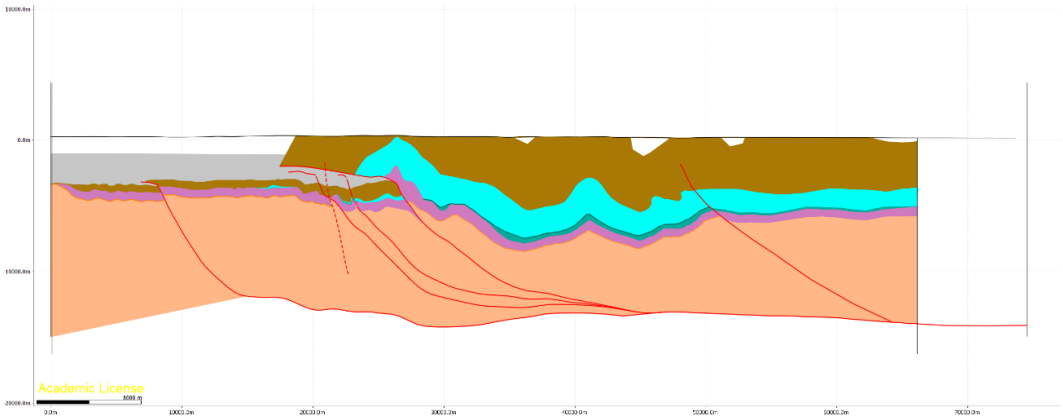


Fig 5.15 Reconstructed cross-section displaying the development of the Variscan orogeny. The black line represents the erosional surface.

The entity of the erosion which results from the model is compared with the burial history derived from the thermocronology. This discussion will be enhanced in the following chapters.

The reconstruction of the ramp anticline in correspondence of the HCF is used to restore the isostatic flexure generated by the increasing tectonic load on the footwalll. As a consequence of this restoration, the section experiences an uplift in the central part.

Then, the HCF is restored using the Devonian in the hanging wall and in the footwall as template horizon. The displacement recorded along this fault is about 8000 meters.

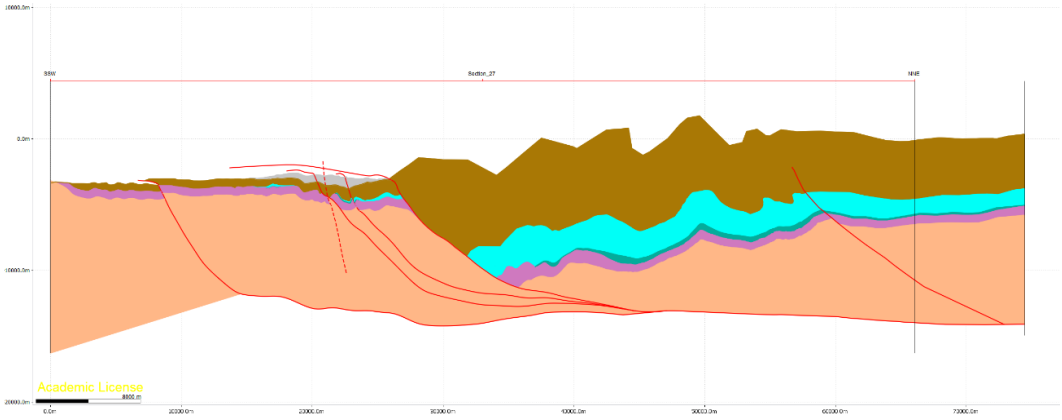


Fig 5.16 Reconstructed cross-section displaying the development of the first phases of the Variscan orogeny, in which big folds was created.

The syn-thrusting Carboniferous beds, , are then removed.

During the Devonian, the Northern block is affected by intensive folding as a consequence of the Variscan compression and buttressing produced by the horst rising in the southern Block.

After the bed has been correctly flattened, the decompaction is applied.

The thickness of the Devonian bed is markedly different from north to south of the HCF, suggesting an extensional tectonic occurring during this period.. In the Łysogóry unit the thickness ranges between 1800 and 3000 meters, whereas in the Kielce unit the thickness never exceed 250 meters.

These values concord with both the data from thermochronology and previous studies on the Paleozoic deposition rate in this area, endorsed by vitrinite reflectance data. The Devonian unit is now removed and the Silurian succession restored to its depositional position.

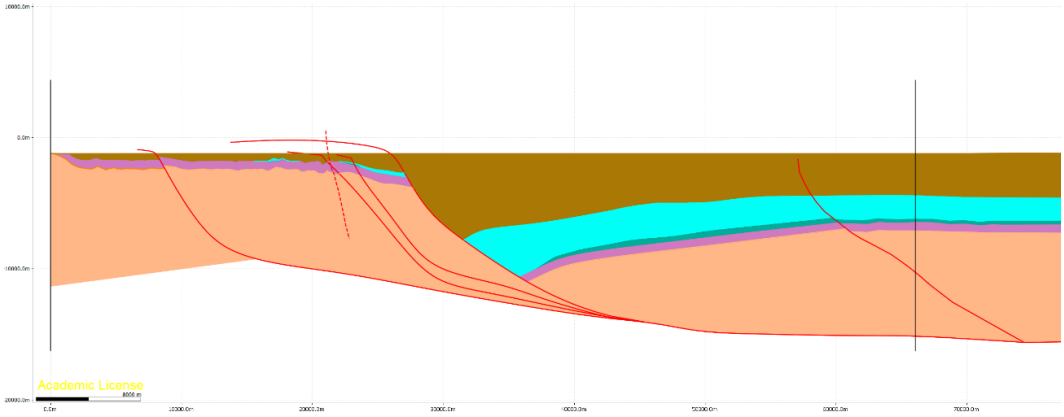


Fig 5.17 Reconstructed cross-section after the deposition of Devonian beds.

The thickness of the Silurian bed presents marked difference from the Łysogóry unit to the Kielce unit. North to the HCF its thickness varies from 800 to 1000 meters depending of the accommodation space, whereas it is almost missing in the south. In the Kielce block the Silurian is at most 20 meters thick, and its deposition is probably controlled by the geometry of the Cambrian substratum (e.g. synclinals).

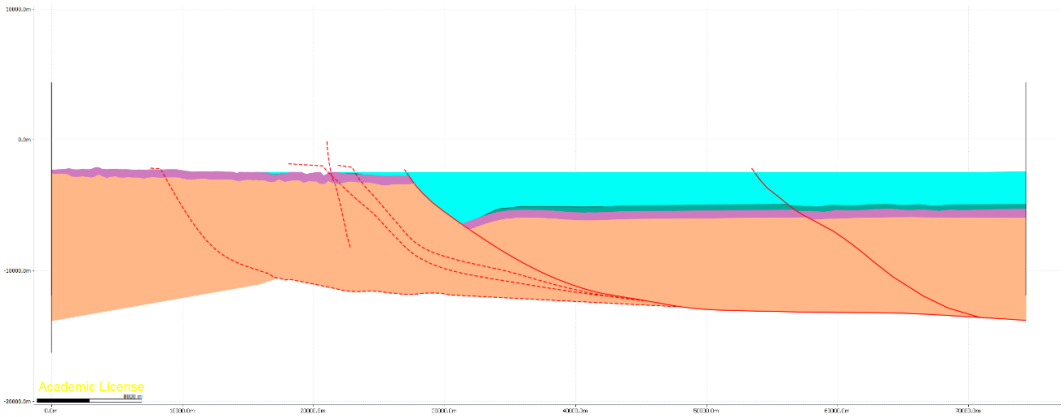


Fig 5.18 Reconstructed cross-section after the deposition of Silurian beds.

As for the previous step, the normal displacement along the HCF is restored and the Ordovician beds lead to the depositional position.

The Ordovician bed shows exactly the same behaviour of the Silurian sequence,. Its presence is almost negligible in the Kielce block and never exceeds the 120 meter in the north.

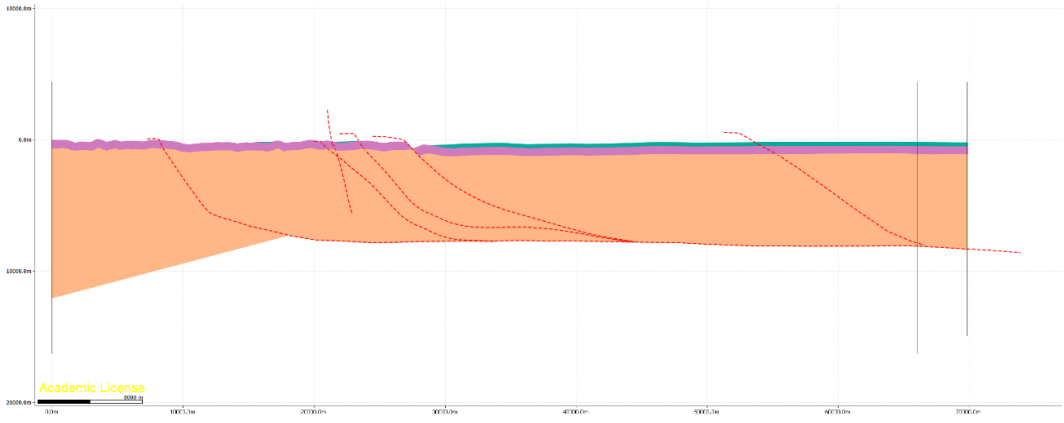


Fig 5.19 Reconstructed cross-section after the deposition of Ordovician beds.

The deposition of the Ordovician bed takes place in syn-rifting condition as the Caledonian orogeny occurs. Thus, during retrodeformation the thrusts are activated as normal faults progressively from north to south.

Eventually, the Ordovician unit is flattened, decompatted and removed.

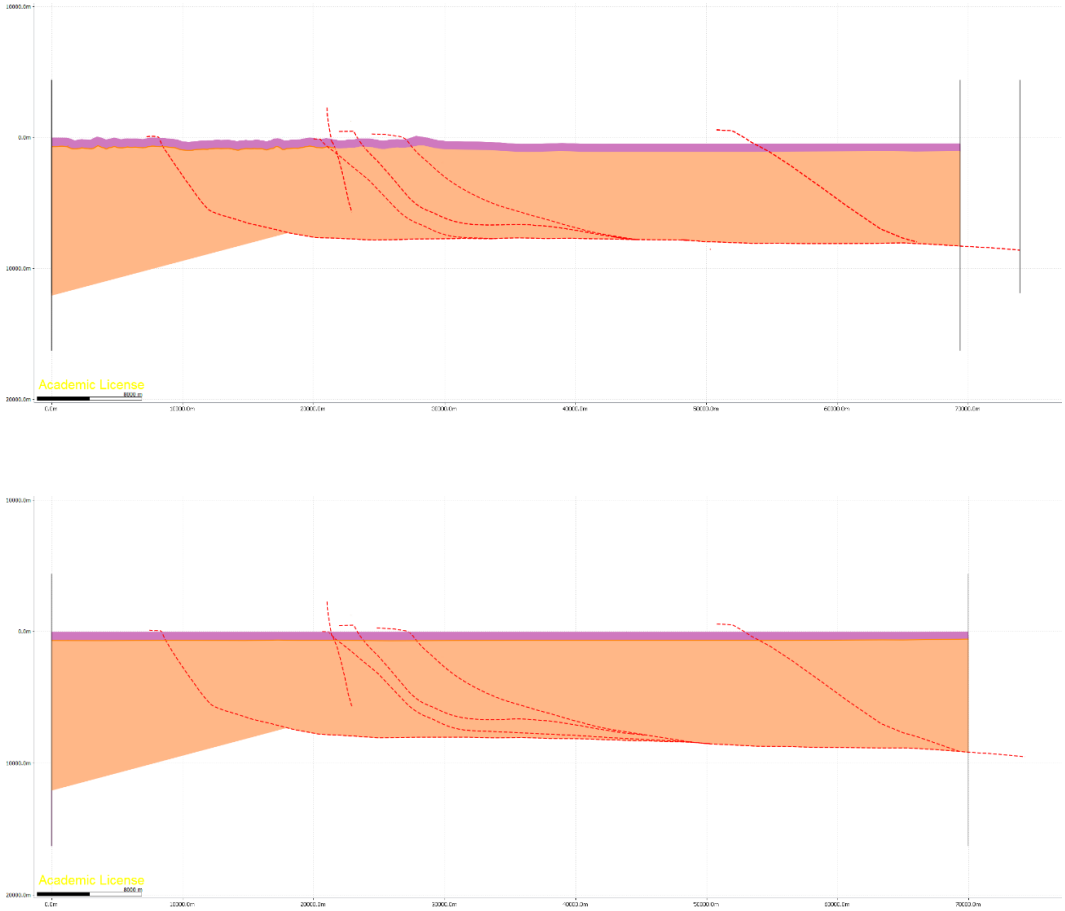


Fig 5.20-5.21 Reconstructed cross-section showing the folded basement beds (up) and the undeformed basement beds (down).

Performing the sequential restoration the first undeformed stage (starting point for the forward modelling) has been obtained.

The Cambrian beds lay on the Precambrian basement and their suggested thickness (ca. 600 meters) has been assumed to be constant along the section.

In this way, the cross-section is balanced and the suggested tectonic scenario is validated by the forward modelling.

# CHAPTER SIX
# INTERPRETATION OF THERMOCHRONOLOGICAL RESULTS

In this chapter, the results of the (U-Th)/He analysis will be discussed to achieve information about the burial-exhumation history of the samples and ultimately the whole area of the HCM. On this purpose, the basic parameters for data interpretation will be firstly provided.

## 6.1. MEANING AND USE OF THERMOCHRONOMETERS

As stated in chapter 2, the closure temperature (Tc) can be defined as the temperature of a system at the time given by its apparent age. The $T_c$ concept is actually an approximation of a temperature interval defined Partial Retention Zone (PRZ), through which the retention of the $^4He$ (in the case of AHe thermochronometer) progressively increase from base to top.

The "correct date" which is provided as output by the AHe analysis expresses the time at which the analysed grain cools enough to go below the $T_c$. If a rock which stayed for a period of time within a temperature range lesser than the $T_c$ is bought to a temperature high enough to reopen the system, some reset is possible. The reset can be complete or partial.

A completely reset sample shows typically low dispersion of single grain ages which are all very similar and always younger than their stratigraphic ages. A partially reset sample has low reproducibility of date values, displaying grain ages both younger and older than stratigraphic ages,. A third option is also present, namely a not-reset sample, which occurs when a sediment does not reach the $T_c$ since is deposition and exhibits high dispersion and grain ages older than stratigraphic ages.

A sedimentary succession usually experiments vertical movements during its history, due to tectonic or erosional causes. If the movement is directed upwards, the term "uplift" is used. A rock which undergoes uplift is moved from higher temperature to lower temperature, and hence it experiences cooling, on a rate which depends from the rate of the movement.
When a rock is uplifted, it usually undergoes exhumation therefore approaching the Earth's surface.
To the contrary, during the burial process the rocks are shifted downward by a combination of tectonic and sedimentary loading. The material is moved toward higher temperature and, if the burial is sufficient, it can be partially or completely reset.

## 6.2. FROM TC TO BURIAL HISTORY

The thermochronological ages of the samples provide information about the time at which the sample crosses the 60°C isotherm for cooling rates of 10°C/Ma for the AHe system, and of about 110°C for the same cooling rate for the AFT system.
High erosion rate produces the rising of the isotherms, which causes both an increase of thermal gradient and the introduction of uncertainty factors for the analysis of thermochronological data.

Fig 6.1 Influence of erosion rate on the thermal profile and closure temperatures at steady state (Reiners and Brandon, 2006). The thermal profiles are steady-state solutions for a one-dimensional thermal field with a steady erosion rate. Temperature is held fixed at the top and bottom of a 30-km thick infinite layer. Erosion is represented by a steady velocity through the layer. The specific thermal parameters used for this model are based on the northern Apennines of Italy, which is a fairly typical convergent orogeny: TS= surface temperature; TL=temperature at the base of the layer; HT= internal heat production ; Qs= heat flow at surface.The color lines show the effective closure temperature for apatite He (AHe), zircon fission track (ZFT), and muscovite Ar (MuAr) as a function of increasing erosion rate.

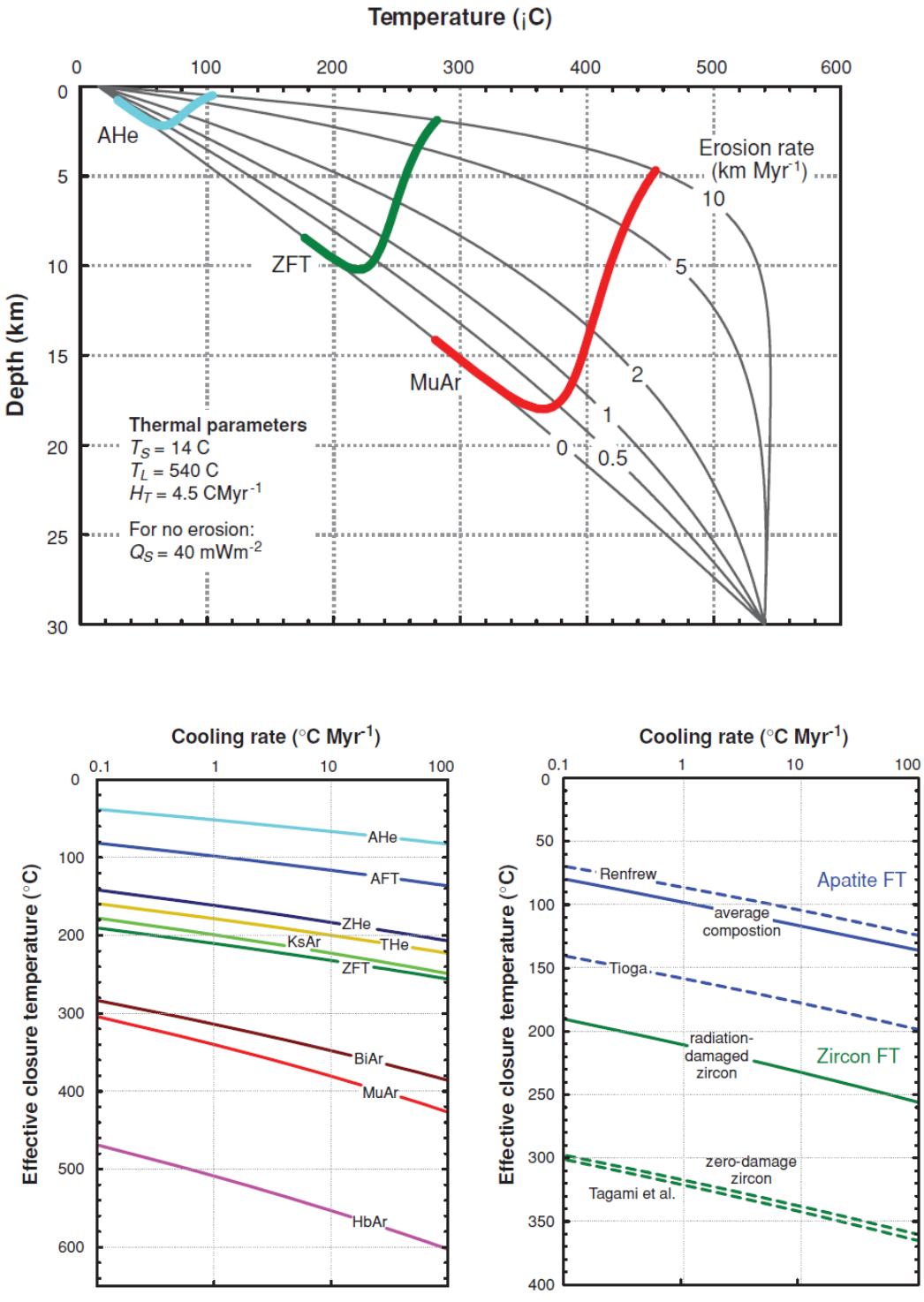


Fig 6.2 Effective closure temperature (Tc) as a function of cooling rate for common He, FT, and Ar thermochronometers (from Reiners and Brandon, 2006). Results were calculated using the CLOSURE program.

If the thermal field of the area can be derived from other studies and the erosion rate can be assumed as steady state, the $T_c$ can be related to a closure depth, which means the depth of the sample at the time of its closure.

In this way, the sample is constrained to be in a determinate position at the time indicated by its thermochronologic age. For instance, this data can be used to evaluate the slip of a fault, or the uplift and denudation of a rock.

## 6.3. DISPERSION OF AHe AGES

Age reproducibility of crystals indicates a total reset sample. However, age dispersion is sometime related to peculiar thermal histories. In fact positive correlations between He ages and grain size can be related to a prolonged period of slow cooling. Samples which underwent slow cooling were kept in the PRZ for a long time and show a discontinuous or incomplete transition from retention to diffusion of radiogenic He. Age dispersion can also be due to radiation damages. In this case, the grain He ages and the eU values would show a correlation.

However, in this case dispersion does not preclude the use of dates for reconstructing thermal histories, provided the RDAAM model of Flowers et al. (2009) which is able to quantify the effects of radiation damage in the temperature range of PRZ.

In all the cases described above, age dispersion can then be used to obtain information on the thermal history of the sample.

Indeed, age dispersion can also derive from crystal defects and, in this case, ages has not geological meaning. However, the main factors which cause dispersion are generally the presence of inclusions and coating, especially if they are composed by U-bearing and Th-bearing minerals, or pronounced roundness or abrasion in the grains, which can mislead the α-ejection correction.

On this purpose, the graphs Age vs. U, Age vs. Th and Age vs. Th/U can give some information. Reliable data do not show any kind of correlation among these parameters. As it can be seen by the before-mentioned graphics, previously plotted in Chapter 5, the dispersion of the values is high and no correlation can be found. Hence, the data seem not affected by any dispersion related to inclusions.

## 6.4. INTERPRETATION OF APATITE U-Th/He DATA

Ideally, the output product of the (U-Th)/He analysis is the thermocronological age of the sample which virtually constrains the examined strata in a specific position within a narrow time interval. However, the transition from retentive to diffusional behaviour of radiogenic He can be unclear and incomplete, especially if the samples remain protractedly within the PRZ or underwent slow cooling. In this case, the samples are only partially reset and the correct age which results from the analysis does not reflect the closure temperature: the samples show generic rejuvenation up to an age which ranges between the older original age and age related to the Tc. This effect is particularly pronounced in larger crystals compared to the smaller apatites, since the size affects both α-ejection and He diffusion kinetics: bigger crystal are more retentive due to the minor surface/volume ratio.

For this reason, plotted crystal size (Rs) and age values tend to correlate and arrange themselves along a straight line.

The values of all the replicates have been plotted, minus the bad data given by unfitting crystal, which were removed. In this figure a trend can be identified, although not very clear.

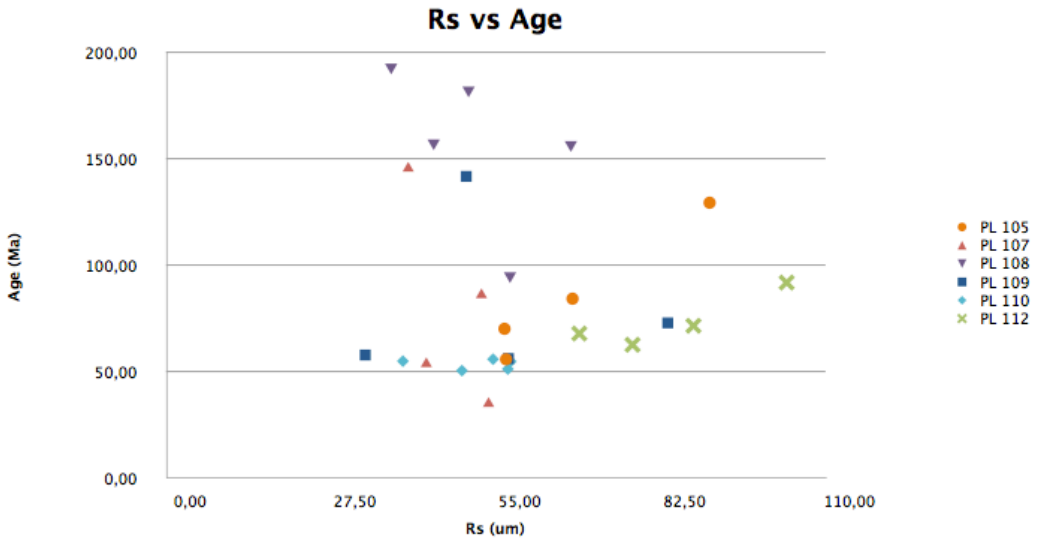


Fig 6.3 AHe single grain (distincted by belonging) ages plotted against grain radium. The bad datas was excluded.

Considering every sample in an independent way, it can be noticed that:

-PL 105 shows medium-high dispersion and a rather clear trend, which symbolise that slow cooling occurred.

-PL 107 displays very high age dispersion and no pattern can be recognised, limiting the role of slow cooling.

-PL 108 exhibits very high age dispersion, but it is characterised by a peculiar disposition of the values in a negative-pendency trend. Smaller crystals seems to be more retentive than larger one, probably because of compositional difference.

-PL 109 shows high dispersion and it lacks the radium-age trend.

-PL 110 displays very high age reproducibility and no radium-age trend.

-PL 112 exhibits a quite narrow range of ages, and a clear positive trend,.

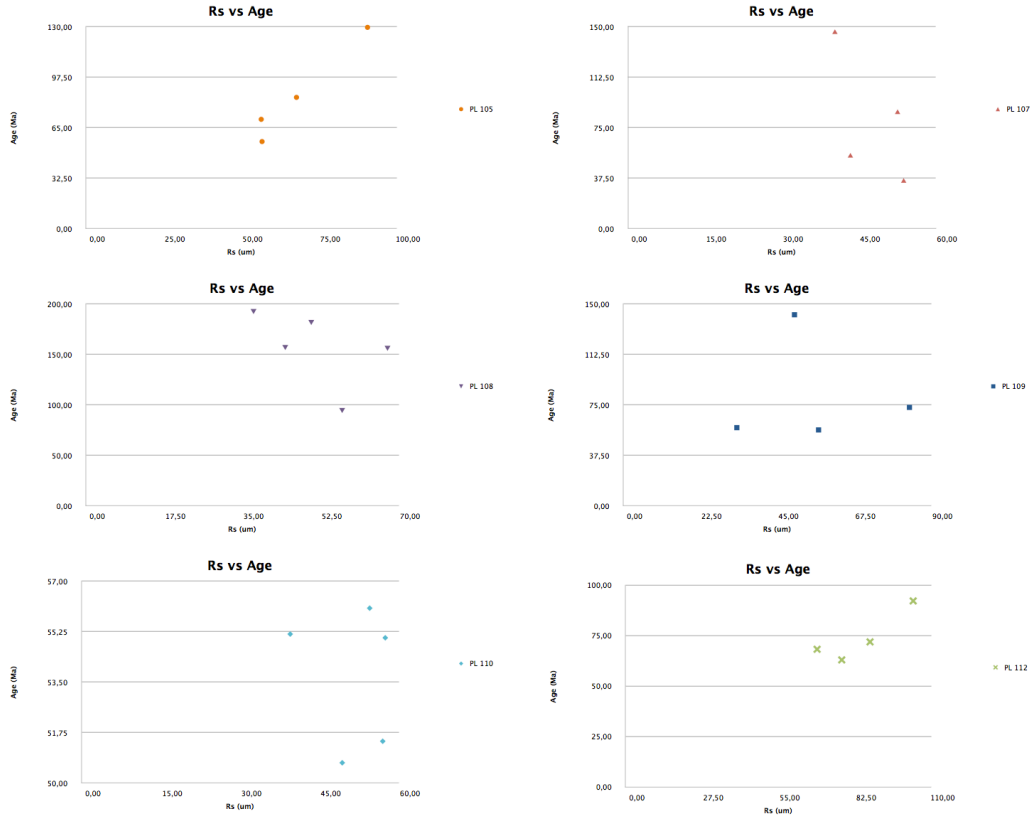


Fig 6.4 AHe single grain ages plotted against grain radium. The thermochronological age values have been clusterised by the sample. The bad datas was excluded.

The data acquire even more significance if plotted not clustered on the basis of the belonging of an apatite to a particular sample, but gathering the values according to their age. In the first figure the distinction is made between lower Cretaceous and older dates and Upper Cretaceous and younger ages. Two groups can be distinguished, which are characterized by different trends that reflect two very different histories.

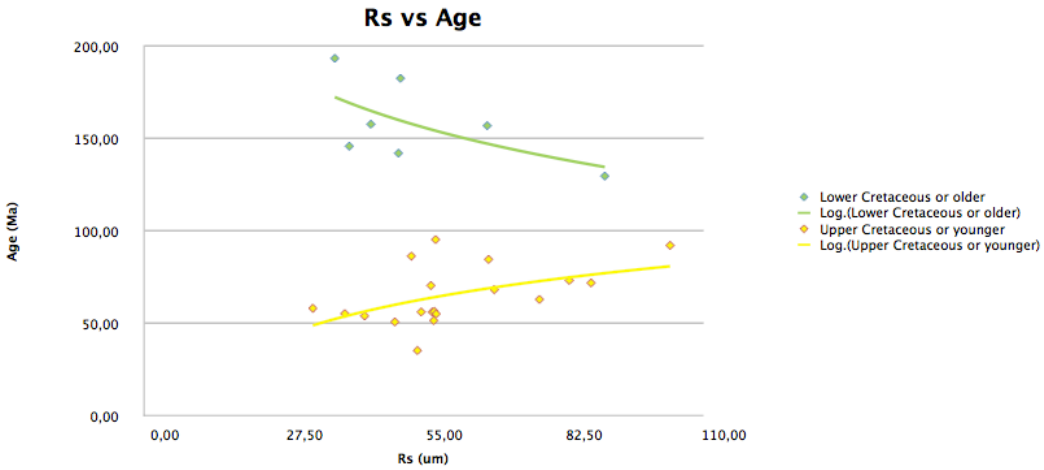


Fig 6.5 AHe single grain ages plotted against grain radium. The bad datas was excluded. The thermochronological age values have been clusterised in Lower Cretaceous and older ages and Upper Cretaceous or younger ages.

In the second graph, in which the values are divided in Cenozoic and Mesozoic samples, the difference is even more accentuated.

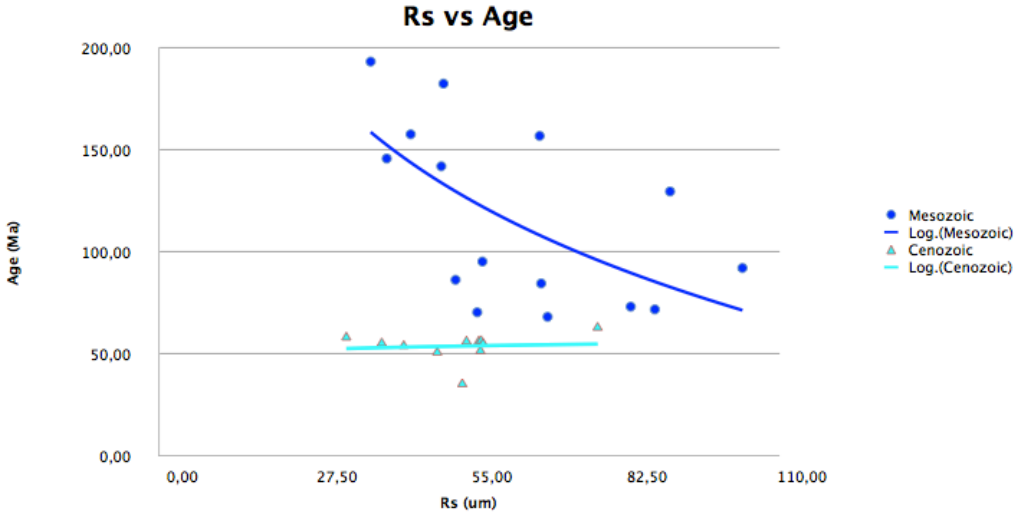


Fig 6.6 AHe single grain ages plotted against grain radium. The bad datas was excluded. The thermochronological age values have been clusterised in Lower Cretaceous and older ages and Upper Cretaceous or younger ages.

We can hypothesized that all the samples underwent slow cooling, the importance of which is greater in some crystal than others. Particularly,

older crystals shows a higher grade of dispersion. Probably, given the complex thermal history, those crystals crossed the $T_c$ much before before the eventual exhumation and therefore small differences in crystal structures and chemical composition greatly influenced the final age values.
For this reason, radium-age graphs alone indicate that younger values should be considered the most reliable and accurate.

This interpretation is confirmed by Uranium versus age relationships. The eU parameter is quite important in the analysis because it reflects the sensitivity of the crystal. A high value of eU indicates a more sensitive apatite, allowing to record more precisely the thermocronological age. In the Fig. 6.7 it can be seen that the values arrange themselves in an hyperboles: all the older ages are characterized by low values of eU, whereas the higher eU is contained in the younger crystals.

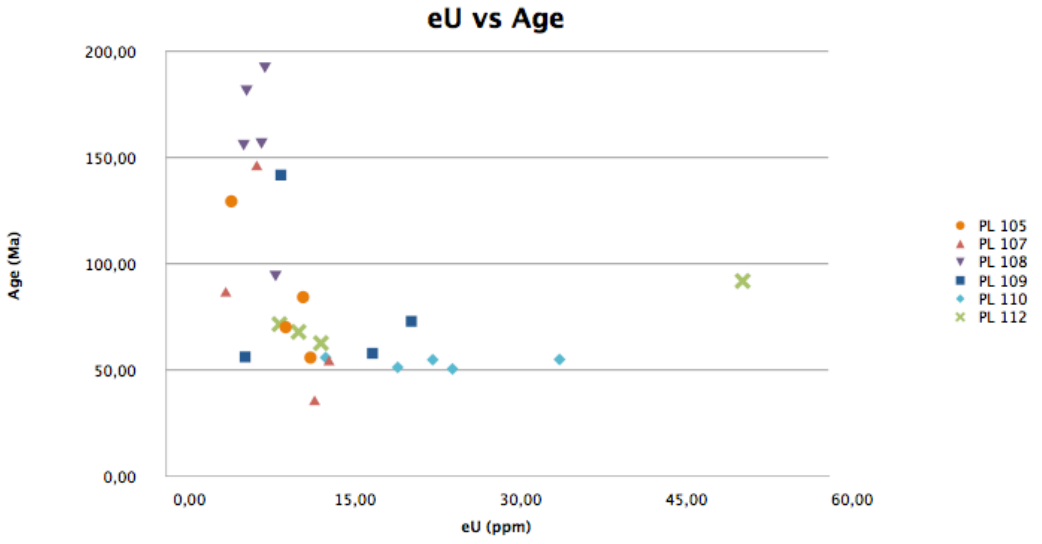


Fig 6.7 AHe single grain (distincted by belonging) ages plotted against effective Uranium content. The bad datas was excluded.

Hence, the younger ages cluster can be rightly considered the more reliable.

A comparison with available AFT data confirm that only younger AHe ages can be considered reliable. In fact, AFT system is characterized by a higher $T_c$ so AFT ages should be older than AHe ages detected on the same sample.

In conclusion, we can consider the values inferred by PL110 as the most reliable data, followed by PL112. Both of them recorded an uplift and exhumation event about 55-60 Ma ago. The other samples show a more or less intense grade of partial reset, which caused the scattering of the thermochronological values.
AFT analysis on PL112 recorded an older uplift event which occurred 100-110 Ma ago. Finally, AHe analysis on PL108 and AFT analysis on PL107 indicates a much more older event dated 210-215 Ma ago. The meaning of this result will be discussed in Chapter 7.

# CHAPTER SEVEN
# DISCUSSION

(U-Th)/He data are characterized by general dispersion of the values, depending both on the complex thermal history which held the samples within the PRZ for prolonged time, and mostly on the occurring of markedly slow cooling in the area. For all the reasons previously discussed , younger thermochronological ages, recorded in smaller and more sensitive crystals, can be considered more reliable,. Hence, the (U-Th)/He analysis indicate that a general uplift of the Holy Cross Mountains occurred about 55-60 Ma, between the Paleocene and the Eocene. This uplift derives from the final phases of the Laramide orogeny (Lower Cretaceous to Upper Paleocene), when the uplift rate previously constant and slow seems to undergo a sudden acceleration, probably of short duration. After that period, the Miocene subsidence or other tectonic phases were not sufficient to reset the crystals, so the subsidence had to be scarce.

AFT data also exhibit dispersion and present ages of 100-110 Ma, older than AHe. These ages seems to be too old to belong to the early stages of the Laramide orogeny but they could be related to a thermal history with a long permanence in the Partial Annealing Zone. In other words, the ages here detected have not a particular geological meaning as the original ages, probably derived from the Variscan orogeny, could have been rejuvenated throughout a very slow and prolonged subsidence. One sample displays abnormally old AFT ages ( Triassic), which indicate a minor grade of reset..

## 7.1. TECTONIC EVOLUTION OF THE HCM

The most ancient lithology is the meta-argillites of Upper Precambrian succession which belongs to the complex originated during the Baikalian orogeny in the Upper Proterozoic (850-570 Ma). This layer constitutes the basement of the whole rock column. In the Lower and Middle Cambrian (570-520 Ma) the massifs were eroded and became a peneplain. Therefore we can assume a constant thickness of Cambrian beds along the section, evaluated of 600 meters.

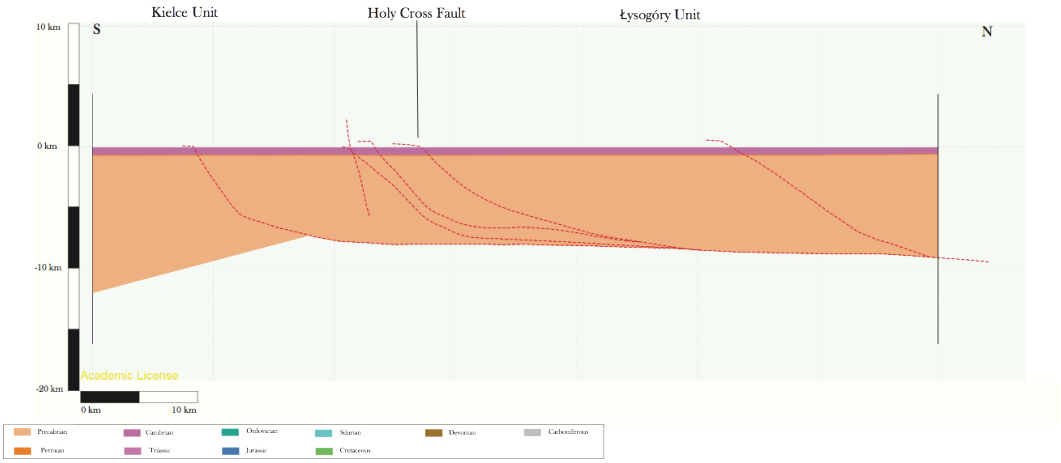


Fig 7.1 Reconstructed cross-section showing the undeformed basement beds and the Cambrian.

In the Late Cambrian, these successions underwent a compressional phase which generated asymmetric folds. This stage is associated to the late Tremadocian-Sandomirian Orogeny (Early stage of Caledonian orogeny), related to the anticlockwise rotation of Baltica between 500 and 490 Ma (Torsvik et al., 1996). The compression created in this way is sufficient to generate the folding, but it is not enough in order to activate the thrusts.

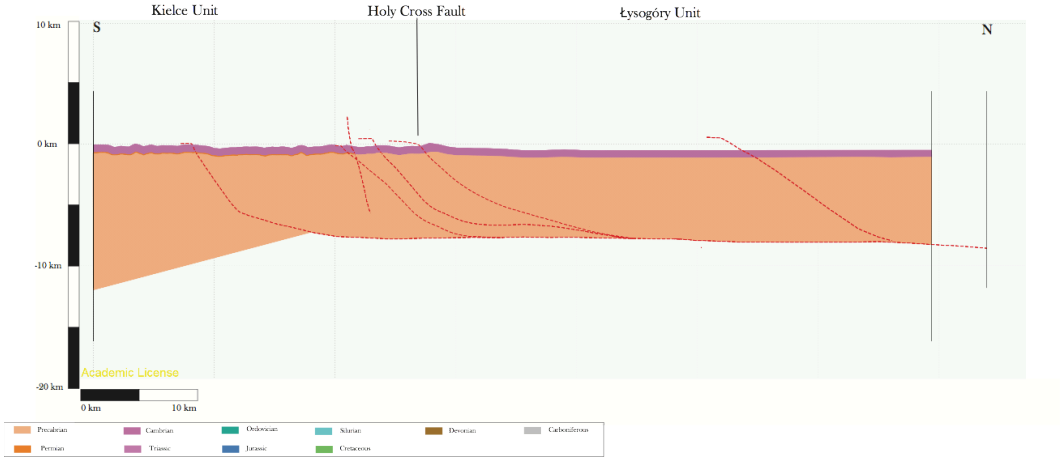


Fig 7.2 Reconstructed cross-section showing the folded basement and Cambrian beds.

The Cambrian-Ordovician (485 Ma) transition marked the passage from compressive to extensional conditions, as a consequence of the Caledonian orogeny, that took place from the Ordovician to the early Devonian (490-390 Ma) further to the north. The study area belonged to the Caledonide foredeep and therefore some subsidence due to flexural bending occurred. In the Holy Cross area, the faults were activated with normal displacement from North to South during the Ordovician when deep water deposits sedimented in the Lisogory block, whereas very minor deposition occurred in the Southern block, which assumed the features of a condensed section.

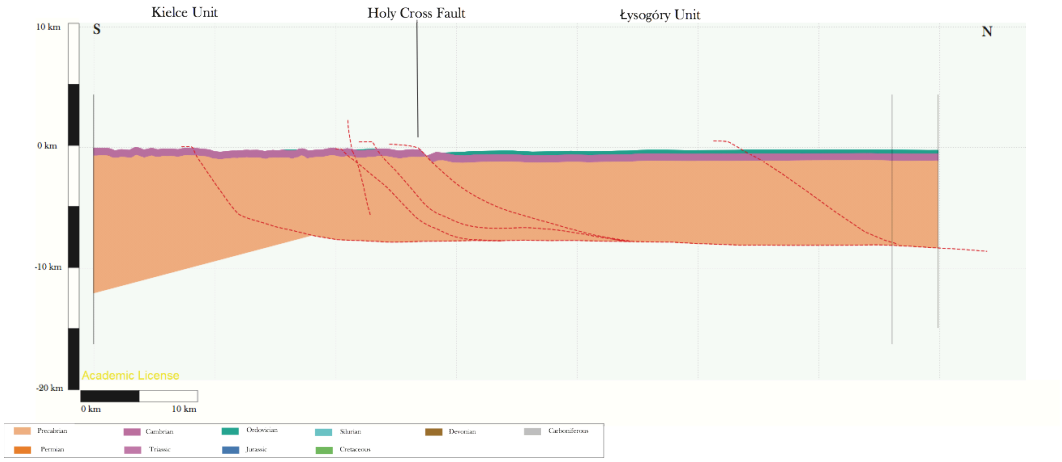


Fig 7.3 Reconstructed cross-section showing the activation of normal faults and the deposition of the Ordovician unit.

During Silurian times, sedimentation of Silurian mudstones occurred in post-rift conditions while the sediments progressively filled the accommodation space and produced a forced marine regression. The last phases of extension are expressed by some displacements along the HCF . The throw accommodated by the HCF was probably of about 4000 meters, with thickness of the sedimentary succession ranging from 1000 meters to the North to few meters in the South, where the deposition occurred only in the Sandomirian synclinals as a condensed section.

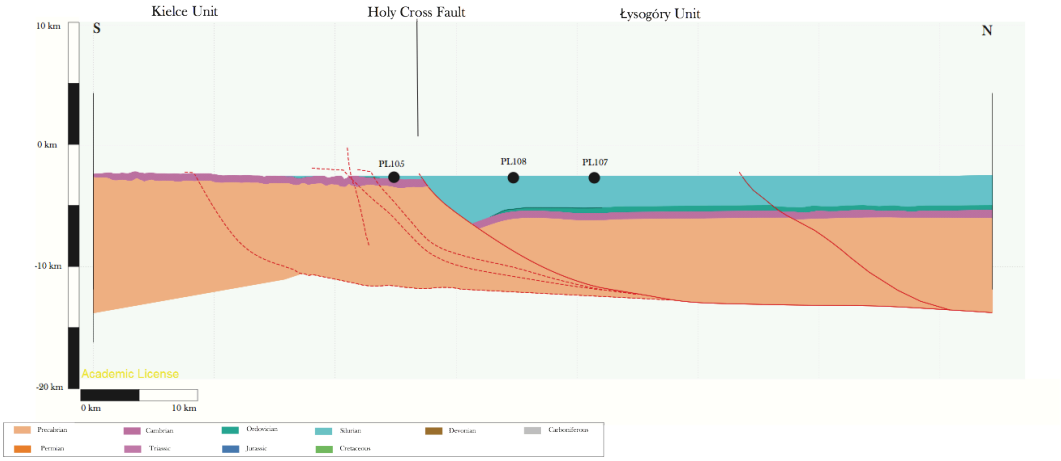


Fig 7.4 Reconstructed cross-section showing the activation of normal faults and the deposition of the Silurian unit. The black circles show the location of the samples.

The rifting phase lasts till 390 Ma (Lower-Middle Devonian), when the Silurian normal faults have been reactivated. Devonian deposits start as thick carbonate platform reaching a thickness of 3000 meters in the Łysogóry unit, whereas in the Kielce unit never exceeds 250 meters. The accommodation space was maximum in correspondence of the hangingwall of the HCF. Here the tectonic and the sedimentary loads were surely enough to completely reset the samples North of the fault (PL107, PL108) whereas the reset degree South of the fault (PL105) is unknown.

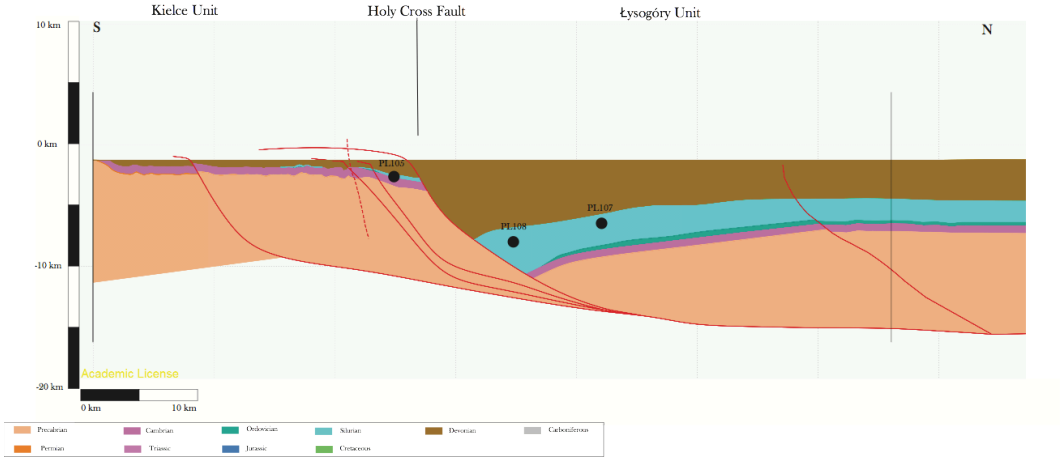


Fig 7.5 Reconstructed cross-section showing the activation of normal faults and the deposition of the Devonian unit. The black circles show the location of the samples.

A new remarkable tectonic inversion with related uplift took place during the Variscan orogeny (Late Devonian to Triassic, 380-250 Ma). All the strata from Precambrian to Carboniferous were intensely folded showing buttressing produced by the horst in the Kielce Block, initially without the activation of thrusts.

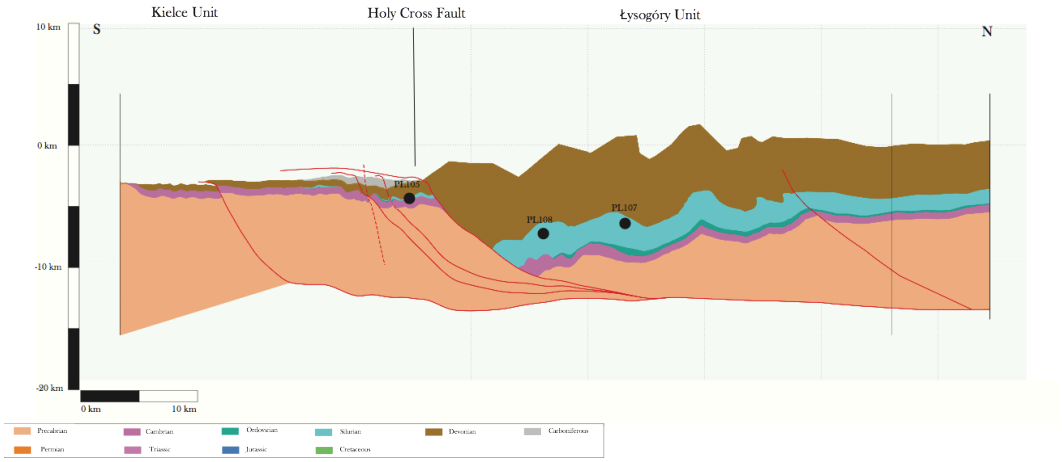


Fig 7.6 Reconstructed cross-section showing the folding of the strata during the first phases of the Variscan orogeny. The Carboniferous unit deposits are syn-orogenic. The black circles show the location of the samples.

As a consequence of the increasing compression, the faults started to be activated as thrusts along a south to north trend. A significant part of the uplift occurred between 360 and 320 Ma ago. The fault displacement

recorded along the HCF was up to 8000 meters, producing an intense crustal shortening. This uplift event surely made the crystals in samples PL109 and PL110 left the PRZ and cooled enough to cross the $T_c$ of both thermochronometers. The uplift rates were elevated, so the cooling can be considered rapid and brief in time.

The syn-thrusting Carboniferous beds (360-330 Ma) deposited while the orogen was uplifting and therefore they were present only South to the HCF. Their remarkable thickness is probably due to the subsidence generated on the Kielce block by the weight of the growing orogen. The erosion is remarkable in at the front of the HCF where the hangingwall reach its maximum structural relief. The intense erosion greatly diminished the thickness of Devonian strata and removed almost completely the Carboniferous beds, generating an unconformity. As a consequence, during the last phases of Carboniferous (320-330) the area underwent an uplift due to unloading.

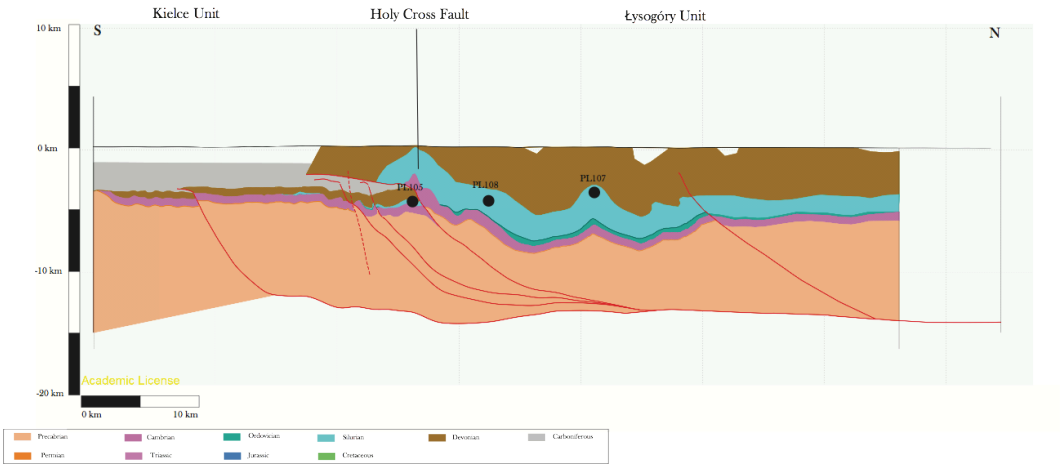


Fig 7.7 Reconstructed cross-section showing the activation of thrusts during the Variscan orogeny.Major role of the Holy Cross Fault. The Carboniferous unit deposits syn-thrust. The black circles show the location of the samples.

The uplift event lasted until the Permo-Mesozoic, when subsidence conditions were restored. The Polish Basin belonging to the European Basin became epicontinental.

The Permian is the first unit to sediment on the erosional surface and it is characterised by a non continuous sedimentation and a thickness of about 60 meter. PL112 sedimented within these beds, in a shallow marine context with terrigenous stages.

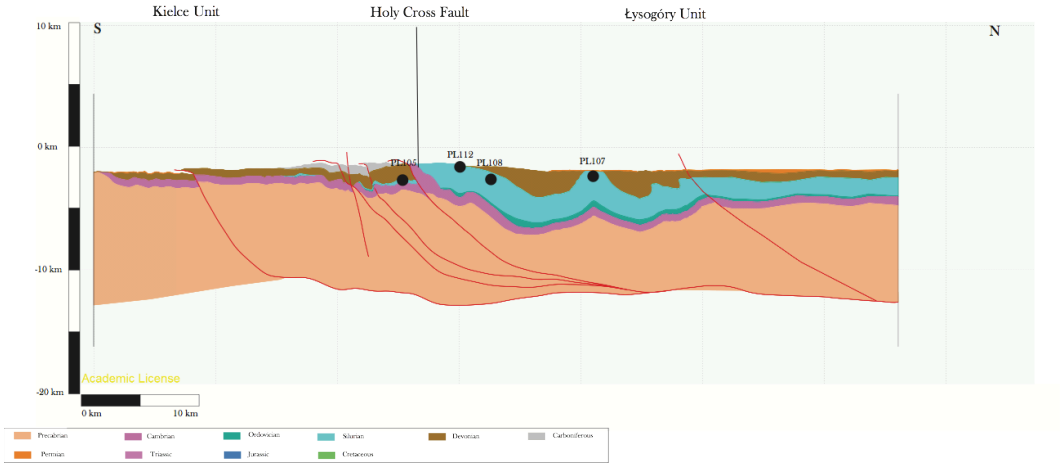


Fig 7.8 Reconstructed cross-section after the post-Variscan erosion. The black circles show the location of the samples.

The Mesozoic successions settled under the same conditions of slow subsidence. Within the Triassic a carbonate platform definitively took place into the basin, reaching about 600 meters of thickness. Triassic carbonates were intercalated with both evaporite layers which represented marine regression and desiccation of the basin, and open marine sediments related with marine transgression. The same conditions characterised also the Jurassic, when alternations of regression and transgression took place. Although these cycles can not be certainty attributed to tectonic causes, surely indicate that the occurring subsidence was not sufficient for a persistent marine regression to happen. Hence, it can be though that the subsidence in this period of time was slow and multiphase. The samples underwent slow cooling within the PRZ crossing the $T_c$ at different times.

This peculiar tectonic history is the cause of high dispersion in the (U-Th)/He values. The AFT analysis on PL107 shows a Triassic thermochronological age. This values might represent a restricted uplift phase in a general subsidence context, but partial reset of the samples is also possible, with crystals rejuvenated from older Carboniferous ages.

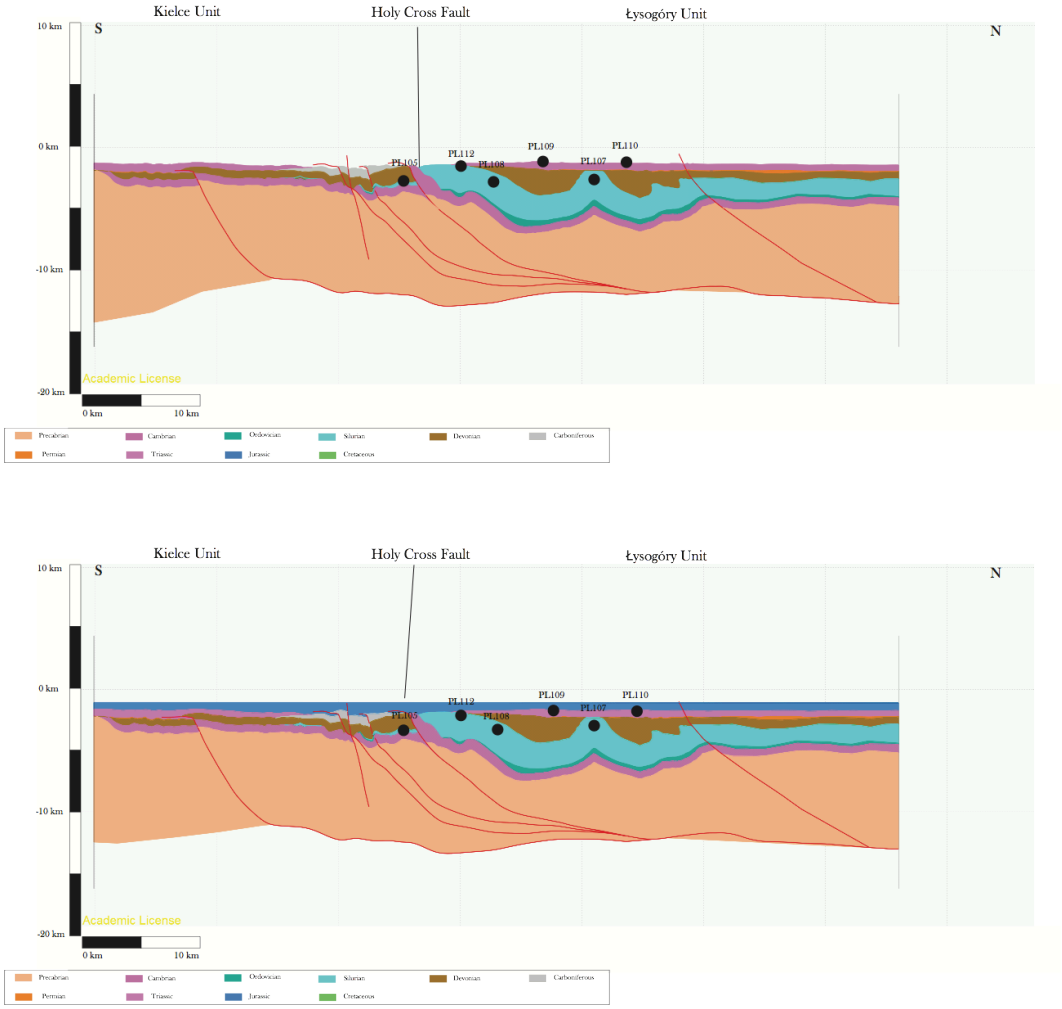


Fig 7.9-7.10 Reconstructed cross-sections showing the deposition of the Jurassic and Triassic units. The black circles show the location of the samples.

The Lower Cretaceous were characterised by more marked subsidence condition, and the thickness of the carbonate platform probably reached 1000-1600 meters. These subsidence was the cause for the partially (PL105, PL107, PL108, PL109) or totally (PL110, PL112) reset of the (U-Th)/He

thermochronometer. Enhanced subsidence rates are also notable in the reactivation from North to South of some of the faults with a normal displacement.

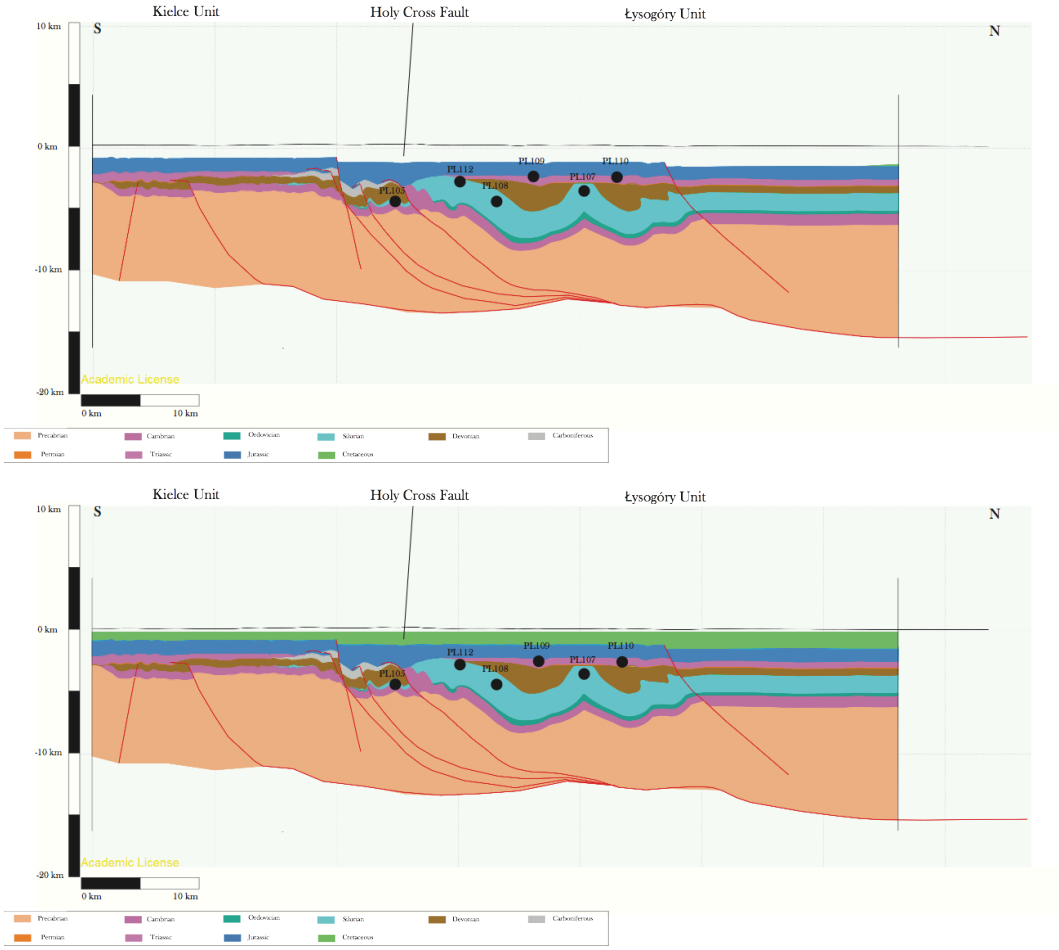


Fig 7.11-7.12 Reconstructed cross-section after the deposition and the faulting of the Jurassic unit (up) after the deposition of the Cretaceous unit (down). The black circles show the location of the samples.

An eventual tectonic inversion is produced by the Laramide orogeny (Late Cretaceous to Late Paleocene, 100-55 Ma), from which derived the wide anticlinal structure that folded the whole succession, without thrusts activation. The occurring uplift promoted the cooling of the samples previously reset during the Mesozoic, as testified by the AHe data. Since this tectonic event, no major deformations and tectonic movements took place.

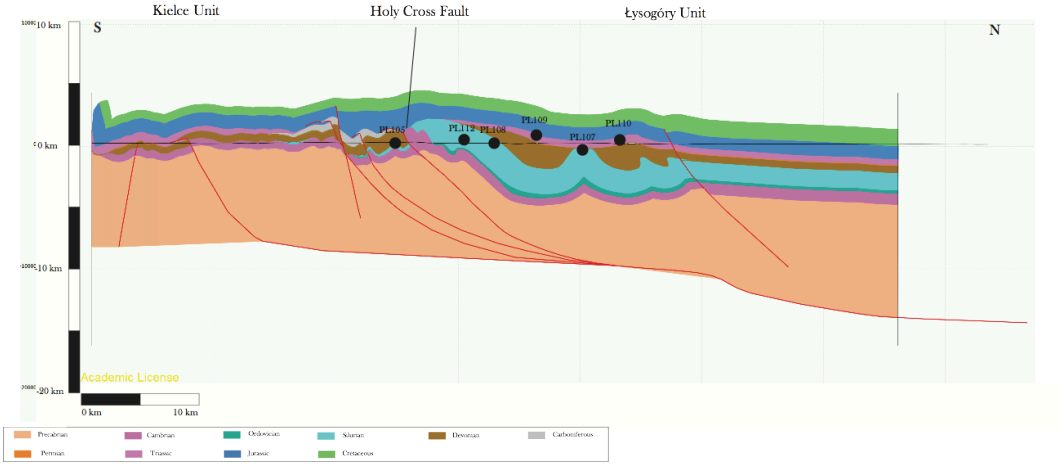


Fig 7.13 Reconstructed cross-section pre-Eocene erosion. The anticlinorium was generated by the Laramide orogeny. The black circles show the location of the samples.

Intense erosion removed most of the Mesozoic strata and exposed the Paleozoic core of the Holy Cross Mountains.

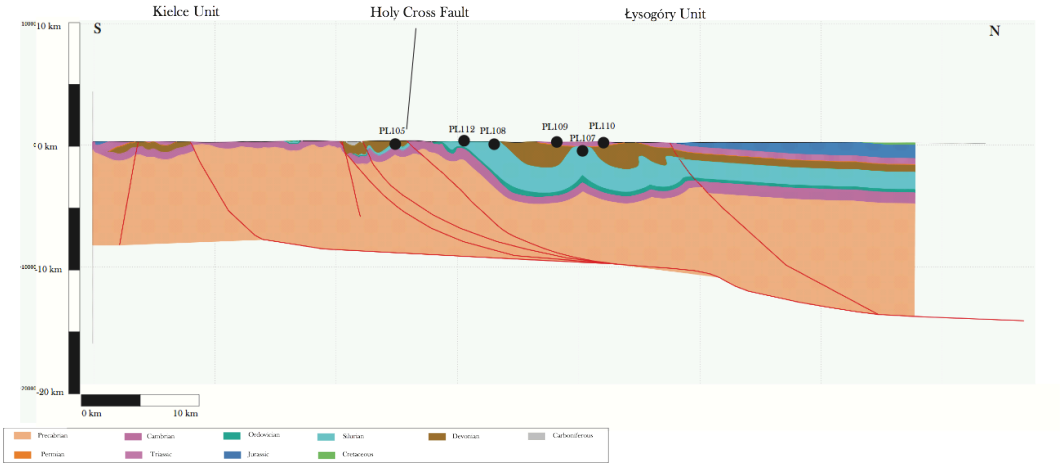


Fig 7.14 Present day cross-section. The black circles show the location of the samples.

The Miocene subsidence testified by Miocene limestone beds can not be reconstruct by thermochronology or modelling and retrodeformation of this specific section, because the sediments are very shallow and never exceed few meters of thickness.

# CHAPTER EIGHT

# CONCLUSIONS

Throughout the jointed use of low-temperature thermochronology and structural modelling, it was possible to achieve the following basic conclusions:

- The timing of the Holy Cross Fault and its displacement were defined: though this fault was active in several different moments through time, the most important movements occurred during the Devonian and, secondly, the Silurian as a normal fault, whereas was reactivated as a thrust fault during the Variscan orogeny.
- Laramide orogeny barely affected the area: the compression created a large anticlinorium, but it was not enough to reactivate the Variscan thrusts.
- After the Paleocene the tectonic evolution of the area was irrelevant: the movements and deformations through the central and late Cenozoic were restrained.

# REFERENCES

Andreucci B., 2013. Thermochronology of the Polish and Ukrainian Carpathians, PhD Thesis.

Belka Z. 1990: Thermal maturation and burial history from conodont colour alteration data, Holy Cross Mountains, Poland. Courier Forsch.-Inst. Senckenberg, 118, pp. 241-251.

Berthelsen, A., 1993. Where different geological philosophies meet: the Trans-European Suture Zone. In: Gee, D.G., Beckholmen, M. (Eds.), EUROPROBE Symposium Jablonna 1991. Pubs. Inst. Geophys., Polish Acad. Sci., vol. 255, pp. 19–31.

Braun, J., Van der Beek, P., Batt, G., 2006, Quantitative Thermochronology: Numerical Methods for the Interpretation of Thermochronological Data. Cambridge University Press, Cambridge, New York.

British Geological Survay, Press Release, 29th March 2012.

Czarnocki, J., 1938. Carte geologique generale de la Pologne, feuille 4, Kielce, echelle 1 : 100,000. Serv. Géol. Pol.

Czarnocki, J., 1957. Tectonics of the Swiety Krzyz Mountains. Prace Panstw. Inst. Geol. 18 (2), (3), 138 pp.

Dadlez, R., 1989a. Epicontinental Permian and Mesozoic basins in Poland. Kwart. Geol., 33: 175-198 (in Polish with English summary).

Dadlez R., Kowalczewsk, Z., Znosko J., 1994. Some key problems of the pre-Permian tectonics of Poland. Geological Quarterly, 38, pp. 169-189.

Dadlez R., M. Narkiewicza, M.T.M. Visserb, J-D. van Weesb, 1995. Evolution of the Mid-Polish Trough: modelling implications and significance for central European geology. Tectonophysics Volume 252, Issues 1–4, 30 December 1995, pp. 179–195.

Dadlez R. (2001) — Holy Cross Mts. area — crustal structure, geophysical data and general geology. Geol. Quart., 45 (2): 99–106.

Farley, K.A., Wolf, R.W., Silver, L.T., 1996. The effects of long alpha-stopping distances on (U-Th)/He ages. Geochim Cosmochim Ac. 60, 4223-4229.

Farley, K.A., 2002. (U-Th)/He dating: techniques, calibrations, and applications. In Noble Gases in Geochemistry and Cosmochemistry. Rev. Min. Geochem. 47, pp. 819–44.

Fitzgerald P.G., 1992. The Transantarctic Mountains of southern Victoria Land: The application of apatite fission track analysis to a rift shoulder uplift. Tectonics, Vol.11, pp. 634-662.

Fleischer, R.L.;.Price, P.B; Walker, R.M.; 1975; Nuclear Tracks in Solids: Principles and Applications; Univ. of Calif. Press, Berkeley.

Guterch A. et al., 1984. Deep strucrure of the Earth's crust in the contact zone of the Paleozoic and Precambrian Platforms and the Carpathian Mts in Poland. Acta Geophys. Pol., 32, p. 25-41, no. 1.

Guterch, A., Grad, M., Materzok, R., Perchuc, E., 1986. Deep structure of the Earth's crust in the contact zone of the Paleozoic and Precambrian platforms in Poland (Tornquist –Teisseyre Zone). In: Galson, D.A., Mu¨ ller,

St. (Eds.), The European Geotraverse, Part 2. Tectonophysics, vol. 128, pp. 251– 279.

Guterch, A., Grad, M., Janik, T., Materzok, R., Luosto, U., Yliniemi, J., Lick, E., Schulze, A. and Wrste, K., 1994. Crustal structure of the transition zone between Precambrian and Variscan Europe from new seismic data along LT-7 profile (NW Poland and eastern Germany). C.R. Acad. Sci. Paris, 319 (II): pp. 1489-1496.

Karwasiecka, M., Bruszewska B., 1997. Surface heat flow density in Poland. Central Geological Archive, Warszawa, Polish Geological Institute, unpublished report (in Polish).

Ketcham, R.A., Donelick, R.A., and Carlson, W.D., 1999, Variability of apatite fission track annealing kinetics III: Extrapolation to geological time scales. American Mineralogist, v. 84, pp. 1235-1255.

Konon A., 2004. Successive episodes of normal faulting and fracturing resulting from progressive extension during the uplift of the Holy Cross Mountains, Poland. Journal of Structural Geology, 26, pp. 419–433.

Kosakowski P., Wróbel M. and Krzywiec P., 2013. Modelling hydrocarbon generation in the Palaeozoic and Mesozoic succession in SE Poland and West Ukraine. Journal of Petroleum Geology, Vol. 36(2), April 2013, pp. 139-162

Kutek, J., Głazek, J., 1972. The Holy Cross area, Central Poland, in the Alpine cycle. Acta Geologica Polonica 22, pp. 603–653.

Kutek, J., 2001. The Polish Permo – Mesozoic Rift Basin. In: Ziegler, P.A., Cavazza, W., Robertson, A.H.P., Crasquin-Soleau, S. (Eds.), Peri- Tethyan Rift/Wrench Basins and Passive Margins. Peri-Tethys Memoir 6, Mé moires du Musé um National d'Histoire Naturelle 186, pp. 213 – 236.

Lamarche J. et al., 1999. Variscan tectonics in the Holy Cross Mountains (Poland) and the role of structural inheritance during Alpine tectonics, Tectonophysics 313, pp. 171–186.

Lewandowski, M., 1992. Paleomagnetic evidences for dextral strike-slip displacement of the southern block of the Holy Cross Mts. along the East European platform border during Variscan orogeny and its continental scale geotectonic implications. Geol. Carp. 46, 151–152.

Lisker F., B. Ventura, and U. A. Glasmacher, 2013. Apatite thermochronology in modern geology, Geological Society, London, Special Publications, 324, pp. 1-23

Marynowski, L., 1998. Degree of thermal alteration of organic matter from the Devonian deposits of the Holy Cross Mountains. Doctoral Thesis(in Polish). Uniwersytet Śląski, pp. 169.

MarinowskiI L. 1999: Thermal maturity of organic matter in Devonian rocks of the Holy Cross Mts (Central Poland). Prz. Geol., 47 (12), pp. 1125-1129 [in Polish with English summary].

Mineralogical Society of America, Geochemical Society, Volume 58: Low-Temperature Thermochronology: Techniques, Interpretations, and Applications, Peter W. Reiners & Todd A. Ehlers, editors

Mizerski, W., 1988. Tectonic evolution of the Lysogory region, Holy Cross Mts (with English summary). Przegl. Geol. 1, 142–146.

Narkiewicz, M., 2007. Development and inversion of Devonian and Carboniferous basins in the eastern part of the Variscan foreland (Poland). Geological Quarterly, 51, pp. 231-256.

Narkiewicz et al., 2010.New constraints on the Middle Palaeozoic to Cenozoic burial and thermal history of the Holy Cross Mts. (Central Poland): results from numerical modelling, Geologica Acta, Vol.8, No 2, pp. 189-205.

Pozaryski, W., Brochwicz-Lewinski, W., Tomczyk, H., 1982. On heterochroneity of the Teisseyre–Tornquist Line. Przegl. Geol. 11, pp. 569–574.

Poprawa P. Et al., 1997. Caledonian accretion along TESZ. Terra Nostra, 11, pp. 110–117.

Poprawa P. et al., 2005: Variscan heat transfer along the western prolongation of the Holy Cross Fault Zone by migration of hot fluids related to igneous intrusions (northern Małopolska Block, southern Poland). Pol. Tow. Mineral. Prace Spec., 25, pp. 180-183.

Poprawa, P., 2006a. Development of the Caledoniancollision zone along the western margin of Baltica and its relation to the foreland basin. (In Polish with Englishabstract). In: Matyja, H. and Poprawa, P. (Eds.), Facies, tectonic and thermal evolution of the Pomeranian sector of Trans-European Sature

Zone and adjacent areas. Prace Państwowego Instytutu Geologicznego, pp. 186, 189–214.

Reiners P. W., Ehlers T. A., Zeitler P. K., 2005. Past, present, and future of thermochronology. Reviews in Mineralogy and Geochemistry, 58, pp. 1–18.

Reiners, P.W. and Brandon, M.T., 2006, Using Thermochronology to Understand Orogenic Erosion, Annual Reviews of Earth and Planetary Science, v. 34, pp. 419-466.

Roure, F., Roca, E., Sassi, W., 1993. The Neogene evolution of the outer Carpathian flysh units (Poland, Ukraine and Romania): kinematics of a foreland=fold-and-thrust belt system. Sediment. Geol. 86, pp. 177–201.

Stupnicka, E., 1992. The significance of the Variscan orogenyin the Swietokrzyskie Mountains (Mid Polish Uplands). Geol.Rundsch. 81 (2), pp. 561–570.

Tagami, T., O'Sullivan, P.B., 2005. Fundamentals of fi ssion-track thermochronology. Rev. Mineral. Geochem. 58, pp. 19-47.

Todd A. Ehlers , Kenneth A. Farley, 2003. Apatite (U-Th)/He thermochronology: methods and applications to problems in tectonic and surface processes. Earth and Planetary Science Letters, 206, pp. 1-14.

Torsvik TH, Smethurst MA, Meert JG, R Van der Voo, WS McKerrow, 1996. Continental break-up and collision in the Neoproterozoic and Palaeozoic-a tale of Baltica and Laurentia. Earth-Science Reviews 40 (3), pp. 229-258

Valverde-Vaquero et al., 2000. U^Pb single-grain dating of detrital zircon in the Cambrian of central Poland: implications for Gondwana versus Baltica provenance studies. Earth and Planetary Science Letters 184, pp. 225-240

Ziegler, P.A., 1990. Geological Atlas of Western and Central Europe 1990. Shell Int. Petrol. Co. and Geol. Sot. Publishing House, Bath, pp. 239.

# ACKNOWLEDGMENTS

Heartfelt thanks to my supervisor, prof. Massimiliano Zattin, for all the support and the advices, and for giving me this thesis work, that I found very captivating.

I also deeply thank my co-supervisors: dott. Benedetta Andreucci, who taught me the principles of thermochronology with the same care and patience with which she picks her apatites, and dott. Ada Castelluccio, who introduced me to Move2013 and shares with me the traumas of Move's sudden crashes.

I thank the qualified chemist Sandra Boesso, who supported me in the long processes of sample separation, and the whole University of Padova's staff.

Besides the professional experience, there are many people that enriched me from a personal point of view.
So, a big "thank you" to Anzo and all my geologist (and not) friends for these years together.
I mightily thank my flatmates: Lisa, because she's unique and she sees me and I see her, Silvia, who has shared with me 10 square metres and a bunk-bed from the beginning and Sara, who paradoxically makes me more tranquil.

I deeply thank my Mum and my Dad, who are the best parents in the whole wide world to me, even if they don't believe that.
I thank my grandmothers, my grandfathers and all my relatives for remembering me my origins.
Finally, I thank Laura, the proof that childhood friendship can last in time.